Probabilistic Assessment and Robustness Analysis of Power Electronic System for Grid Applications

Gholami-Khesht, Hosein

DOI (link to publication from Publisher):
10.54337/aau644668261

Publication date:
2023

Document Version
Publisher's PDF, also known as Version of record

Link to publication from Aalborg University

Citation for published version (APA):
Gholami-Khesht, H. (2023). *Probabilistic Assessment and Robustness Analysis of Power Electronic System for Grid Applications*. Aalborg Universitetsforlag. https://doi.org/10.54337/aau644668261

PROBABILISTIC ASSESSMENT AND ROBUSTNESS ANALYSIS OF POWER ELECTRONIC SYSTEM FOR GRID APPLICATIONS

BY
HOSEIN GHOLAMI-KHESHT

DISSERTATION SUBMITTED 2023

AALBORG UNIVERSITY
DENMARK

PROBABILISTIC ASSESSMENT AND ROBUSTNESS ANALYSIS OF POWER ELECTRONIC SYSTEM FOR GRID APPLICATIONS

by

Hosein Gholami-Khesht

AALBORG UNIVERSITY
DENMARK

Dissertation submitted 2023

.

Dissertation submitted: September 2023

PhD supervisor: Prof. Frede Blaabjerg,
Aalborg University

Assistant PhD supervisor: Associate Prof. Pooya Davari,
Aalborg University

Prof. Xiongfei Wang
Aalborg University

PhD committee: Associate Professor Amin Hajizadeh (chairman)
Aalborg University, Denmark

Professor Marcelo Godoy Simões
University of Vaasa, Finland

Dr. Jin Tan
National Renewable Energy Laboratory, USA

PhD Series: Faculty of Engineering and Science, Aalborg University

Department: AAU Energy

ISSN (online): 2446-1636
ISBN (online): 978-87-7573-797-0

Published by:
Aalborg University Press
Kroghstræde 3
DK – 9220 Aalborg Ø
Phone: +45 99407140
aauf@forlag.aau.dk
forlag.aau.dk

Printed in Denmark by Stibo Complete, 2023

ENGLISH SUMMARY

The global energy paradigm shift from fossil fuel-based to renewable energy-based generation has demonstrated the role of power electronics technology in the power conversion process. Therefore, modern power systems are increasingly integrated with power electronics, also known as power electronic-based power systems (PEPS).

Although PEPS brings many opportunities in terms of full controllability and flexibility, as well as improved performance and efficiency, they may give rise to stability concerns, due to interaction between different control loops, converters, and components (such as transformers, cables, power factor correction capacitors, etc.) and low inertia characteristics of grid-connected converters. Moreover, PEPS are subjected to various uncertainties and disturbances, and their characteristics change considerably throughout the day due to the intermittency of renewable energy generators and loads as well over time. Owning to the abovementioned issues, stability and performance robustness analysis of the PEPS and also robust control system design of such systems have become more important and challenging.

In this respect, this Ph.D. project is dedicated to investigating probabilistic assessment and robustness analysis of PEPS, aiming to address stability and performance concerns. The approach takes into account the probability of different operating conditions, thereby reducing the need for overly conservative designs. The proposed robustness analysis identifies potential issues arising from fluctuations in inverter power levels, variations in power grid impedance, and interactions within control loops. This innovative approach seamlessly combines probabilistic and robust stability analyses, thereby facilitating risk and reliability assessment, an essential aspect of power system planning and design.

To enhance system robustness, the project introduces adaptive and robust control methods for inner control loops. An adaptive mechanism continually updates current control gains to accommodate changes in filter impedance, offering notable benefits for systems with uncertain or highly variable impedances. The robust H_∞ design technique, encompassing polytopic uncertainties, effectively addresses variations in filter and grid impedance. Experimental studies substantiate the efficacy of this technique, particularly under weak grid conditions, a dimension previously unexplored.

Moreover, to account for interactions between inner and outer control loops, the project proposes a systematic and optimal solution for managing broad-frequency dynamics, multi-input and multi-output (MIMO) structure, and cascaded control loops within grid-connected voltage source converters (VSCs). By introducing a linear optimization problem and utilizing an optimal control theorem, this solution systematically calculates the control gain matrix. This establishes transparent correlations between tuning parameters, stability, and performance indicators,

simplifying the design process. Furthermore, the proposed control structure enables the implementation of a high-bandwidth phase-locked loop (PLL) even when dealing with weak grid conditions.

DANSK RESUME

Det globale paradigmeskifte inden for energi fra fossilt brændstof til vedvarende energi har vist effektelektronikkens rolle i energiomformningsprocessen. Moderne el-systemer integrerer i stigende grad effektelektronik, også kendt som effektelektronikbaserede el-systemer (PEPS).

Selvom PEPS bringer mange muligheder for fuld styring og fleksibilitet samt forbedret ydeevne og effektivitet, kan de skabe stabilitetsproblemer på grund af komplekse interaktioner mellem forskellige kontrolsløjfer, omformere og komponenter samt lav inerti ved brug at net-tilsluttede omformere. Derudover er PEPS udsat for forskellige usikkerheder og forstyrrelser, og deres karakteristika ændrer sig markant eksempelvis i løbet af dagen på grund af svingende produktion og forbrug af vedvarende energi. Som følge af disse udfordringer er robusthedsanalyse af stabilitet og ydeevne for PEPS, samt robust kontrolsystemdesign af sådanne systemer blevet mere vigtige og udfordrende.

I denne sammenhæng er dette Ph.D. projekt dedikeret til at undersøge probabilistisk vurdering og robusthedsanalyse af PEPS med henblik på at håndtere stabilitets- og ydelses udfordringer. Tilgangen tager hensyn til sandsynligheden for forskellige driftsbetingelser, hvilket reducerer behovet for konservative designs. Den foreslåede robusthedsanalyse identificerer potentielle problemer, der opstår på grund af udsving i invertereffektniveauer, variationer i el-netimpedans og interaktioner inden for net-tilsluttede omformere. Denne innovative tilgang kombinerer probabilistiske og robuste stabilitetsanalyser og reducerer dermed risiko- og pålidelighedsvurderingen, en essentiel del af el-systemplanlægning og -design.

For at styrke de robusthed introducerer projektet adaptive og robuste kontrolmetoder til indre kontrolkredsløb. En adaptiv mekanisme opdaterer løbende nuværende kontrolgevinster for at imødekomme ændringer i impedansen og giver klare fordele for systemer med usikre eller stærkt variable impedanser. En robust $H\infty$-designmetode, der omfatter usikkerheder, håndterer effektivt variationer i filter- og netimpedans. Eksperimentelle undersøgelser bekræfter effektiviteten af denne metode, især under svage el-netforhold, en dimension der tidligere ikke er udforsket.

Desuden for at tage højde for interaktioner mellem indre og ydre kontrolkredsløb, foreslår projektet en systematisk og optimal løsning til at håndtere bredfrekvente dynamikker, multi-input og multi-output (MIMO)-strukturer og kaskadekontrolkredsløb inden for nettilsluttede omformere. Ved at introducere et lineært optimeringsproblem og udnytte en optimal kontrolmetode beregner denne løsning systematisk en kontrolmatrice. Dette etablerer en transparent sammenhæng mellem justeringsparametre, stabilitet og ydeevneindikatorer, samt forenkler designprocessen. Derudover muliggør den foreslåede kontrolstruktur implementeringen af en phase-locked loop (PLL) med høj båndbredde, selv når der arbejdes med svage netforhold.

TABLE OF CONTENTS

TABLE OF FIGURES

THESIS DETAILS

Thesis Title: Probabilistic Assessment and Robustness Analysis of Power Electronic System for Grid Applications

Ph.D. Student: Hosein Gholami-Khesht

Supervisors: Professor Frede Blaabjerg, Aalborg University

Professor Pooya Davari, Aalborg University

Professor Xiongfei Wang, Aalborg University

The main part of the dissertation is based on the following publications:

Publications in Refereed Journals:

[J1] **H. Gholami-Khesht**, P. Davari, M. Novak, and F. Blaabjerg, "A probabilistic framework for the robust stability and performance analysis of grid-tied voltage source converters," *Appl. Sci.*, vol. 12, no. 15, p. 7375, 2022, doi: 10.3390/app12157375.

[J2] **H. Gholami-Khesht**, P. Davari, C. Wu, and F. Blaabjerg, "A systematic control design method with active damping control in voltage source converters," *Appl. Sci.*, vol. 12, no. 17, p. 8893, Sep. 2022, doi: 10.3390/app12178893.

[J3] **H. Gholami-Khesht**, P. Davari, and F. Blaabjerg, "An Adaptive Model Predictive Voltage Control for LC-Filtered Voltage Source Inverters," *Appl. Sci.*, vol. 11, no. 2, p. 704, Jan. 2021, doi: 10.3390/app11020704.

Publications in Refereed Conferences:

[C1] **H. Gholami-Khesht**, M. Monfared, M. Graungaard Taul, P. Davari, and F. Blaabjerg, "Direct adaptive current control of grid-connected voltage source converters based on the Lyapunov theorem," *2020 IEEE 9th Int. Power Electron. Motion Control Conf. IPEMC 2020 ECCE Asia*, pp. 858–863, 2020, doi: 10.1109/IPEMC-ECCEAsia48364.2020.9368224.

[C2] **H. Gholami-Khesht**, P. Davari, M. Novak, and F. Blaabjerg, "Robust H_∞ current control of three-phase grid-connected voltage source converters using linear matrix inequalities," in *2021 IEEE 22nd Workshop on Control and Modelling of Power Electronics (COMPEL)*, Nov. 2021, pp. 1–6. doi: 10.1109/COMPEL52922.2021.9646071.

[C3] **H. Gholami-Khesht**, P. Davari, and F. Blaabjerg, "Adaptive predictive-DPC for LCL-filtered grid-connected VSC with reduced number of sensors," *2020 22nd Eur. Conf. Power Electron. Appl. EPE 2020 ECCE Eur.*, pp. 1–10, 2020, doi: 10.23919/EPE20ECCEEurope43536.2020.9215839.

Publications in Book Chapters:

[B1] **H. Gholami-Khesht**, P. Davari, and F. Blaabjerg, “Adaptive control in power electronics systems,” in *Control of Power Electronic Converters and Systems*, Academic Press, Vol. 3, Chapter 5, 2021.

[B2] **H. Gholami-Khesht**, P. Davari, and F. Blaabjerg, “Sliding mode control in power electronics systems,” in *Control of Power Electronic Converters and Systems*, Academic Press, Vol. 3, Cahpter 3, 2021.

This dissertation has been submitted for assessment in partial fulfillment of the Ph.D. degree. The thesis serves as a summary of the above publications with highlighting the outcome of the Ph.D. project. Parts of the results are used directly or indirectly in the extended summary of the thesis. The coauthor statements have been made available to the assessment committee and are also available at the Faculty of Engineering and Science, Aalborg University.

PREFACE

The following content summarizes the main outcomes of the Ph.D. project, titled "Probabilistic Assessment and Robustness Analysis of Power Electronic Systems for Grid Applications," conducted at AAU Energy, Aalborg University, Denmark. This project received funding from the Villum Foundation Denmark through the Reliable Power Electronic based Power Systems (REPEPS) project for 3 years. The author acknowledges the support of AAU Energy and the Villum Foundation.

Special thanks go to my supervisor, Professor Frede Blaabjerg, for his invaluable expertise, guidance, and support throughout this rewarding experience. To my co-supervisors, Assoc. Prof. Pooya Davari and Prof. Xiongfei Wang, I extend my appreciation for their contributions, unique perspectives, and constructive feedback that enriched my work significantly. I feel incredibly fortunate to have had the privilege of learning from such distinguished experts in their respective fields.

Gratitude is also extended to Dr. Kazem B. Dowlatabadi, Dr. Mikkel P. Sidoroff Gryning, and Dr. Lukasz Kocewiak for their precious input and collaborative efforts during my study abroad with Ørsted.

I want to emphasize my profound appreciation to all my colleagues at the Department of Energy Technology, Aalborg University, especially Saeed Peyghami, Mateja Novak, Chao Wu, Shih-Feng Chou, and Mads Graungaard Taul, whose valuable suggestions and fruitful discussions greatly contributed to my research endeavors.

Finally, I wish to express my profound and heartfelt gratitude to my wife. Her unwavering belief in my abilities and her constant support have been the driving force behind my achievements. Her encouragement and sacrifices allowed me to devote my full attention to my studies, and her presence in my life has made all the difference. I am forever grateful for her unwavering support.

I also want to extend heartfelt thanks to my parents for their love, guidance, and encouragement, and I am eternally grateful for everything they have done for me.

Chapter 1. Introduction

1.1. Background

Nowadays, renewable energy sources have become a critical part of the energy sector and form a sustainable development by producing minimal greenhouse gas emissions, diversifying energy supply sector, and reducing the dependency on imported fossil fuels. Among them, solar and wind power plants have become more and more important and popular; in such a way, 209.6 GW of solar PV and 97.3 GW of wind power new capacity were installed in 2022, compromising 90% of the renewable new installation as shown in Fig. 1.1 [1].

With this new installation, the global installed capacity of PV and wind power achieved a remarkable record of 1100.9 GW and 925.6 GW, respectively. It increased the share of these sources in global electricity production by exceeding 28% in 2021. Renewable energy is expected to contribute almost 40% of global electricity output in 2027 to compensate for coal's, natural gas's, and nuclear's declining market share as shown in Fig. 1.2 [1].

However, renewable energy sources produce electrical energy with different characteristics (voltage and frequency) from the power grid. Therefore, a power electronics converter is required as an interface to successfully inject produced power by renewables into the power grid and meet the grid code requirements, as it is shown in Fig. 1.3.

Even though the massive integration of power electronics-based renewable energy systems provides more economical and environmental advantages, it causes considerable concerns among power system researchers and engineers, specifically about the robustness and reliable operation of these revolutionized power systems. The main challenges come from low inertia characteristics and wide time-scale control dynamics of static power converters, making them more vulnerable to disturbances (even small ones) in the grid over a wide frequency range [2]–[4].

Previously, these problems have not been crucial due to the higher inertia and low-frequency characteristics of conventional, centralized, and bulk power generators. Indeed, the stored energy in large rotating generators helps the traditional power system to maintain stability and absorb minor load disturbances.

Therefore, to make a successful green transition, the stability issues regarding power converters' multiple time scale, fast dynamic response, low inertia characteristic, and interactions between different control loops, converters, and power grids must be adequately understood and addressed [2]–[4]. This understanding is crucial in achieving a highly reliable power system that can continuously supply end-consumers and also be reliable for suppliers, including private distributed generators (DGs).

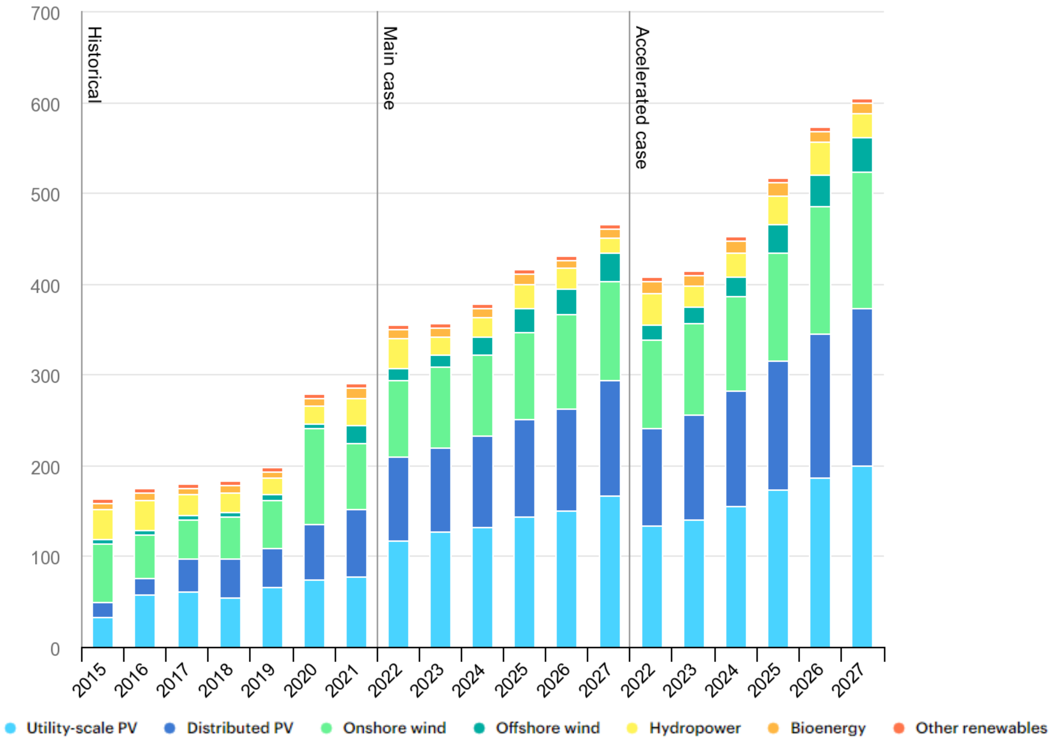

Fig. 1.1: Amounts of new renewable energy capacity added annually by technology historical, main case and accelerated case, 2015-2027. Source: [1]

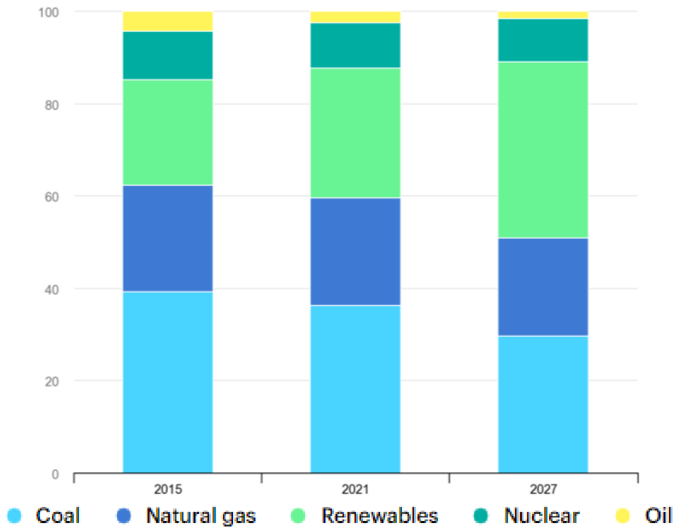

Fig. 1.2: Global electrical power generating capacity, 2015, 2021, and-2027. Source: [1].

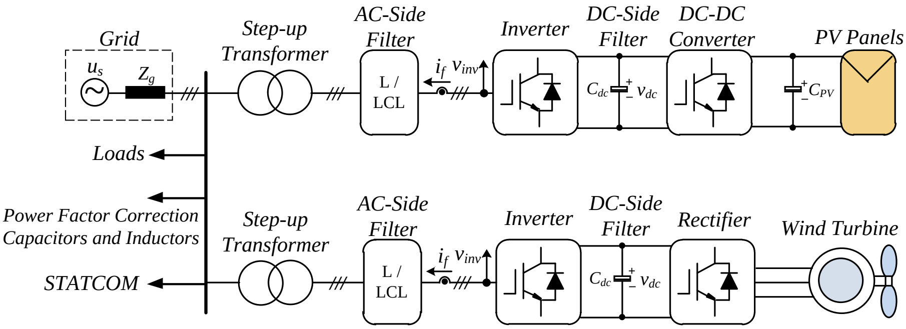

Fig. 1.3: State-of-the-art renewable generators and possible grid interfaces to the grid.

1.2. Research Gaps Identified by Ph.D. Project

The following summarizes the research gaps identified in the Ph.D. thesis concerning modeling, stability analysis, and robust control system design of modern power electronics-based power systems (PEPS).

These research gaps will be supported by the state-of-the-art of relevant research topics in the next subsections.

Research Gap 1 (Complexity Reduction of PEPS Description and Modeling)

Because of the multiple time-scale dynamics of power converters, the system order and complexity will significantly increase in a PEPS. In this situation, numerous uncertain parameters and disturbances such as variable grid conditions, operational-point changes, and other uncertainties in the power system lead to more complicated mathematical models and consequently more conservative designs (higher conservatism leads to smaller sets of parameters satisfying design criteria and less performance as a result). Therefore finding solutions to reduce the model complexity while considering potential uncertainties is highly required in order to do an analysis. Moreover, much efforts need to make results more realistic and less conservative, maybe by assessing the likelihood of the varying conditions.

Research Gap 2 (PEPS Robustness Analysis)

Most robust stability and performance assessment are developed for a specific problem and do not provide a general framework. In this respect, providing a comprehensive robustness framework for PEPS analysis that can include more practical issues and reveal the system dynamic behavior under different uncertainties and disturbances is highly desired. In addition, although numerous studies cover various aspects of the reliability-based analysis of PEPS, many questions have remained regarding the impact of control performance and robustness on the risk and reliability assessment. Therefore, more efforts to present efficient solutions are still required.

Research Gap 3 (Robust and Optimal Control System Design)

Although many efforts have been made to provide control design guidelines for grid-connected VSCs in the literature, however, the research on developing optimal, robust, and multi-input, multi-output (MIMO) control strategies that can consider all control loop interactions and provide sufficient robustness and desired responses under different operating conditions do not match the advancement of the control theory. Therefore, there is a need to take advantage of these advanced design techniques and present more efficient and practical solutions for VSCs.

1.3. State-of-the-art

1.3.1. State-of-the-art of Modeling and Robustness Analysis of PEPS

Although PEPS brings many opportunities in terms of full controllability and flexibility, as well as improved performance and efficiency, they may give rise to stability concerns due to their low inertia characteristics and broad time-scale dynamics in the grid-connected voltage source converters (VSCs) [2]–[4]. Fig 1.4 visualizes this wide frequency range of power converters and compares it to conventional synchronous generators. As it can be concluded from this figure, modern power systems are at risk of interaction between different control loops, converters, and components (such as transformers, cables, power factor correction capacitors, etc.) due to their broad frequency characteristics. Just a slight variation and disturbance may cause significant variations in power system currents and voltages, and e.g., introduce harmonic stability problems [2].

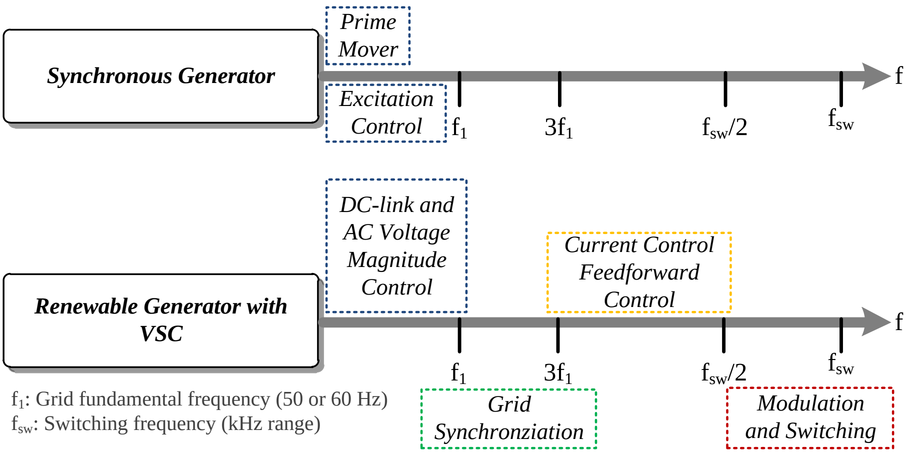

Fig. 1.4: Mapping between time scales of power system oscillations and control loops for conventional synchronous generator and state-of-art renewable generator with voltage source converter (VSC).

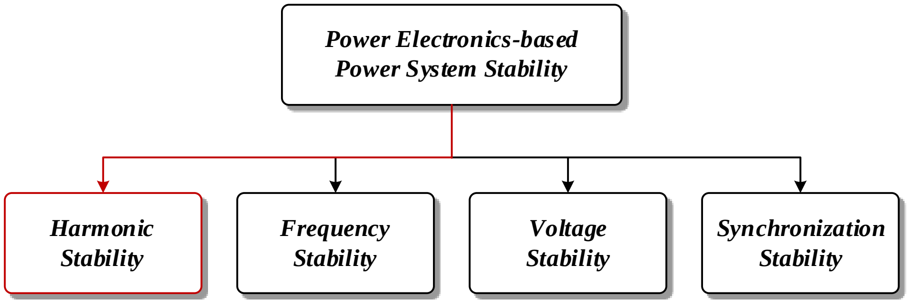

Fig. 1.5: Stability classification in a power electronics-based power system (PEPS). The harmonic stability, highlighted in red, is the main focus of this thesis [5].

It is worth noting that, as shown in Fig. 1.5, there exist other types of PEPS stability issues, such as synchronization stability, frequency stability, and voltage stability, which are other interesting and important topics but selected to be out of this project's scope [3], [5], [6]. This thesis is only focused on small-signal harmonic stability which typically appears due to the interaction on power converters.

Much research works have recently focused on harmonic small signal stability analysis of PEPS, either using impedance [7]–[20] or state-space [21]–[26] modeling. These methods are prevalent due to the simplicity of application and the effectiveness of clarifying different operational aspects of the modern power system. However, they have been established for stability and performance analysis around a certain steady-state operating point for systems subject to the constraints of linearity and time-invariance. They are therefore unable to study how multiple uncertain parameters and disturbances affect the stability and performance of the system. PEPS are subjected to various nonlinearities of power electronics systems, operational point changes, interactions among different control loops and power system components. Conclusively, if these potential system uncertainties have not been incorporated correctly, stability assessment and mitigation may lead to a conservative design and inaccurate results.

Accordingly, much research works have been carried out to propose robust stability analysis methods to overcome the shortcomings of the classical ones. The leading-edge and innovative solutions are e.g., structured singular value analysis (or μ-analysis) [27]–[31], Edge theorem [32], Lyapunov stability function and linear matrix inequalities (LMIs) based approaches [33]–[40], and probabilistic stability analysis [41]–[48].

The structured singular values or μ-analysis is a powerful mathematical method for assessing the stability robustness under different types of uncertainties: 1) uncertain real parameters (commonly structured or parametric uncertainty), 2) unstructured uncertainty (e.g., neglected or un-modeled high-frequency dynamics), and 3) mixed parametric-unstructured uncertainty. This method gives a worthy measure of stability robustness and can be applied to different PEPS under various uncertainties.

For instance, μ-analysis has been used for the robust stability analysis of a grid-connected synchronverter in [27], where unstructured uncertainties represent uncertainties in control and power grid parameters. In this study, the μ-analysis is compared to conventional eigenvalue analysis regarding applicability and effectiveness. Results have verified that μ-analysis can better reveal the impact of grid strength on the synchronverter stability. In such a way, it is demonstrated that the robustness of the synchronverter would be improved under weaker grid conditions, which disproves the expressed results from conventional eigenvalue analysis [49]. In [31], the interaction of two nearby power converters under uncertain grid conditions in terms of μ is analyzed. The grid short circuit ratio (SCR), X/R ratio, and high-frequency effects in the power grid are considered uncertain and represented by a multiplicative representation. Although the obtained results still verify the effectiveness of μ for a larger-scale power system, the conservatism is also increased, e.g., the estimated PLL bandwidth that may lead to system instability is lower than the actual one. Therefore, as a consequence of analysis, the designer may need to reduce the PLL bandwidth, which can lead to degraded performance, increased sensitivity to disturbances, and compromised overall functionality.

μ-analysis can address different robustness problems from the theoretical point of view, but there are still practical challenges. The procedure is computationally complex and needs high expertise to apply. Usually, specialized software tools (e.g., MATLAB Robust Stability Toolbox) are required to perform the linear fractional transformation (LFT) and μ-analysis. Moreover, calculating the exact value of μ is not accessible, and different solvers only try to estimate its upper and lower bounds. For that reason, there is usually some conservatism in applying μ, as partially shown in [31]. It gets worse where multiple uncertain real parameters exist. The lower bound of μ converges to zero in this situation, generating inaccurate results.

In [32], the Edge theorem is employed as a state-of-art robustness method to analyze the stability impact of wind power plant participation in the automatic generation control. In this research, the share of wind power systems is considered uncertain, thus limiting the use of classical stability analysis methods.

Robust stability analysis of DC microgrids using the Lyapunov stability theorem is studied in [33], [34]. In these research works, polytopic uncertainties based on LMIs represent variable constant power loads (CPLs). [36] and [37] address uncertainties in grid inductance for grid-connected applications of VSCs. Again, based on the Lyapunov stability function and LMIs, the system robustness is investigated and also improved. Finally, [38] considers the impact of uncertain control system delay in addition to uncertainties in grid impedance. Therefore, a new robust stability theorem is introduced based on the Lyapunov-Krasovskii function with LMIs.

Despite their advantages in representing different types of uncertainties and conducting robust stability analysis, the same as μ-analysis, they are mathematically complicated, and their application to a higher-order power system with multiple uncertain parameters and disturbances is complex and conservative. It is the main reason why they are limited used to a specific type of PEPS, whereas it is highly required to provide a general robustness framework that can represent and analyze more realistic problems with more components involved.

Moreover, from a power system design perspective, provided results may not be optimal and cost-effective since they investigate the worst-case scenario, which may have a low probability of occurrence. In this respect, to provide more reliable and cost-effective solutions and simultaneously account for all power system uncertainties and disturbances in the study, probabilistic stability analysis can be thought of as a simple but efficient method. The probabilistic robustness assessment defines proper probability distribution functions (PDFs) for the most influential parameters and considers the likelihood of different scenarios. One appropriate method of sampling, usually Monte Carlo (MC), pulls out the data from PDFs. The sampled data are then used in the stability model to calculate stability measures. Finally, the statistical properties of the stability indices are calculated, which provide a wealth of statistical information. Since they can consider the various uncertainties, operating point changes, the variational nature of renewables, and their probability of occurrence, the provided results are more accurate and realistic [41]–[48].

Yet, the probabilistic-based analysis methods have not been widely used in PEPS, with a few exceptions, such as reliability evaluation [50], [51], lifetime estimation [52], [53], and efficiency calculation [54]. In [45], [46], and [46]–[48], probabilistic large-signal and small-signal stability analyses have been reported to include load impacts, generation variations, and other power systems disturbances. However, the developed methods only consider the rotor angle stability and low-frequency electromechanical oscillations of conventional power systems, which may not be enough to emerging power electronics-based power systems with broad time-scale control dynamics and possible interaction between control loops, converters, and the power grid.

As discussed above, even though much efforts have been devoted to modeling and analyzing modern power electronics-based power systems, there are several research gaps.

1.3.2. State-of-the-art of Robust and MIMO Control System Design of PEPS

After doing proper modeling and stability analysis of PEPS and then identifying potential stability issues, the next step would be to consider remedial actions to ensure system robustness. Usually, the most reformative solutions come from the control system. In this respect, a robust and optimal control system design would be highly preferred to provide sufficient damping for oscillations instability, reduce control loops and power converters interactions, and ensure desired stability and performance margins. It is worth noting that such design strategies also need to be practical and efficient without an increased implementation complexity.

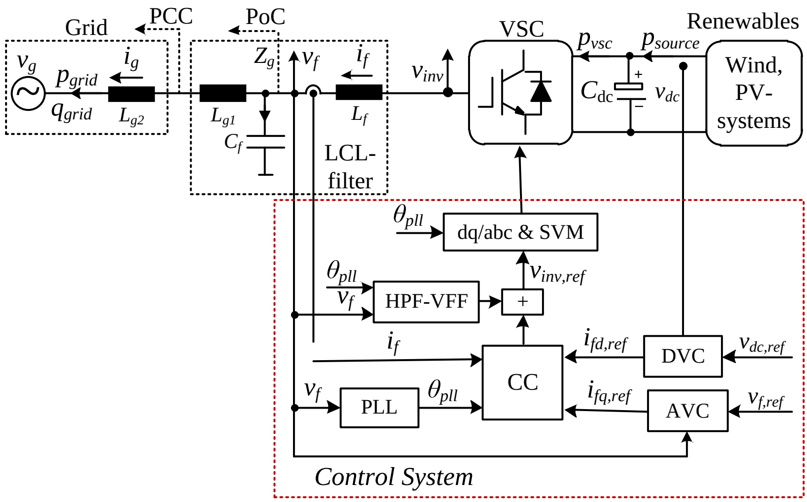

Fig. 1.6: The conventional control method of grid-connected voltage source converters (VSCs) in renewables power systems. CC: current controller, HPF-VFF: high pass filter-based voltage feedforward controller, AVC: AC voltage magnitude controller, DVC: dc-link voltage controller, PLL: phase-locked loop, SVM: space vector modulation, PoC: point of control, PCC: point of common coupling. **Source: [J2].**

Fig. 1.6 shows a conventional control structure of VSCs, which is the main used control structure in this research project.

It includes multiple and cascaded control loops such as dc-link voltage controller (DVC) or active power control loop, ac voltage magnitude controller (AVC) or reactive power control loop, inverter current control loop and protection (CC), high pass filter-based voltage feedforward controller (HPF-VFF) to damp LCL filter resonances, and a phase-locked loop (PLL) for grid synchronization in the case it is a grid-following converter. Despite their facilitation in utilizing VSCs and meeting diverse performance objectives, these controllers also lead to the emergence of a nonlinear control system with strongly coupled, asymmetric, and broad frequency-range dynamics.

So far, considerable efforts have been put into developing a proper control system and design strategy [49]–[65] for the VSC. References [55]–[62] developed a design strategy based on the well-known impedance model. They employed the generalized Nyquist or passivity theorems to reveal different stability phenomena and control gains calculations to achieve a certain performance and robustness.

However, optimal control gain calculations based on these theorems and the modeling are challenging tasks, especially for a high-order, broad frequency-range, and MIMO system like PEPS. Consequently, these design procedures usually lead to a time-consuming and iterative process. For instance, [56] proposed a design method to recursively adjust the current controller’s gains. This work considered the control delay effect on the system stability and ignored the resonances due to the LCL filter. A proper current control design framework for a grid-connected LCL-filtered VSC is presented in [57]. Additional active damping techniques based on the grid-side current control and virtual flux are applied to the current controller in [58] and [59] to suppress LCL filter resonances and control delay adverse effects. Also, many ideas have been given to overcome the adverse effects of digital controllers (routinely employed in the HPF-VFF and CC) on the passivity of the converter output admittance [60]. Finally, an improved control design is recommended to reduce the interaction between the current control loop and PLL in order to improve system robustness under weak grid conditions. Despite these advantages, the method requires extra sensors to measure capacitor current, increasing cost and volume.

In addition to the impedance model and frequency domain-based techniques, other approaches employ the state-space model [35]–[39], [63]–[70]. In [63]–[66], a state-space model-based predictive current control for LCL-filtered VSC has been suggested. In these works, the internal current control is only considered, and instability initiated by insufficient damping in the high-frequency range is studied. Although MPC-based methods provide a fast dynamic response and are suitable for digital implementation, they suffer from validated models and the accuracy of parameters [67]. Moreover, their other important shortcomings are variable switching frequency and more widespread current harmonics.

A full state-space feedback control based on the reduced-order observer is designed to dampen the LCL filter resonance and increase the system robustness at low SCR grids [68]. In contrast, a very low PLL bandwidth, i.e., 2 Hz, is selected to avoid interaction between the current control loop and PLL, which leads to a slow dynamic response and very poor disturbance rejection [68] from the grid. Moreover, pole placement technique is employed to calculate current control and active damping gains. In spite of the method clarity, selecting the desired closed-loop poles for a practical power system subjected to physical limitations and control input saturation is not a trivial task.

A systematic design approach based on the optimal control theorem is presented in [69] and [70], which compromises system performance and control efforts and avoids direct pole placement. However, it requires weighting factors selection, usually tunned based on trial and error, that greatly influences the system's response. Authors in [70] enhanced the control system by considering the impact of PLL. Yet, weighting factors calculation is needed, and tuning factors are not directly linked to stability or performance measures.

In [35]–[40], a robust H_∞ design technique using LMIs is suggested to reduce the impact of the grid SCR changes on the system operation. A systematic way to consider grid SCR uncertainties and calculate the proportional and resonant gains of the current controller is proposed. However, only a simplified model is considered in in their analysis. Moreover, the optimal robust H_∞ technique leads to a high norm of the control gain matrix, making it problematic for practical implementations [36],

[37], [71]. Additional LMIs and a genetic algorithm with a proper objective function have been suggested [36] and [37] to reduce excessive control gains but it comes at a cost of increased complexity and calculations.

Unlike previous works with a focus on internal and fast control loops, the authors in [62] proposed a design approach for external control loops (AVC and DVC) based on a loop-at-a-time stability assessment (LAAT). The proposed scheme has a close correlation to the characteristic loci in the generalized Nyquist criterion for MIMO systems and attempts to address issues concerning asymmetric and MIMO control dynamics. However, to simplify the problem's complexity, the possible interaction between internal and external control loops is overlooked, and the internal control loops (CC, HPF-VFF) and PLL are inserted inside the plant. A different but more comprehensive approach to obtain the external control gains is presented in [72], where the H_∞ optimization technique adjusts different input and output relationships based on defined dynamic weighting functions. However, many parameters should be tuned, which highly impact the system performance and complexity of solving the H_∞ optimization problem.

It is worth to note that all the previous works only considered one of the inner or outer control loops and kept the other ones out of the design process. If all are considered simultaneously, a nonlinear optimization problem will appear due to the multiplication of control gains. Therefore an improved design procedure that can overcome this problem is lacking and important to solve.

1.4. Thesis Motivation and Research Objectives

1.4.1. Research Motivations

1- As previously discussed, even though many valuable research works have tried to address the challenges of upcoming modern power systems with a massive integration of power converters, several research gaps and questions regarding their modeling, stability and performance sensitivity analysis, and control system design are remaining. The majority of issues arise due to the broad frequency range dynamics, rendering power systems more susceptible to unavoidable uncertainties and disturbances. Therefore, the prime motivation of this thesis is to provide a general robustness analysis framework that considers all uncertainties simultaneously and reflect their impact on the system behavior truly. Such a robustness assessment framework needs to be efficient and applicable to different power system applications and should try to avoid high complexity. Moreover, the provided results should be more realistic and less conservatism in design. In addition, new stability and performance indices may be required behind the existing ones to reveal better the impact of various uncertainties on the stability response.
2- After identifying the potential stability issues, it is necessary to take proper remedial actions. They usually originate from the control system and are

fulfilled by employing a suitable control structure and an appropriate control system design. The grid-connected power converter (see Fig. 1.6) operates with different outer voltage (power) control loops, inner current control loops, synchronism mechanisms, and also active damping control gains. They lead to relatively complex, coupled, asymmetric, and wide time-scale dynamics. Calculating the optimal control gains based on a full dynamic model of such a system is not easy due to a nonlinear optimization problem caused by multiplications of different control gains and states. Hence, it motivates this Ph.D. project to work on a new formulation that can solve this problem and provide a linear optimization problem while a complete dynamic model is still considered. In other words, this thesis would aim to find a systematic design strategy that can simultaneously consider inner and outer control loops and their interaction and reduce the recursive processes.

In conclusion, the primary motivation of this research project is to widen the existing knowledge on robustness analysis of power electronics-based power systems (PEPS) and provide a systematic control system design strategy with minimum iterative actions. It should be able to examine different operational aspects of modern power systems and provide solutions to improve their performance and avoid instability issues thereby having a strong system robustness.

Fig. 1.7 illustrates the Ph.D. thesis motivations and the associated research tasks required to achieve them. Work task 1 involves conducting a basic design of a grid-connected VSC. Subsequently, a MATLAB Simulink model and experimental setup will be developed to implement and assess the proposed solutions for modeling, robustness analysis, and robust control system design (work task 2).

The established basic design and test setup will serve as the basis for investigating conventional stability and control systems, thereby identifying potential research gaps (work tasks 3 and 4).

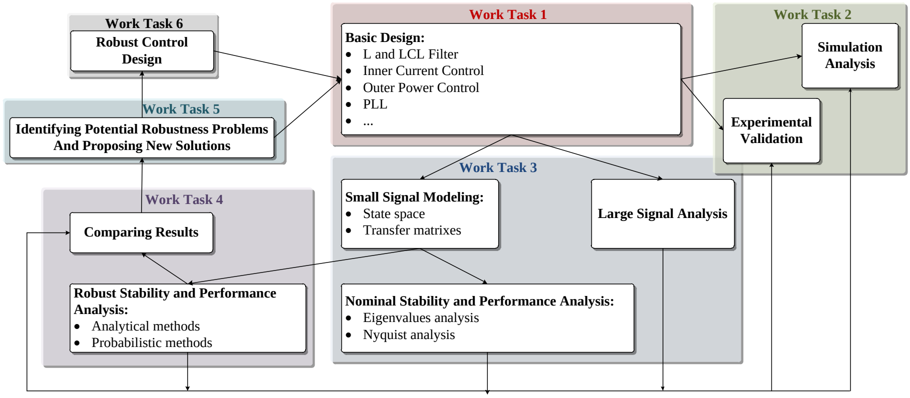

Fig. 1.7: Thesis motivations and considered research work tasks.

In work task 5, efforts will be made to expand the current understanding of robustness analysis and propose novel solutions. Ultimately, a new strategy for designing a robust control system will be discussed, aiming to address the identified stability and performance issues (work task 6). The outcomes of the new strategy will be compared with those achieved using conventional control methods.

1.4.2. Research Hypothesis Questions

The overall research hypothesis of this Ph.D. project is condensed into the following research question:

"*How to systematically analyze and identify robustness issues of power electronics-based power systems subjected to different uncertainties and disturbances, and what are the proper solutions to improve system robustness*?"

Based on the overall research question and the discussed research gaps, several sub-questions are identified to be:

- Can PEPS be modeled adequately using small-signal modeling techniques to include different aspects and system conditions?
- Which part of the system (or control parameter) exerts the most critical impact on the robustness of PEPS?
- How will a stability robustness analysis of PEPS be connected to the reliability metrics of such systems?
- Is it possible to benefit from the advantages of the probabilistic stability analysis for PEPS?
- What objectives should the control system be able to handle based on the robustness analysis results?
- Is it possible to propose a systematic design procedure with a minimum recursive process?
- Does a robust and optimal control system tackle system uncertainties and disturbances?
- Can a clear intuition be found between control tuning and relevant stability and performance indicators?

1.4.3. Research Objectives

Regarding these detailed research questions, the Ph.D. project can be represented by the following objectives:

Power electronics-based power systems description and modeling

Due to the wide time-scale dynamics of power converters, which include both electromechanical dynamics of electrical machines and electromagnetic transients of power networks into the system modeling, the system order and complexity is significantly increased compared to conventional synchronous generator based, and thus a high computational demand will be required. Moreover, variable grid conditions and other system uncertainties introduce a more complex case into the power system modeling. Therefore, one of the main aims of this project is to explore the adequate mathematical model of PEPS for an efficient analysis. Although this model should reflect the essential characteristics and oscillation modes of modern power systems, it should, on the other hand, have as low order as possible.

A probabilistic framework for robust stability and performance analysis of a single-converter system

The second objective of this research project is to widen the existing knowledge on the robustness analysis of PEPS and provide a general framework for probabilistic stability and performance analysis. It will give a new probabilistic perspective and suggests measuring stability and performance not only in absolute terms (determined by the deterministic assessment) but also in terms of their statistical properties (produced by the probabilistic assessment). This statistical information reveals the impact of uncertainties on the system response and provides a transparent physical intuition into the system stability problem. It can calculate the probability of a specific or desired condition and connect the stability robustness analysis to the risk and reliability evaluation.

A systematic control design method with active damping control in voltage source converters

In addition to the above objectives related to modeling and stability robustness analysis of power converters, a further step will be to take a proper control system and design strategy to eliminate instability issues and improve the system performance. As discussed previously, many efforts have partially addressed the challenges related to complex dynamics in a wide frequency range, multiple control loops with a MIMO structure, and uncertainties regarding grid variations. This project will keep the widely used cascaded control loops and improve them by adding active damping based on the state feedback. However, as it can be expected, including inner current and outer voltage controllers and active damping gains increases the number of tuning parameters and design complexity. In addition, when all control gains are simultaneously considered to be calculated, a nonlinear optimization problem will appear due to the multiplication of the control gains. This issue may limit the application of well-known and developed linear optimization techniques and leads to a more conservative and recursive procedure as well as time demands. Therefore new solutions are needed to calculate the control gains while recursive procedures are kept low. In addition to these, the provided design strategy will give a clear insight between stability and performance indices and tuning parameters, leading to a more efficient and straightforward design.

1.4.4. Limitations

This project considers some assumptions, simplifications, and limitations as follows:

- This project investigates the harmonic small-signal stability of grid-connected VSCs, while large-signal stability and grid faults are not of the primary concerns.
- The project focuses on the grid-side converter in back-to-back structures, e.g., in wind farm power systems and PV power plants, to investigate the interaction between power converters and the power grid.
- Only two-level voltage source converters are examined. Other topologies, such as multi-level converters and current source converters, are out of this project’s scope.
- A Thevenin model represents an external power grid as a combination of a (static) line inductor and an ideal voltage source.
- Nonlinear effects from inductors, step-up transformers, and protection devices are neglected.

1.5. Thesis Outline

The Ph.D. thesis will take the form of a collection of ***selected papers*** with an extended summary as a ***report***. How the ***selected papers*** constitute ***report chapters*** is shown in Fig. 1.8. The ***report*** contains five chapters, as described in the following:

Chapter 1 presents a literature review on the background of the problem and identifies the existing research gaps. Based on the research gaps, the hypothesis and motivation of this research project are explained and divided into several sub-questions, which further define the project objectives. In the end, the thesis outline and a list of selected publications are given.

Chapter 2 investigates the power electronics-based power systems structure and modeling. It discusses the conventional state-space modeling method and control system design as a base for future studies (and case studies) to compare with the proposed solutions.

Chapter 3 proposes a probabilistic framework for robust stability and performance analysis of a single-converter system. In this chapter, firstly, the stability and performance definitions and metrics as well as power system uncertainties are defined. After that, based on the provided robustness framework and information, the stability and performance of the studied power system under operational point changes and grid impedance variations are examined. The obtained results are discussed in detail, and the main reason behind them are carefully addressed.

Chapter 4 presents proposed solutions for adaptive and robust control methods for the inner loop in PEPS. At first, a proposed solution to implement an adaptive internal current controller is presented. Then the proposed solution for polytopic type representation of system uncertainties and robust H_∞-based current control design are discussed.

Chapter 5 suggests a comprehensive solution for robust design based on active damping control and an optimal theorem to consider the impact of PLL and outer voltage control loops. This chapter clarifies the direct relationships between control parameters and stability indices as well as provides design guidelines based on straightforward steps having minor iterative actions.

Finally, *Chapter 6* outlines this Ph.D. project's main findings and conclusions as well as highlights future research works.

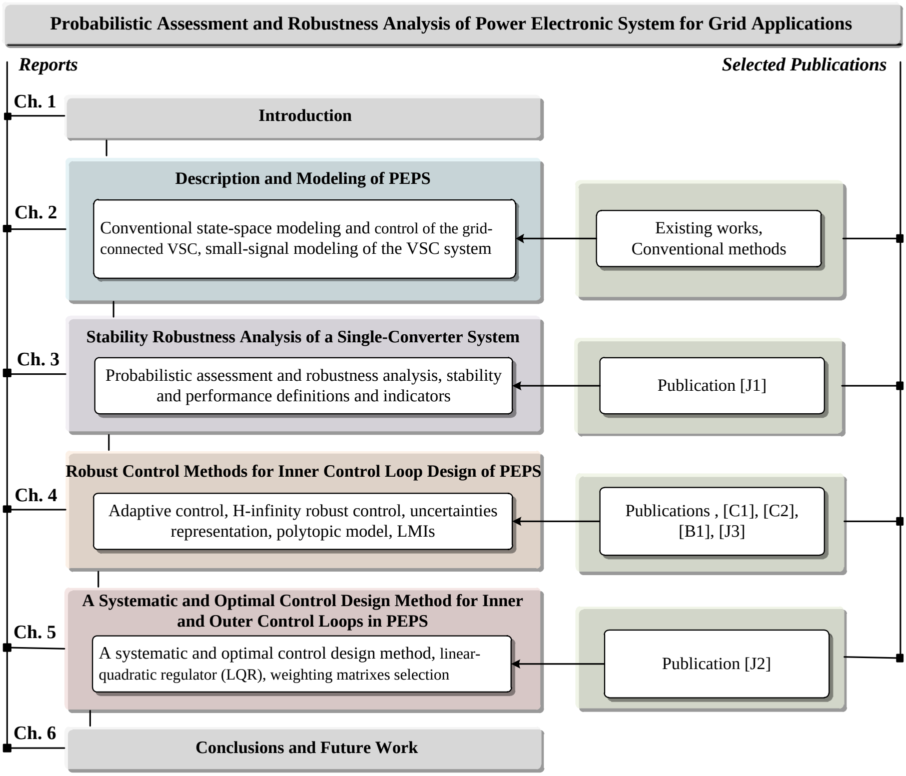

Fig. 1.8: Report structure and presentation of how the selected publications are linked to the chapters.

1.6. List of Publications

The results and outcomes of this Ph.D. project have been disseminated in the form of publications: journals, conferences, and book chapters. The following is a list of publications during the Ph.D. study:

Publications in Refereed Journals:

[J1] **H. Gholami-Khesht**, P. Davari, M. Novak, and F. Blaabjerg, "A probabilistic framework for the robust stability and performance analysis of grid-tied voltage source converters," *Appl. Sci.*, vol. 12, no. 15, p. 7375, 2022, doi: 10.3390/app12157375.

[J2] **H. Gholami-Khesht**, P. Davari, C. Wu, and F. Blaabjerg, "A systematic control design method with active damping control in voltage source converters," *Appl. Sci.*, vol. 12, no. 17, p. 8893, Sep. 2022, doi: 10.3390/app12178893.

[J3] **H. Gholami-Khesht**, P. Davari, and F. Blaabjerg, "An Adaptive Model Predictive Voltage Control for LC-Filtered Voltage Source Inverters," *Appl. Sci.*, vol. 11, no. 2, p. 704, Jan. 2021, doi: 10.3390/app11020704.

Publications in Refereed Conferences:

[C1] **H. Gholami-Khesht**, M. Monfared, M. Graungaard Taul, P. Davari, and F. Blaabjerg, "Direct adaptive current control of grid-connected voltage source converters based on the Lyapunov theorem," *2020 IEEE 9th Int. Power Electron. Motion Control Conf. IPEMC 2020 ECCE Asia*, pp. 858–863, 2020, doi: 10.1109/IPEMC-ECCEAsia48364.2020.9368224.

[C2] **H. Gholami-Khesht**, P. Davari, M. Novak, and F. Blaabjerg, "Robust H_∞ current control of three-phase grid-connected voltage source converters using linear matrix inequalities," in *2021 IEEE 22nd Workshop on Control and Modelling of Power Electronics (COMPEL)*, Nov. 2021, pp. 1–6. doi: 10.1109/COMPEL52922.2021.9646071.

[C3] **H. Gholami-Khesht**, P. Davari, and F. Blaabjerg, "Adaptive predictive-DPC for LCL-filtered grid connected VSC with reduced number of sensors," *2020 22nd Eur. Conf. Power Electron. Appl. EPE 2020 ECCE Eur.*, pp. 1–10, 2020, doi: 10.23919/EPE20ECCEEurope43536.2020.9215839.

Book Chapters:

[B1] **H. Gholami-Khesht**, P. Davari, and F. Blaabjerg, "Adaptive control in power electronics systems," in *Control of Power Electronic Converters and Systems*, Academic Press, Vol. 3, Chapter 5, 2021.

[B2] **H. Gholami-Khesht**, P. Davari, and F. Blaabjerg, "Sliding mode control in power electronics systems," in *Control of Power Electronic Converters and Systems*, Academic Press, Vol. 3, Chapter 3, 2021.

Chapter 2. Description and Modeling of PEPS

2.1. Background

As discussed in the introduction, this thesis aims to broaden existing knowledge on modeling, robustness analysis, as well as optimal and robust control system design that can be used in emerging power electronics-based power systems.

In this regard, the proposed solutions are applied to the most commonly used three-phase grid-connected voltage source converters (VSCs), which can be found in a wide range of power system applications such as renewable power generation, energy storage, flexible AC transmission systems (FACTS), and power quality equipment.

The considered VSC contains all control loops, such as DVC, AVC, CC, HPF-VFF, and a PLL like shown in Fig. 2.1. This structure provides the possibility of investigating many modern power system challenges like broad time scale dynamics as well as low- and high-frequency oscillations due to the interaction between VSC and the power grid as well as between the VSCs.

The following subsections briefly introduce the case study system; it will discuss how different control loops are designed conventionally and how a linearized state-space model can be obtained.

It is worth noting that the information presented in this chapter can also be found in other sources, but this chapter collects and summarizes them, and presents them in a readable manner for convenience. In addition, they are also used as a base case for the proposed solutions (on probabilistic robustness analysis, robust control system design, etc.) in the following chapters.

2.2. Nonlinear AC and DC side Power System Equations of the Grid-Connected Three-Phase VSC

The following equations describe the power system dynamics of the AC and DC sides of the grid-connected voltage source converter, encompassing current and voltage equations as well as power flows.

1) AC-side system equation

The control and circuit diagram of the studied grid-connected three-phase voltage source converter (VSC) is shown in Fig. 2.1. Based on this figure and Kirchhoff's Laws, the ac-side system equation in the vector frame can be written as:

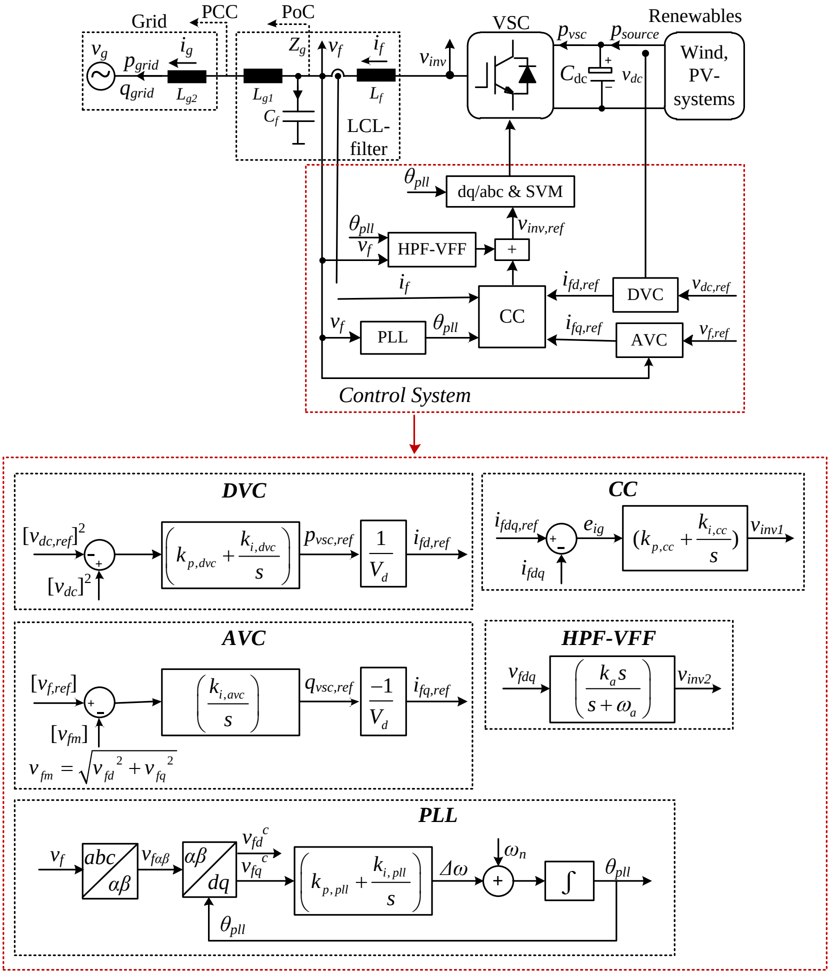

Fig. 2.1: The conventional control method of grid-connected voltage source converters (VSCs) in renewables power systems. CC: current controller, HPF-VFF: high pass filter-based voltage feedforward controller, AVC: AC voltage magnitude controller, DVC: dc-link voltage controller, PLL: phase-locked loop, SVM: space vector modulation, PoC: point of control, PCC: point of common coupling. **Source: [J2].**

$$
\begin{aligned}
\dot{i}_f &= L_f^{-1}\left(-r_f i_f - j\omega L_f i_f + v_{inv} - v_f\right) \\
\dot{v}_f &= C_f^{-1}\left(-j\omega v_f + i_f - i_g\right) \\
\dot{i}_g &= L_g^{-1}\left(-r_g i_g - j\omega L_g i_g + v_f - v_g\right),\ \ L_g = L_{g1} + L_{g2}
\end{aligned}
\tag{2.1}
$$

where, "." means d/dt. i_f, v_c and i_g are converter current, capacitor voltage, and grid current, respectively. Also, L_f, L_{g1}, r_f, r_g, and C_f are converter filter inductances and their equivalent series resistances and filter capacitance. In addition, L_{g2} is grid inductance. The filter capacitance's internal resistance is ignored here due to its lower impact.

2) DC-side system equation

The dc-side dynamics can be expressed with the power balance in the dc-link capacitor:

$$\frac{1}{2}C_{dc}\frac{d\left(v_{dc}{}^{2}\right)}{dt}=p_{source}-p_{vsc} \tag{2.2}$$

where, C_{dc} and v_{dc} are the dc-link capacitance and voltage, respectively. p_{vsc} and p_{source} are injected active power to the AC system and generated active power by DC sources. It is worth remarking that the converter is considered without losses. Active powers at the AC and DC side of VSC can be written as [13]:

$$\begin{cases} p_{vsc}=v_{fd}i_{fd}+v_{fq}i_{fq}+\dot{E}_L \\ E_L=0.5.L_f.\left(i_{fd}{}^2+i_{fq}{}^2\right) \\ p_{source}=v_{dc}i_{dc} \end{cases} \tag{2.3}$$

Here, v_{fdq} and i_{fdq} are capacitor voltage and converter current components in the grid dq-frame. Also, E_L is the stored energy in the inverter-side inductor, and i_{dc} is dc-side current source.

2.3. Control of the Grid-Connected Three-Phase VSC

This section discusses how different inner and outer control loops are designed conventionally.

1) *Inverter current control (CC)*

The current control loop employs the proportional-integral (PI) controller to ensure zero steady-state trackings as given in (2.4):

$$\begin{cases} v_{inv1}=G_{cc}(i_{fdq,ref}-i_{fdq}) \\ G_{cc}=k_{pc}+\dfrac{k_{ic}}{s} \end{cases} \tag{2.4}$$

The following equations can calculate the current control gains using (2.1) and (2.4) and considering the gain crossover frequency of the current control loop at ω_g [73]–[75]:

$$\begin{cases} k_{pc}=\omega_g.L_f \\ k_{ic}\simeq 0.1.\omega_g{}^2.L_f \end{cases} \tag{2.5}$$

ω_g should in general be ten times the fundamental frequency to ensure a fast-tracking response and less than one-tenth of the switching frequency for noise and harmonic attenuations.

2) Highpass filter-based voltage feedforward control (HPF-VFF)

To dampen the resonances introduced by the LCL filter, either passive or active damping is necessary. Passive damping is a simple solution to dampen the resonance. However, it increases the system losses and reduces its efficiency. In contrast, active damping can provide the required damping while the system losses are not increased. Therefore, active damping based on the high pass filter (HPF) feedforward of PoC voltage is commonly employed as discussed [23], [75]:

$$G_{HPF}(s) = \frac{v_{inv2}}{v_f} = \frac{k_a s}{s + \omega_a} \tag{2.6}$$

It is worth remarking that the HPF behaves like a parallel resistor to the PoC capacitor and improves the system stability. The corner frequency can be calculated as [76]:

$$\omega_a = \left(R_d C_f\right)^{-1}, R_d = \left(3\omega_{res} C_f\right)^{-1} \tag{2.7}$$

Here , $\omega_{res} = \sqrt{\dfrac{L_f + L_g}{L_f L_g C_f}}$ is the LCL filter resonance frequency. Since L_g includes variable grid inductance, the worst-case scenario should be considered to ensure a minimum stability margin under all conditions.

3) DC-link voltage control (DVC)

This control loop regulates the dc-link voltage at the desired value and generates the active power reference for the VSC or the *d*-axis reference current. It usually employs a PI controller to regulate the dc-link voltage. The controller output is the reference active power reference [77], [78]:

$$p_{vsc,ref} = -G_{dvc}.\left[v_{dc,ref}{}^2 - v_{dc}{}^2\right] = \left(k_{pd} + \frac{k_{id}}{s}\right)\left[v_{dc,ref}{}^2 - v_{dc}{}^2\right] \tag{2.8}$$

where, G_{dvc} is the PI controller of dc-link voltage, also k_{pd} and k_{id} are its proportional and integral gains. By replacing (2.8) in (2.2) and doing some manipulations, the closed-loop transfer function and control gains can be obtained as:

$$\begin{aligned} &\frac{v_{dc}{}^2}{v_{dc,ref}{}^2} = \frac{G_{dvc}}{0.5C_{dc}s + PI_{dvc}} = \frac{k_{pd}s + k_{id}}{0.5C_{dc}s^2 + k_{pd}s + k_{id}} \approx \frac{\omega_{dvc}{}^2}{s^2 + 2\omega_{dvc}\zeta_{dvc}s + \omega_{dvc}{}^2} \\ &\rightarrow \begin{cases} k_{pd} = \omega_{dvc}\zeta_{dvc}C_{dc} \\ k_{id} = 0.5\omega_{dvc}{}^2 C_{dc} \end{cases} \end{aligned} \tag{2.9}$$

where, ξ_{dvc} and ω_{dvc} are the desired damping ratio and closed-loop bandwidth of a standard second-order system. The control parameters are calculated so that the closed-loop bandwidth should be less than one-tenth of the inner current control loop bandwidth to avoid control loop interactions. However, under weak grid conditions, the closed-loop bandwidth is more restricted to be below the fundamental frequency to have a good stability margin and to avoid system instability [62]. The controller output is then divided by the PoC voltage amplitude (V_d) to generate the d-axis current reference:

$$i_{fd,ref} = \frac{1}{V_d} p_{vsc,ref} \tag{2.10}$$

Here, V_{d} is the steady-state value of the PoC voltage.

4) AC voltage magnitude control (AVC)

This control loop regulates the voltage amplitude at the PoC at the desired level and generates the converter reactive power reference. AVC commonly employs an integral controller, and the reactive power reference can be calculated by:

$$\begin{cases} q_{vsc,ref} = \dfrac{k_{ia}}{s}\left(v_{f,ref} - v_{fm}\right) \\ v_{fm} = \sqrt{v_{fd}^{\,2} + v_{fq}^{\,2}} \end{cases} \tag{2.11}$$

The controller output is then divided by the PoC voltage amplitude to generate the q-axis current reference:

$$i_{fq,ref} = \frac{-1}{V_d} q_{vsc,ref} \tag{2.12}$$

This control loop is slower than the DVC, and the closed-loop bandwidth will typically be selected below 10 Hz. The right choice is the closed-loop bandwidth of around 3 Hz [62], [79]. It is worth noting that the grid inductance has a significant impact on the performance of AVC. Therefore, the control parameters should be selected carefully to achieve the desired performance under the different possible grid impedances. The following can be used to calculate the control gain of the AVC [62]:

$$k_{ia} = \frac{\omega_{avc}}{\omega_1 L_{g,\min}},\ 1 < \frac{\omega_{avc}}{2\pi} < 10 \tag{2.13}$$

where, ω_{avc} and ω_1 are desired AVC bandwidth and fundamental frequency. Also, $L_{g,min}$ is the minimum expected grid inductance, meaning the strongest grid situation.

It is also remarkable to mention that the IEEE standard 1052-2018 has suggested a rise time (t_r) less than 100 ms (or equivalently $\omega_{avc} \approx 2.2/\ t_r$ = 2.2/100 ms = 22 rad/s or 3.5 Hz) for the AC voltage controller for a STATCOM. This recommendation provides a good compromise between a small-signal stability margin and transient response [62], [79], confirming the previous suggestion.

5) Phase-locked loop (PLL)

As shown in Fig. 2.1 and [80], a synchronous reference frame (SRF) PLL is employed to synchronize VSC with the PoC voltage. In this figure, $v_{f\alpha\beta}$ is the PoC voltage in the stationary reference frame.

$$v_{f\alpha\beta} = v_{f\alpha} + jv_{f\beta} \tag{2.14}$$

The *dq* voltages can be written using the following complex equations:

$$\begin{cases} v_f = v_{f\alpha\beta} e^{-j\theta_g} = V_d \\ v_f{}^c = v_{f\alpha\beta} e^{-j\theta_{pll}} = v_{fd}{}^c + jv_{fq}{}^c \end{cases} \tag{2.15}$$

Here, θ_g and θ_{pll} represent phase angles of the PoC voltage in the grid and the converter *dq*-frames.

By considering Δv_f as a small perturbation in PoC voltage, one has:

$$v_f = v_{f\alpha\beta} e^{-j\theta_g} = V_d + \Delta v_f = V_d + \Delta v_{fd} + j\Delta v_{fq} \tag{2.16}$$

By comparing (2.15) and (2.16), the following gives the relationship between PoC voltage at grid (v_f) and PLL (v_f^c) *dq* frames:

$$\begin{cases} v_f{}^c = \left(V_d + \Delta v_f\right) e^{-j\delta} \\ \Delta\theta = \theta_{pll} - \theta_g \end{cases} \rightarrow \begin{cases} v_{fd}{}^c = v_{fd} \\ v_{fq}{}^c = v_{fq} - V_d \delta \end{cases} \tag{2.17}$$

By doing some simplifications and using Fig. 2.1, the closed-loop transfer function and control gains can be obtained as [80]:

$$\frac{\Delta\theta}{v_{fq}} == \frac{k_{pp}s + k_{ip}}{s^2 + k_{pp}V_d s + k_{ip}V_d} = \frac{\omega_{pll}{}^2}{s^2 + 2\omega_{pll}\zeta_{pll}s + \omega_{pll}{}^2} \rightarrow \begin{cases} k_{pp} = \dfrac{2\omega_{pll}\zeta_{pll}}{V_d} \\ k_{ip} = \dfrac{\omega_{pll}{}^2}{V_d} \end{cases} \tag{2.18}$$

where, ξ_{pll} and ω_{pll} are the desired damping ratio and bandwidth of the closed-loop system. It is worth mentioning that various types of PLLs exist; however, in this context, one of the most commonly used PLLs is described and employed [81].

2.4. Small-Signal Modeling of the Grid-Connected Three-Phase VSC

The stability analysis based on an eigenvalues method requires a small-signal model of the VSC system linearized around an equilibrium point. Therefore, this section discusses how it can be calculated based on the system and control dynamics in the previous sections.

1) dq-frame transformation

As previously mentioned, to include the PLL dynamics, there are two *dq*-frames in the system small-signal model, i.e., the converter`(PLL) and the grid *dq*-frames. The converter *dq*-frame follows the estimated phase with PLL, and the grid *dq*-frame aligns with the positive sequence of PoC voltage. The transformation between these two *dq*-frames can be done as:

$$\begin{cases} x^c = xe^{-j\Delta\theta} \\ x = x^c e^{j\Delta\theta} \end{cases} \tag{2.19}$$

where x shows the vector in grid *dq*-frame and variable with subscript c shows the vector in the converter *dq*-frame. Assuming the vectors contain small perturbation and applying first-order Taylor expansion, the relationship between vectors in grid and converter *dq*-frames are given as:

$$x^c = X^c + \Delta x^c = \left(X + \Delta x\right)e^{-j\Delta\theta} = \left(X_d + jX_q + \Delta x_d + j\Delta x_q\right)\left(1 - j\Delta\theta\right) \tag{2.20}$$

In the converter *dq*-frame, without considering the second-order small-signal terms, the small-signal variation of vectors can be calculated as:

$$\begin{cases} \Delta x_d{}^c = \Delta x_d + X_q \Delta\theta \\ \Delta x_q{}^c = \Delta x_q - X_d \Delta\theta \end{cases} \tag{2.21}$$

Therefore the capacitor voltage and inverter current in converter and grid *dq*-frames can be related together as:

$$\begin{cases} \Delta v_{fd}{}^c = \Delta v_{fd} \\ \Delta v_{fq}{}^c = \Delta v_{fq} - V_d \Delta\theta \end{cases}, \quad \begin{cases} \Delta i_{fd}{}^c = \Delta i_{fd} + I_{fq} \Delta\theta \\ \Delta i_{fq}{}^c = \Delta i_{fq} - I_{fd} \Delta\theta \end{cases} \tag{2.22}$$

Here, $\mathbf{I_f}=I_{fd}+jI_{fq}$, and $\mathbf{V_f}=V_d$ are the steady-state values in the grid *dq*-frame, and prefix Δ shows the small-signal perturbation around the steady-state values.

2) AC and DC side power system equations

The following represents AC-side system equations in the vector frame using (2.1) and (2.22):

$$\begin{aligned} \Delta\dot{i}_f{}^c &= L_f{}^{-1}\left(-r_f \Delta i_f{}^c - j\omega L_f \Delta i_f{}^c + \Delta v_{inv}{}^c - \Delta v_f + jV_d \Delta\theta\right) \\ \Delta\dot{v}_f &= C_f{}^{-1}\left(-j\omega \Delta v_f + \Delta i_f{}^c + jI_f \Delta\theta - \Delta i_g\right) \\ \Delta\dot{i}_g &= L_g{}^{-1}\left(-r_g \Delta i_g - j\omega L_g \Delta i_g + \Delta v_f - \Delta v_g\right), \end{aligned} \tag{2.23}$$

Moreover, the small-signal model of the dc-side dynamic can be expressed as given in the following. By considering a small perturbation in all signals (i.e., $(x = X + \Delta x)$) in (2.2), doing some manipulations, and neglecting the second-order small-signal variation terms, the small-signal dynamic of active power balance (APB) can be represented as:

$$\begin{aligned} & V_{dc} C_{dc} \frac{d\Delta v_{dc}}{dt} = \\ & -L_f I_{fd} \frac{d\Delta i_{fd}}{dt} - L_f I_{fq} \frac{d\Delta i_{fq}}{dt} - I_{fd} \Delta v_{fd} - I_{fq} \Delta v_{fq} - V_d \Delta i_{fd} + V_{dc} \Delta i_{dc} + I_{dc} \Delta v_{dc} \end{aligned} \tag{2.24}$$

Here, capital letters are steady-state values. The dc-side dynamics can be rearranged as:

$$\begin{cases} \dot{x}_{dc} = \dfrac{1}{C_{dc} V_{dc}} \left(I_{fd} v_{fd} + I_{fq} v_{fq} - V_d I_{fq} \Delta\theta \right) + \dfrac{I_{dc}}{C_{dc} V_{dc}} x_{dc} + \\ \qquad + \left(\dfrac{V_d}{C_{dc} V_{dc}} + \dfrac{L_f I_{dc} I_{fd}}{\left(C_{dc} V_{dc} \right)^2} \right) i_{fd}{}^{c} + \dfrac{L_f I_{dc} I_{fq}}{\left(C_{dc} V_{dc} \right)^2} i_{fq}{}^{c} - \dfrac{i_{dc}}{C_{dc}} \\ \Delta v_{dc} = -x_{dc} - \dfrac{L_f}{C_{dc} V_{dc}} \left(I_{fd} . \Delta i_{fd} + I_{fq} . \Delta i_{fq} \right) = \\ \qquad - x_{dc} - \dfrac{L_f}{C_{dc} V_{dc}} \left(I_{fd} . \left(\Delta i_{fd}{}^{c} - I_{fq} \Delta\theta \right) + I_{fq} . \left(\Delta i_{fq}{}^{c} + I_{fd} \Delta\theta \right) \right) \end{cases} \tag{2.25}$$

where, x_{dc} is the state considered for state-space realization of dc-side dynamics.

3) Current control (CC)

The current controller in (2.4) can be written in the time domain as:

$$\begin{cases} \dot{\gamma}_{idq} = \Delta i_{fdq,ref} - \Delta i_{fdq}{}^{c} \\ v_{inv1} = k_{ic} \gamma_{idq} + k_{pc} \left(\Delta i_{fdq,ref} - \Delta i_{fdq}{}^{c} \right) \end{cases} \tag{2.26}$$

Here, γ_{idq} are integral states for CC.

4) Highpass filter-based voltage feedforward control (HPF-VFF)

The highpass filter in (2.6) can be represented in the time domain as:

$$\begin{cases} \dot{x}_{ffdq} = -\omega_a x_{ffdq} + \Delta v_{fdq}{}^{c} \\ v_{inv2} = -k_a \omega_a x_{ffdq} + k_a \Delta v_{fdq}{}^{c} \end{cases} \rightarrow \begin{cases} \dot{x}_{ffdq} = -\omega_a x_{ffdq} + \Delta v_{fdq} - jV_d \Delta\theta \\ v_{inv2} = -k_a \omega_a x_{ffdq} + k_a \left(\Delta v_{fdq} - jV_d \Delta\theta \right) \end{cases} \tag{2.27}$$

Here, x_{ffdq} are states considered for state-space realization of HPF-VFF.

5) Control delay

The reference voltage for VSC is the sum of the CC and the HPF-VFF outputs $\left(\Delta v_{inv,ref} = v_{inv1} + v_{inv2}\right)$. Moreover, the transfer function between the VSC output voltage (Δv_{inv}) and the reference one ($\Delta v_{inv,ref}$) is considered as a pure time delay:

$$\begin{cases} \Delta v_{inv}(t) = \Delta v_{inv,ref}(t - T_d) \rightarrow G_d(s) = \dfrac{\Delta v_{inv}}{\Delta v_{inv,ref}}(s) = e^{(-T_d . s)} \\ T_d = 1.5 T_{samp} \end{cases} \tag{2.28}$$

Here, T_{samp} is the sampling period of the controller. State-space realization of a first-order or third-order Pade approximation of control delay is often used and described in [23], [82]. The following shows the representation of a third-order Pade approximation in the state-space form:

$$\begin{aligned} &\underbrace{\begin{bmatrix} \dot{x}_{dq1} \\ \dot{x}_{dq2} \\ \dot{x}_{dq3} \end{bmatrix}}_{\dot{x}_d} = \begin{bmatrix} 0 & 1 & 0 \\ 0 & 0 & 1 \\ -120/T_d^{\,3} & -60/T_d^{\,2} & -12/T_d \end{bmatrix} \underbrace{\begin{bmatrix} x_{dq1} \\ x_{dq2} \\ x_{dq3} \end{bmatrix}}_{x_d} + \begin{bmatrix} 0 \\ 0 \\ 1 \end{bmatrix} \Delta v_{inv,ref} \\ &\Delta v_{inv} = \begin{bmatrix} \dfrac{240}{T_d^{\,3}} & 0 & \dfrac{24}{T_d} \end{bmatrix} x_{dq} - \Delta v_{inv,ref} \end{aligned} \tag{2.29}$$

where, $\left(x_{dq1}, x_{dq2}, x_{dq3}\right)$ are states considered for state-space realization of the control delay.

6) DC-link voltage control (DVC)

By linearizing (2.8) and (2.10), the linear time-domain dynamic of DVC can be expressed as:

$$\Delta i_{fd,ref} = \frac{-PI_{dvc}}{V_d}\left(V_{dc,ref}\Delta v_{dc,ref} - V_{dc0}\Delta v_{dc}\right) \tag{2.30}$$

(2.30) can be rewritten as:

$$\begin{cases} \dot{\gamma}_{dc} = \dfrac{k_{id}}{V_d}\left(V_{dc0}\Delta v_{dc} - V_{dc,ref}\Delta v_{dc,ref}\right) \\ \Delta i_{fd,ref} = \gamma_{dc} + \dfrac{k_{pd}}{V_d}\left(V_{dc0}\Delta v_{dc} - V_{dc,ref}\Delta v_{dc,ref}\right) \end{cases} \tag{2.31}$$

Here, γ_{dc} is the integral state for DVC.

7) AC magnitude voltage control (AVC)

The *q*-axis current reference can be calculated by the following using (2.11) and (2.12):

$$\begin{cases} i_{fq,ref} = \dfrac{-1}{V_d} q_{vsc,ref} = \dfrac{-1}{V_d}\left(\dfrac{k_{ia}}{s}\right)\left(v_{f,ref} - v_{fm}\right) \\ v_{fm} = \sqrt{{v_{fd}}^2 + {v_{fq}}^2} \rightarrow \Delta v_{fm} = \Delta v_{fd} \end{cases} \tag{2.32}$$

(2.32) can be rewritten as:

$$\begin{cases} \dot{\gamma}_{ac} = k_{ia}\Delta v_{fd} - k_{ia}\Delta v_{m,ref} \\ \Delta i_{fq,ref} = \dfrac{-1}{V_d}\left(\gamma_{ac}\right) \end{cases} \tag{2.33}$$

where, γ_{ac} is the integral state for AVC.

8) Phase-Locked loop

The open-loop transfer function between the q-axis component voltage and the output synchronization angle can be derived from Fig. 2.1 as follows:

$$\frac{\Delta\theta}{\Delta {v_q}^c} = \left(k_{pp} + k_{ip}\frac{1}{s}\right).\frac{1}{s} \tag{2.34}$$

Hence the time-domain dynamics of SRF-PLL can be written as follows:

$$\begin{cases} \dot{\gamma}_q = \Delta {v_{fq}}^c = \Delta v_{fq} - V_1\Delta\theta \\ \Delta\dot{\theta} = k_{i,pll}\gamma_q + k_{p,pll}\Delta {v_{fq}}^c = k_{i,pll}\gamma_q + k_{p,pll}\left(\Delta v_{fq} - V_d\Delta\theta\right) \end{cases} \tag{2.35}$$

Here, γ_q is the integral state for PLL.

9) The overall system state-space equations

By considering the small-signal modeling of the power system (LCL-filtered VSC and Thevenin-represented grid model) and control parts and by doing some manipulations, the state-space model of the overall system can be calculated as:

$$\dot{x}_{sys} = A x_{sys} \tag{2.36}$$

where, the system state vector (x_{sys}) is defined as:

$$x_{sys} = \left[\overbrace{\gamma_{id}, \gamma_{iq}}^{CC}, \overbrace{x_{ffd}, x_{ffq}}^{VFF}, \overbrace{x_{d1}, x_{d2}, x_{d3}, x_{q1}, x_{q2}, x_{q3}}^{Delay\ \text{model}}, \overbrace{\Delta {i_{fd}}^c, \Delta {i_{fq}}^c}^{VSC\ currents}, \overbrace{\gamma_q, \Delta\theta}^{PLL}, \overset{DVC}{\gamma_{dc}}, \overset{AVC}{\gamma_{ac}}, \overset{APB}{x_{dc}}, \overbrace{\Delta v_{fd}, \Delta i_{gd}, \Delta v_{fq}, \Delta i_{gq}}^{Capcitor\ \text{voltages}\ \&\ grid\ currents} \right]^T \tag{2.37}$$

Further the system state-matrix (A), which is essential for small-signal eigenvalue analysis, can be written as (2.38). It is worth remarking that, as shown, the state matrix depends on the operating point conditions and many other uncertain parameters that confirm the necessity of using robust stability and performance

$$
A=\begin{bmatrix}
0 & 0 & 0 & 0 & 0 & 0 & 0 & 0 & 0 & 0 & -1-\frac{k_{pd}L_f I_{fd}}{C_{dc}V_d} & -\frac{k_{pd}L_f I_{fq}}{C_{dc}V_d} & 0 & 0 & 1 & 0 & -\frac{k_{pd}V_{dc}}{V_{fd}} & 0 & 0 & 0 & 0 \\
0 & 0 & 0 & 0 & 0 & 0 & 0 & 0 & 0 & 0 & 0 & -1 & 0 & 0 & 0 & 1 & 0 & 0 & 0 & 0 & 0 \\
0 & 0 & -\omega_a & 0 & 0 & 0 & 0 & 0 & 0 & 0 & 0 & 0 & 0 & 0 & 0 & 0 & 0 & 1 & 0 & 0 & 0 \\
0 & 0 & 0 & -\omega_a & 0 & 0 & 0 & 0 & 0 & 0 & 0 & 0 & 0 & -V_{fd} & 0 & 0 & 0 & 0 & 0 & 1 & 0 \\
0 & 0 & 0 & 0 & 0 & 1 & 0 & 0 & 0 & 0 & 0 & 0 & 0 & 0 & 0 & 0 & 0 & 0 & 0 & 0 & 0 \\
0 & 0 & 0 & 0 & 0 & 0 & 1 & 0 & 0 & 0 & 0 & 0 & 0 & 0 & 0 & 0 & 0 & 0 & 0 & 0 & 0 \\
k_{ic} & 0 & -k_a\omega_a & 0 & \left(\frac{-120}{T_d^{\,3}}\right) & \left(\frac{-60}{T_d^{\,2}}\right) & \left(\frac{-12}{T_d}\right) & 0 & 0 & 0 & -k_{pc}\left(1+\frac{k_{pd}L_f I_{fd}}{C_{dc}V_d}\right) & -\frac{k_{pc}k_{pd}L_f I_{fq}}{C_{dc}V_d} & 0 & 0 & k_{pc} & 0 & -\frac{k_{pc}k_{pd}V_{dc}}{V_d} & k_a & 0 & 0 & 0 \\
0 & 0 & 0 & 0 & 0 & 0 & 0 & 0 & 1 & 0 & 0 & 0 & 0 & 0 & 0 & 0 & 0 & 0 & 0 & 0 & 0 \\
0 & 0 & 0 & 0 & 0 & 0 & 0 & 0 & 0 & 1 & 0 & 0 & 0 & 0 & 0 & 0 & 0 & 0 & 0 & 0 & 0 \\
0 & k_{ic} & 0 & -k_a\omega_a & 0 & 0 & 0 & \left(\frac{-120}{T_d^{\,3}}\right) & \left(\frac{-60}{T_d^{\,2}}\right) & \left(\frac{-12}{T_d}\right) & 0 & -k_{pc} & 0 & -k_aV_d & 0 & k_{pc} & 0 & 0 & 0 & k_a & 0 \\
\frac{-k_{ic}}{L_f} & 0 & \frac{k_a\omega_a}{L_f} & 0 & \frac{240}{L_fT_d^{\,3}} & 0 & \frac{24}{L_fT_d} & 0 & 0 & 0 & \left(\frac{-r_f+k_{pc}}{L_f}+\frac{k_{pc}k_{pd}I_{fd}}{C_{dc}V_d}\right) & \left(\omega_1+\frac{k_{pc}k_{pd}I_q}{C_{dc}V_d}\right) & 0 & 0 & -\frac{k_{pc}}{L_f} & 0 & \frac{k_{pc}k_{pd}V_{dc}}{L_fV_d} & \left(\frac{-1-k_a}{L_f}\right) & 0 & 0 & 0 \\
0 & \frac{-k_{ic}}{L_f} & 0 & \frac{k_a\omega_a}{L_f} & 0 & 0 & 0 & \frac{240}{L_fT_d^{\,3}} & 0 & \frac{24}{L_fT_d} & -\omega_1 & \left(\frac{-r_f+k_{pc}}{L_f}\right) & 0 & \frac{(k_a+1)V_d}{L_f} & 0 & \frac{-k_{pc}}{L_f} & 0 & -\frac{k_{pc}k_{pa}}{L_f} & 0 & \frac{-(k_a+1)}{L_f} & 0 \\
0 & 0 & 0 & 0 & 0 & 0 & 0 & 0 & 0 & 0 & 0 & 0 & 0 & -V_d & 0 & 0 & 0 & 0 & 0 & 1 & 0 \\
0 & 0 & 0 & 0 & 0 & 0 & 0 & 0 & 0 & 0 & 0 & 0 & k_{ip} & -k_{pp}V_{fd} & 0 & 0 & 0 & 0 & 0 & k_{pp} & 0 \\
0 & 0 & 0 & 0 & 0 & 0 & 0 & 0 & 0 & 0 & -\frac{k_{id}L_f I_{fd}}{C_{dc}V_d} & -\frac{k_{id}L_f I_{fq}}{C_{dc}V_d} & 0 & 0 & 0 & 0 & -\frac{k_{id}V_{dc}}{V_d} & 0 & 0 & 0 & 0 \\
0 & 0 & 0 & 0 & 0 & 0 & 0 & 0 & 0 & 0 & 0 & 0 & 0 & 0 & 0 & 0 & 0 & k_{ia} & 0 & 0 & 0 \\
0 & 0 & 0 & 0 & 0 & 0 & 0 & 0 & 0 & 0 & \left(\frac{V_d}{C_{dc}V_{dc}}+\frac{L_f I_{dc} I_{fd}}{(C_{dc}V_{dc})^2}\right) & \frac{L_f I_{dc} I_{fq}}{(C_{dc}V_{dc})^2} & 0 & \frac{-V_d I_{fq}}{C_{dc}V_{dc}} & 0 & 0 & \frac{I_{dc}}{C_{dc}V_{dc}} & \frac{I_{fd}}{C_{dc}V_{dc}} & 0 & \frac{I_{fq}}{C_{dc}V_{dc}} & 0 \\
0 & 0 & 0 & 0 & 0 & 0 & 0 & 0 & 0 & 0 & \frac{1}{C_f} & 0 & 0 & \frac{-I_q}{C_f} & 0 & 0 & 0 & 0 & \frac{-1}{C_f} & \omega_1 & 0 \\
0 & 0 & 0 & 0 & 0 & 0 & 0 & 0 & 0 & 0 & 0 & 0 & 0 & 0 & 0 & 0 & 0 & \frac{1}{L_g} & \frac{-r_g}{L_g} & 0 & \omega_1 \\
0 & 0 & 0 & 0 & 0 & 0 & 0 & 0 & 0 & 0 & 0 & \frac{1}{C_f} & 0 & \frac{I_{fd}}{C_f} & 0 & 0 & 0 & -\omega_1 & 0 & 0 & \frac{-1}{C_f} \\
0 & 0 & 0 & 0 & 0 & 0 & 0 & 0 & 0 & 0 & 0 & 0 & 0 & 0 & 0 & 0 & 0 & 0 & -\omega_1 & \frac{1}{L_g} & \frac{-r_g}{L_g}
\end{bmatrix}
\tag{2.38}
$$

analysis in the next Chapters. Additionally, the state matrix also contains control gains multiplied by each other, resulting in a nonlinear optimization problem in case a complete optimization will be done. Such nonlinear problem makes optimal and robust control gains calculation difficult, as they are recursive and time-consuming, and this will be discussed in Chapter 5.

2.5. Equilibrium Point Calculation

The obtained linearized state-space model can be used for stability analysis and also for control system design. However, the state matrix demands operating points such as PoC voltage and converter currents in steady-state. They can be obtained by solving the original nonlinear equations or by carrying out simulations, which are meticulous but can be time-consuming. This subsection proposes a more straightforward solution to calculate the equilibrium point based on Fig. 2.2, using the power flow equations and Kirchhoff's Laws.

$$
\begin{aligned}
&Inputs \rightarrow P, C_f, L_{g1}, L_{g2}, V_{dc}, V_{fd}, V_g \\
&X_g = \omega_1\left(\overbrace{L_{g1}+L_{g2}}^{L_g}\right), X_C = \frac{1}{C_f\omega_1}, \delta = a\sin\left(\frac{X_g.P}{V_{fd}V_g}\right), \\
&Q_{grid} = \frac{V_g}{X_g}\left(V_{fd}\cos(\delta)-V_g\right), S_{grid} = \sqrt{Q_g{}^2+P^2}, \left|I_g\right| = \frac{S_{grid}}{V_{fd}} \\
&Q_L = X_g.\left|I_g\right|^2, Q_C = \frac{V_{fd}{}^2}{X_C}, Q_{vsc} = Q_{grid}+Q_L-Q_C \\
&I_{dc} = \frac{P}{V_{dc}}, I_{fd} = \frac{P}{V_{fd}}, I_{fq} = \frac{-Q_{vsc}}{V_{fd}} \\
&Outputs \rightarrow I_{dc}, I_{fd}, I_{fq}
\end{aligned}
\tag{2.39}
$$

Based on the above equations, the power system is supposed to be stable and operate in steady-state conditions; therefore, the VSC's controllers keep the dc-link and PoC voltage at the imposed values (in this work, V_{dc}=700V, V_{fd}=V_d=400V, see in Table 2.1). Moreover, the grid inductance and VSC power level are independent inputs needed in order to run calculations and impact on the power system operating point.

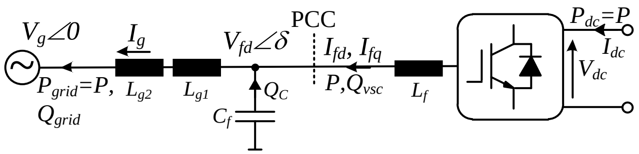

Fig. 2.2: Active and reactive power flow in a grid-connected VSC for equilibrium point calculation. Source: **[J2].**

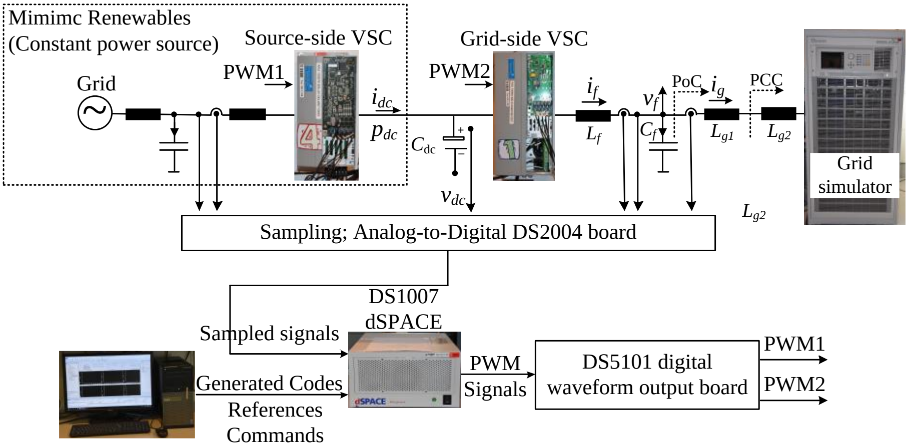

Fig. 2.3: Experimental setup used in the thesis. Source: **[J2]**

Eventually, based on the system inputs, the parameters, and the mathematical power flow model, the PoC current (I_{fd}, I_{fq}) and dc source current (I_{dc}) can be calculated. Now, all parameters and variables are available to build a model for stability in (2.38).

2.6. Simulation and Experimental Platform used in Ph.D. Project

To verify the proposed solutions in the thesis, a MATLAB Simulink model and experimental setup have been prepared. The experimental setup includes back-to-back VSCs, which are shown in Fig. 2.3. The first VSC (source-side VSC) operates in constant power to emulate a primary renewable power source. It supplies the second LCL-filtered grid-connected VSC, which contains CC, HPF-VFF, PLL, AVC, and DVC. A grid simulator (Chroma 61845) and filter inductors represent the power grid at the connection point. The main power system and control parameters are listed in Table 2.1.

It is worth remarking that a down-scaled power system is also used to mimic weak grid connections and reduce the need for large grid inductors in the experiments. For experimental implementation, a DS1007 dSPACE is employed to drive both VSCs and realize VSC controllers. In addition, an Analog-to-Digital DS2004 board and a DS5101 digital waveform output board are used to digitize sampled signals (measured current and voltage signals) and to generate PWM signals, respectively. The system and control parameters that are different from the main power circuit (in Table 2.1) are given in Table 2.2.

2.7. Summary

This chapter has provided the foundation for future analysis, suggesting a commonly used power system application of VSCs. It is discussed how the small-signal model of the whole system can be obtained and how the control system is traditionally designed. They can be used as a base case study to compare the proposed solutions suggested in this thesis. It has been observed that the small-signal model depends on the different power systems and control parameters that may be uncertain, which are impacting the conventional stability analysis and control system design.

Table 2.1: Main system and control parameters.

Power system parameters		**Control parameters**	
Nominal power (P_n)	5-10 [kW]	Conventional cascaded PI controllers	
Nominal line voltage (v_g)	400 [V]	k_{pc}, k_{ic},	9.425, 4.4e^3
Grid frequency (f_1)	50 [Hz]	k_{pp}, k_{ip}	0.22, 9.9
Filter capacitor (C_f)	10 [µF]	k_{pa}, k_{ia}	0, 4.8
Inverter-side inductor (L_f)	2-5 [mH]	k_a, ω_a	1, 6.6e^3
Grid-side inductor (L_g)	5-50 [mH]	k_{pd}, k_{id}	0.13, 2.91
Grid SCR	1-10	k_{ig}	6.1
The series resistance of C_f (r_c)	0.5 [mΩ]	Proposed optimal control method	
The series resistance of L_f (r_f)	1 [mΩ]	r, q_1	1.5, 1e^4
The series resistance of L_g (r_g)	1 [mΩ]	q_2, q_3	1, 5
DC-link capacitor (C_{dc})	1.5 [mF]	k_{pp}, k_{ip}	0.22, 9.9
DC-link voltage (v_{dc})	700 [V]	Conventional PR current controller	
Sampling and switching frequencies	10 [kHz]	k_{pc}, k_{s1}	22, 10e^3
T_d	150 [µs]	ξ_S	1
		Proposed adaptive current controller	
		a_m, b_m	4000, 4012
		γ_{ad}	20
		k_{1n}, k_{2n}	19.8, 20.1

Table 2.2: Down-scaled system and control parameters to emulate weak grid conditions in the test.

Power system parameters		**Control parameters**	
Nominal power (P_n)	5 [kW]	Conventional cascaded PI controllers	
Nominal line voltage (v_g)	172 [V]	k_{pc}, k_{ic}	7.068, 3.3e^3
Filter capacitor (C_f)	30 [µF]	k_{pp}, k_{ip}	0.51, 22.95
Inverter-side inductor (L_f)	1.5 [mH]	k_{pa}, k_{ia}	0, 30
Grid-side inductor (L_g)	1.9-19 [mH]	k_{ig}	3
DC-link voltage (v_{dc})	600 [V]	Proposed optimal control method	
		k_{pp}, k_{ip}	0.51, 22.95
		q_2, q_3	1, 1
		r, q_1	2, 1e^4
		Proposed robust H_∞ current controller	
		Performance weighting function	
		k_{s1}, k_{s5}, k_{s7}	40, 4, 4
		ξ_S, ω_n	2, 100π
		Control input weighting factor	
		k_u	0.001

Chapter 3. Stability Robustness Analysis of a Single-Converter System

3.1. Background

As discussed in the previous two chapters, power electronics-based power systems are susceptible to power system changes, uncertainties, and disturbances due to their broad wide-scale dynamics. In such a way, a slight variation in one or more of the power system parameters may give current or voltage oscillations, activate protection devices, and might lead to a power system shutdown. Therefore conducting a robustness analysis of different power system and control parameters on the system response and identifying the potential robustness issues is of utmost importance. Many research works have presented robustness analysis methods to answer these questions, usually based on analytical methods. These analytical methods are μ-analysis, Lyapunov stability analysis, LMI formulations, etc., which are helpful but suffer from some conservatism in the end-design. Moreover, providing a general framework applicable to different VSC-based power systems and doing robustness analysis is not easy at all. These methods typically rely on worst-case scenarios to determine whether system robustness requirements are satisfied under specific conditions. However, their usefulness is limited when the worst-case conditions have a low probability of occurrence. In such cases, the results may not be efficient or applicable.

This chapter provides a new general framework for a robustness analysis of PEPS. Unlike the previous solutions, the proposed one employs a probabilistic-based approach. This method measures the system stability and performance not only based on the absolute values of stability metrics but also in terms of their statistical value variation. It can consider different uncertainties and disturbances, at the same time reveal their impact on the system response, and also identify the most critical ones.

Through the consideration of the likelihood of different conditions and inputs, the obtained results are more realistic. Additionally, the probabilistic approach establishes a valuable connection between system stability studies and risk and reliability analysis, offering significant benefits from a power system design perspective.

Furthermore, the proposed solution demonstrates applicability across various PEPS applications. In particular, this chapter includes a probabilistic harmonic small-signal stability analysis, utilizing the small-signal model introduced in Chapter 2 as the base case. Notably, this concept can be seamlessly integrated with other available small- and large-signal stability models and assessment methods, providing a probabilistic and robust analysis of the system under study.

3.2. Proposed Framework for Probabilistic Stability and Performance Assessment

A probabilistic robustness analysis can be done at two levels: at the converter and at system levels. At the converter level, the grid condition at the point of connection, converter power level, and filter parameters are the main parameters subjected to variations and for study. At the system-level, since different manufacturers and vendors may provide the power converters, it may introduce additional unknown parameters from the inside of the power converter including its control system. Fig. 3.1 shows the proposed flow diagram of a probabilistic robustness assessment method to be applied in a PEPS application.

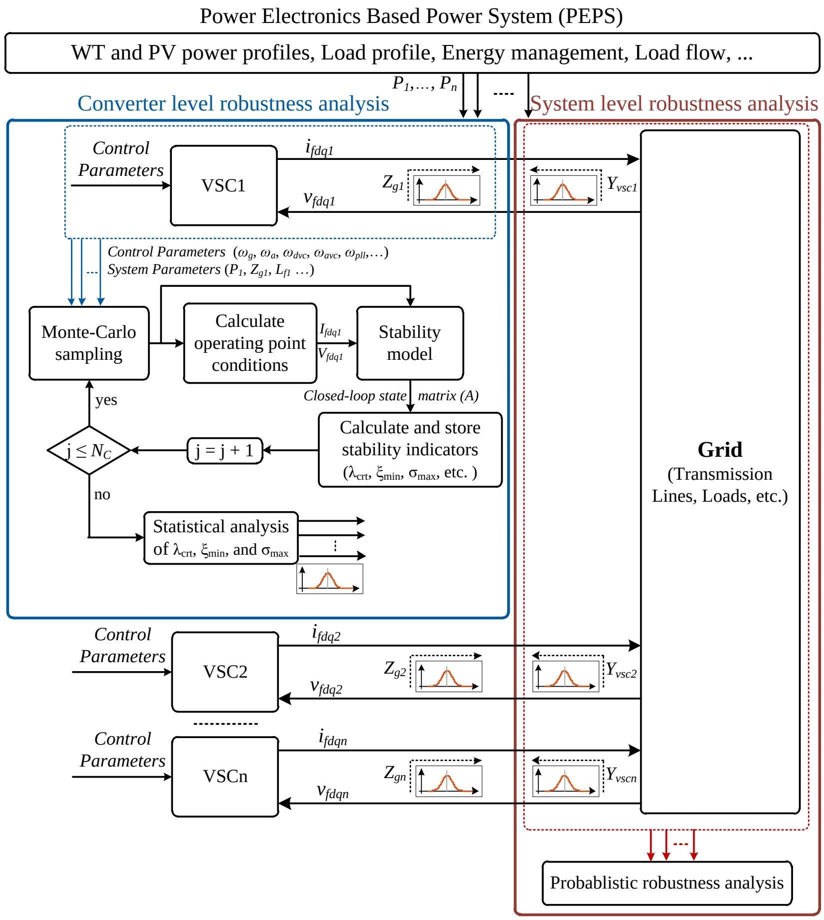

Fig. 3.1: Proposed flow diagram for probabilistic robustness analysis of PEPS, PV: Photovoltaic power system, WT: Wind turbines. Source: **[J1].**

The probabilistic robustness analysis is shown at the converter level (blue box), where a single three-phase grid-connected VSC is used. A Thevenin model represents the power grid with varying impedance (Z_{g1}) to study both strong and weak grid conditions. Additionally, the intermittent nature of renewables dictates the inverter power operation; therefore, the operating power point should be considered as an uncertain parameter that may impact the power system stability. Notably, under a weak grid condition, even slight changes in the injected power or current may cause risk of oscillations and variations in the PoC voltage, which may endanger system operation. In the proposed framework for uncertain parameters like grid impedance, a proper probability distribution function (PDF) is defined. Then, sampling methods such as Monte Carlo sampling (MC) extract the uncertain parameters from PDFs. Based on the fixed (control parameters, inverter power level) and sampled parameters (grid inductance), the power system equilibrium point is calculated, and a stability model is built. Since the chapter's main focus is on small-signal stability analysis, the stability model is a linearized state-space model derived in the previous chapter. After that, eigenvalue analysis calculates the stability and performance indices based on critical mode (λ_{crt}), damping factor (σ), and damping ratio (ξ) of the system. This procedure is repeated for N_C times to ensure a full un-mapping of the studied system. Finally, the statistical properties of the outputs (λ_{crt}, σ, and ξ) are computed, providing essential information about the system's sensitivity to parameter variations and enabling a link between stability analysis and reliability considerations.

3.3. Stability and Performance Definitions and Metrics

In power electronics-based power systems, unstable or weakly damped modes cause higher output oscillations and system instability. Therefore, it is essential to identify these crucial modes and locate them far from the hazardous area. The critical mode is the eigenvalue with the lowest damping among all eigenvalues in the system analyzed. The following complex equation can represent the system eigenvalue:

$$\lambda = \sigma \pm j\omega_d \tag{3.1}$$

where λ is an eigenvalue, σ and ω_d are its real and imaginary parts, σ is called the damping factor that represents the relative stability margin and ω_d is the frequency of oscillation. Another performance metric is the damping ratio (ξ), which is related to the system response in terms of overshoot:

$$\xi = \frac{-\sigma}{\sqrt{\sigma^2 + {\omega_d}^2}} \tag{3.2}$$

For an LTI system, the system is stable if [23]:

a) All eigenvalues of state matrix (A) are in the left half of the complex plane (LHP).

and the following definitions are equivalent:

a) All eigenvalues of *A* are in the LHP.

b) The critical mode of *A* is in the LHP.

c) The LTI system is asymptotically stable [18].

d) The LTI system is exponentially stable [83].

Moreover, the system is unstable if one or all of the following conditions happen:

a) At least one eigenvalue of *A* is in the open right half of the complex plane.

b) There are repeated eigenvalues on the imaginary axis (or equivalently, at least one of the Jordan blocks associated with such eigenvalues has a size of two or more [84]).

The system with distinct eigenvalues on the imaginary axis is neither stable nor unstable, and it is called marginally stable. However, for a grid-connected VSC, not only is the asymptotic stability required (all eigenvalues are in the LHP), but they should also have a sufficient distance to the imaginary axis to provide the desired stability margins and to avoid unacceptable overshoots.

In this regard, the damping factor should be less than a maximum value to ensure some stability margin, placing all eigenvalues in a sector like shown in Fig. 3.2(a). Also, the damping ratio should be greater than a minimum value to limit the system oscillations and overshoots, as illustrated in the wedge-shaped sector in Fig. 3.2(b). When both requirements are requested simultaneously, the closed-loop eigenvalues are located in the D-shape sector in Fig. 3.2(c).

Consequently, considering the required conditions on the damping factor and ratio and whether system uncertainties are included or not, the following four descriptions for nominal and robust stability and performance are given:

Nominal Stability (NS): The critical mode is in LHP when the plant is known, and there are not any uncertainties, i.e.,

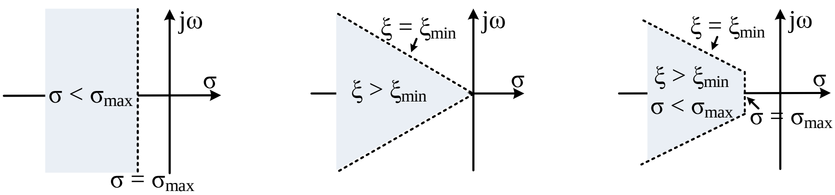

(a) Region on the left side of the complex plane for $\sigma < \sigma_{\max}$

(b) A wedge-shape sector in the complex plane for $\xi > \xi_{\min}$

(c) A D-shape sector in the complex plane for $\sigma < \sigma_{\max}$ & $\xi > \xi_{\min}$

Fig. 3.2: Desired eigenvalue location based on the desired stability and performance specification. Source: **[J1]**

$$\begin{cases} \sigma < 0, \ \xi > 0 \\ \text{Uncertainties} = 0 \end{cases} \rightarrow \text{Nominal Stability analysis}$$

Robust Stability (RS): The critical mode remains in LHP considering power system uncertainties, i.e.,

$$\begin{cases} \sigma < 0, \ \xi > 0 \\ \text{Uncertainties} \neq 0 \end{cases} \rightarrow \text{Robust Stability analysis}$$

Nominal Performance (NP): The power system fulfills the stability and performance requirements, and there are not any uncertainties, i.e.,

$$\begin{cases} \sigma_{\min} \leq \sigma \leq \sigma_{\max}, \ \xi_{\min} \leq \xi \leq \xi_{\max} \\ \text{Uncertainties} = 0 \end{cases} \rightarrow \text{Nominal Performance analysis}$$

Robust Performance (RP): The power system fulfills the stability and performance requirements considering power system uncertainties, i.e.,

$$\begin{cases} \sigma_{\min} \leq \sigma \leq \sigma_{\max}, \ \xi_{\min} \leq \xi \leq \xi_{\max} \\ \text{Uncertainties} \neq 0 \end{cases} \rightarrow \text{Robust Performance analysis}$$

3.4. Stopping Criteria for Monte Carlo (MC) Sampling Method

As it is shown in Fig. 3.1, in order to calculate the probabilistic characteristics of stability and performance indices, the proposed procedure should be repeated N_C times for N_C selections of uncertain parameters. It is believed that increasing the number of random samples (N_C) improves the accuracy of the calculated statistical properties of outputs, however, it is at the expense of the higher computational time and burden. Therefore, the selection of N_C compromises balance between accuracy and computations. Fig. 3.3 shows the error of the estimated mean value of the damping factor for different iteration numbers.

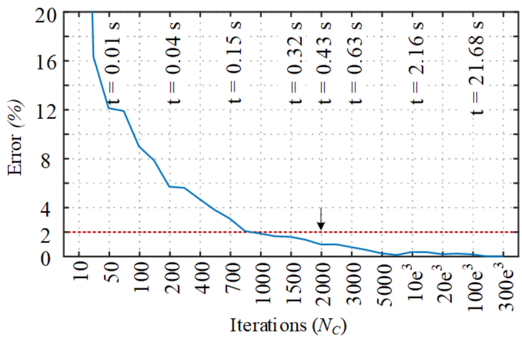

Fig. 3.3: The impact of the number of iterations on both the accuracy of mean value estimation for the damping factor and the time required to complete calculations. (a single-converter system, SCR=1.67, p_{vsc} = 10 kW). Source: **[J1]**

Moreover, the required time to complete calculations for some cases is also given. As it can be seen, N_C equal to 2000 can provide a good compromise between time and accuracy. In such a way, the expected estimated error is lower than 2% while the computational time is sufficiently low.

Similar conclusions can be obtained for other stability metrics and power system conditions, which are not given here in order to avoid repeated discussion and keep this subsection short.

3.5. Results of Probabilistic Stability and Performance Analysis

As previously mentioned in Fig. 3.1, the proposed flow diagram for probabilistic stability and performance assessment can be applied to different PEPS. This chapter has selected a three-phase grid-connected VSC as an example system, which was also discussed in details in the previous chapter. This power system provides the possibility of examining high-frequency oscillations due to the current controller, control delay, and the LCL filter resonances as well as low-frequency oscillations due to the voltage controller, PLL, and weak grid conditions (variable SCR).

In continue, it will be shown how the new framework for probabilistic stability analysis can be applied to the example system and how to interpret the findings. In this respect, the impact of grid SCR variations, operating point changes, and different PLL bandwidths on the system response are investigated. It tries to widen the available knowledge on robustness analysis and provide a probabilistic perspective of such a system design.

3.5.1. Impact of Grid SCR Variations

This subsection aims to examine how grid SCR changes affect the stability and performance of the power system. In this regard, five different values for grid SCR (SCR=10, 5, 2.5, 2, and 1.67) are assumed to cover all possible conditions in practice. It is worth noting that an SCR > 5 introduces a strong grid, 2<SCR<3 corresponds to a weak grid, and SCR < 2 represents an ultra-weak grid [85]. The following equation represents the relationship between grid SCR and inductance.

$$L_g = \frac{L_b}{SCR} \tag{3.3}$$

Here L_b is the base grid inductance in a per-unit system, and $L_g = L_{g1} + L_{g2}$.

For grid inductance corresponding to each SCR level, a proper PDF is defined. PDF's mean value is the nominal grid inductance. The PDF's standard deviation is 6.67% of the mean value; therefore, 99.7% of the randomly sampled inductances are within ±80% of the mean value. Fig. 3.4 shows the calculated PDFs for different grid SCRs and inductances. After representing the system uncertainties by statistics, the next step would be to employ the proposed flow diagram for probabilistic robustness analysis shown in Fig. 3.1. Here, the Monte Carlo sampling method extracts random values of the uncertain parameters from the defined PDFs. Using the sampled and fixed parameters, the power system operational point in (2.39) and the stability model in (2.38) are calculated. Then the eigenvalue analysis evaluates the critical mode based on the available data and the stability model. These actions are repeated N_C times, and the final results are summarized and demonstrated in Fig. 3.5.

Furthermore, the statistical properties of the critical mode and its damping factor and ratio can also be evaluated and plotted, which will be discussed in the following.

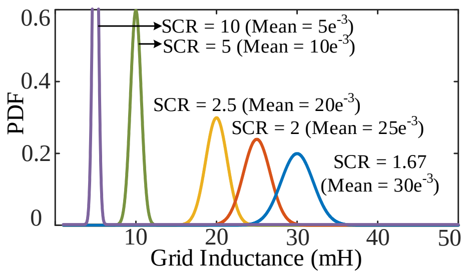

Fig. 3.4: Considered PDFs of grid inductance for different grid SCR levels. Source: **[J1]**

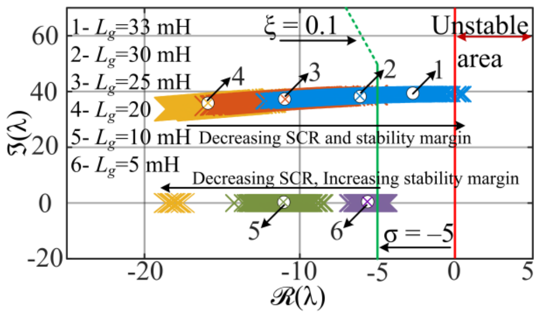

Fig. 3.5: Critical mode locations in the complex plane, calculated based on the defined grid impedance PDFs. The colors match the distribution in Fig. 3.4. Source: **[J1]**

a) Nominal and robust stability and performance comparison:

As elaborated, the system status can be analyzed in terms of nominal and robust stability and performance parameters (*NS*, *RS*, *NP*, and *RP*). In Fig. 3.5, the white circles containing colored multiplication signs demonstrate where the critical mode is located for the mean value of the PDFs or the grid inductance nominal value. Moreover, the colored lines show the critical mode locations under grid inductance variations. The desired relative stability margin or maximum damping factor is selected as -5 sec^{-1}, and the desired minimum damping ratio is equal to 10%. Green lines depict these stability and performance specifications, and the red line separates stable and unstable areas.

For example, for the grid SCR equal to 10, the following can be concluded from Fig. 3.5. The critical mode under nominal grid inductance (white circle with purple sign) meets both red and green lines, ensuring nominal stability and performance. On the other hand, under grid inductance uncertainties, the critical mode locations (purple curves) do not cross the red line and do the green lines, meaning the power system has robust stability but does not have robust performance. Similar conclusions can be reached out for other SCRs and they are outlined in Table 3.1.

Table 3.1: Different defined stability and performance metrics by evaluating system response for various grid SCRs (P=P_n).

	SCR				
Indexes	**10**	**5**	**2.5**	**2**	**1.67**
Nominal stability (NS)	+	+	+	+	+
Nominal performance (NP)	+	+	+	+	+
Robust performance (RS)	+	+	+	+	-
Robust stability (RP)	-	+	+	+	-

b) Discussion on critical mode locus in the complex plane

Fig. 3.5 shows critical mode location under different grid SCRs. Under a lower grid SCR, they can cover a larger area in the complex plane, resulting in higher sensitivity to grid impedance variations. Moreover, two different behaviors are observed when grid SCR changes from 10 to 2.5 and then from 2.5 to 1.6. At first, the stability margin is improved, then decreased by further reducing SCR. The main reasons behind that are as follows.

As discussed in [86], an inverter-side current control-based VSC has better stability margins under lower grid SCR than the higher ones. In this respect, reducing SCR from 10 to 2.5 improves the stability margin. Nevertheless, if SCR is reduced further, it may cause higher interaction between VSC and the power grid because of the synchronization mechanism and higher grid inductances. A participation factor analysis can validate the above discussion.

As given in Table 3.2, the AVC substantially affects the maximum damping factor under higher SCRs. For example, as it can be seen from this table, for SCRs equal to 10 and 5 and when the power is nominal (P=P_n), the participation factor (PF) of AVC state on the critical mode damping factor is 99% and 97% (red box), respectively, which confirm the high contribution of AVC on the maximum damping factor. The same conclusion can be drawn for other power levels as well.

In this situation, the AVC has a lower bandwidth among all control loops, which may lead to performance degradation. Moreover, the maximum damping factor can be estimated by $\sigma_{\max} = -\omega_{B,AVC} = -k_{ia}.\omega_1.L_g$ [62]. Accordingly, higher SCR (smaller grid inductance) results in a smaller stability margin.

Table 3.2: Participation factor analysis of critical modes for different grid SCRs and power levels. Source: **[J1]**

SCR	10	5	2.5	2	1.67
			P = 0.05P$_n$		
Damping Factor	AVC(.99)	AVC(.99)	AVC(.92)	AVC(.8), DVC(.13)	CC(.46), i_{gdq}(.23), PLL(.07), AVC(.06), APB(.09)
Damping Ratio	HPF(.3), Delay(.27), i_{fdq}(.17), v_{fdq}(.13)	HPF(.33), Delay(.22), i_{fdq}(.21), v_{fdq}(.13)	HPF(.33), Delay(.22), i_{fdq}(.21), v_{fdq}(.13)	CC(.47), i_{gdq}(.25), PLL(.06), AVC(.05), APB(.08)	CC(.46), i_{gdq}(.23), PLL(.07), AVC(.06), APB(.09)
			P = 0.25P$_n$		
Damping Factor	AVC(.99)	AVC(.99)	AVC(.92)	AVC(.73), DVC(.18)	CC(.46), i_{gdq} (.23), PLL(.08), AVC(.06), APB(.08)
Damping Ratio	HPF(31), Delay(.26), i_{fdq}(.17), v_{fdq}(.14)	HPF(.34), Delay(.21), i_{fdq}(.22), v_{fdq}(.13)	HPF(.34), Delay(.2), i_{fdq}(.25), v_{fdq}(.13)	CC(.46), i_{gdq}(.25), PLL(.06), AVC(.05), APB(.08)	CC(.46), i_{gdq}(.23), PLL(.08), AVC(.06), APB(.08)
			P = 0.5P$_n$		
Damping Factor	AVC(.99)	AVC(.97)	DVC(.1), AVC(.87)	PLL(.56), AVC(.07), DVC(.13), APB(.22)	CC(.46), i_{gdq}(.23), PLL(.08), AVC(.06), APB(.08)
Damping Ratio	HPF(.31), Delay(.27), i_{fdq}(.16), v_{fdq} (.13)	HPF(.33), Delay(.22), i_{fdq}(.2), v_{fdq}(.13)	HPF(.34), Delay(.2), i_{fdq}(.24), v_{fdq}(.13)	CC(.45), i_{gdq}(.24), PLL(.1), AVC(.05), APB(.07)	CC(.46), i_{gdq}(.23), PLL(.08), AVC(.06), APB(.08)
			P = 0.75P$_n$		
Damping Factor	AVC(.99)	AVC(.97)	PLL(.44), AVC(.08), DVC(.17), APB(.21)	PLL(.42), AVC(.12), DVC(.16), APB(.21)	PLL(.4), AVC(.15), DVC(.15), APB(.21)
Damping Ratio	HPF(31), Delay(.27), i_{fdq}(.17), v_{fdq} (.14)	HPF(.33), Delay(.23), i_{fdq}(.2), v_{fdq}(.14)	HPF(.35), Delay(.2), i_{fdq}(.24), v_{fdq}(.14)	CC(.46), i_{gdq}(.24), PLL(.08), AVC(.05), APB(.07)	CC(.46), i_{gdq}(.23), PLL(.2), AVC(.06), APB(.08)
			P = P$_n$		
Damping Factor	AVC(.99)	AVC(.97)	PLL(.37), AVC(.13), DVC(.18), APB(.23)	PLL(.35), AVC(.16), DVC(.16), APB(.22)	PLL(.33), AVC(.2), DVC(.14), APB(.21)
Damping Ratio	HPF(.31), Delay(.27), i_{fdq}(.2), v_{fdq} (.14)	HPF(.33), Delay(.22), i_{fdq}(.22), v_{fdq}(.14)	HPF(.33), Delay(.22), i_{fdq}(.22), v_{fdq}(.14)	CC(.45), i_{gdq}(.24), PLL(.1), AVC(.05), APB(.07)	CC(.45), i_{gdq}(.24), PLL(.1), AVC(.06), APB(.08)

Interpretation example: for the case of SCR = 10 and P=Pn (orange box), the participation factor (PF) of AVC state on the critical mode damping factor is 99%. Moreover, HPF and Delay have a higher contribution to the minimum damping ratio, their PF are 31% and 27% respectively.

It is worth to remark that the AVC bandwidth approximately changes from 5.4 rad/s (0.85 Hz) to 21.5 rad/s (3.5 Hz) when the grid SCR varies from 10 to 2.5 using fixed control parameters. Therefore, by further SCR reduction (e.g., SCR<2.5), the AVC bandwidths become close to the other slow outer control loops (PLL, DVC, etc.); consequently, the interaction between different control loops, and not only AVC, leads to stability issues and performance degradation. For example, in the case of SCR=1.67 and P=P_n (green box in Table 3.2), the participation factor of PLL, AVC, DVC, and APB on the maximum damping factor are 33%, 20%, 14%, and 21% respectively, which confirm the contribution of all controllers on the damping factor and severe control loop interaction under lower grid SCR.

In summary, in strong grids, the AVC has the most contribution to the critical mode, and under weak ones, the interaction between different control loops is the main reason, as discussed in the above analysis.

c) Critical mode statistical representation

An interesting feature of probabilistic stability assessment is providing the statistical characteristics of the stability indices. They can provide information on the sensitivity to uncertain parameters and the likelihood of the desired performance.

Fig. 3.6 shows PDF and CDF of damping factor and ratio under a wide range of grid SCRs.

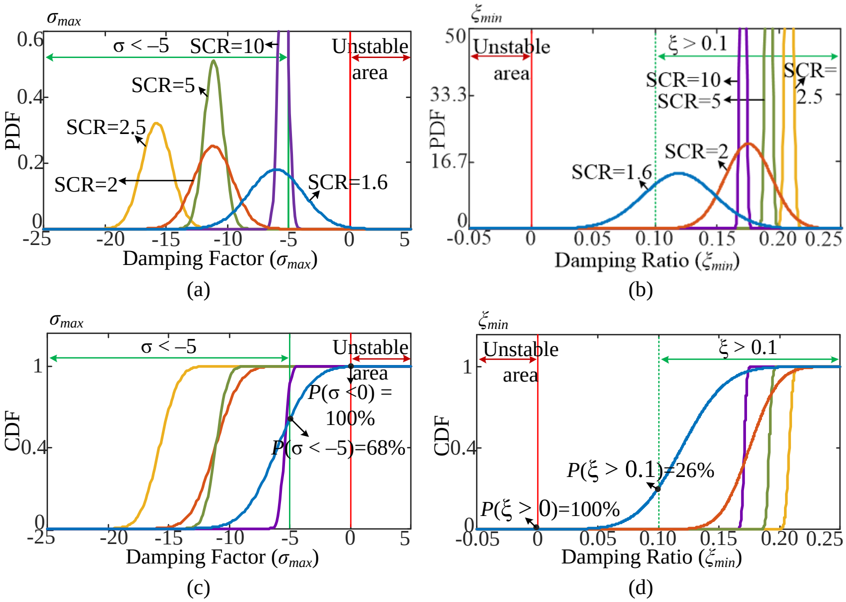

Fig. 3.6: Probability density functions (PDFs) and cumulative density functions (CDFs) of maximum damping factor and minimum damping ratio for different grid SCRs, (a) PDFs of σ_{max}, (b) PDFs of ξ_{min}, (c) CDFs of σ_{max}, (d) CDFs of ξ_{min}. The colors match the distribution in Fig. 3.4. Source: **[J1]**

As it can be seen, PDFs under a strong grid are narrow, which indicates lower sensitivity. On the other hand, they become wider under weak grids meaning higher dependencies to grid inductance variations. As in the previous section, the same conclusion can be drawn for the impact of grid SCRs on the damping factor and ratio. It is worth to add that the damping factor and ratio are generally affected by the slower and faster dynamics of the control system, respectively (Table 3.2).

CDFs can also give information about the likelihood of system stability, instability, or other conditions. For example, risk index of small-signal stability (RIS) can be defined as $P(\sigma \geq 0)$ or $P(\zeta \leq 0)$. From Fig. 3.6 $P(\sigma < 0) = 100\%$, which means the RIS is zero for all considered grid conditions, and the system is always stable. Or for instance, the probability of desired damping factor $(\sigma < -5)$ for the weakest SCR (SCR =1.67) is 68%, and for the remaining SCRs is 100%.

In contrast, the deterministic methods can not measure how much the system is stable or not and what is the likelihood of a specific condition.

3.5.2. Impact of Inverter Power Level

This subsection studies the impact of different inverter operating power levels on the stability and performance indicators. Hence, five values for inverter power levels are considered to study the probabilistic assessment.

a) Damping factor analysis

As it can be seen from Fig. 3.7, when the power grid is strong, the damping factor is unaffected by the inverter power level. Conversely, different behaviors are observed under weak grid conditions. By increasing the inverter power level, the damping factor is first improved. It is then reduced under the higher power levels close to the nominal one. The main reason is the same as the previous discussions. The inverter observes lower SCR under a higher power, which means a better stability margin for the inverter side current controller. However, it reduces again at a higher power capacity due to higher interaction between VSC and the power grid and the different control loops.

Additionally, the AVC significantly influences the damping factor under strong grid conditions. Under weak grid conditions, fast and slow dynamics parts have the most impact on the damping factor at lower and higher power levels, respectively, as participation factor analysis in Table 3.2 shows.

b) Damping ratio analysis

Again the same as the damping factor, the damping ratio is least influenced by the inverter power level at a strong grid and higher influenced at a weak one. Moreover, under a weak grid, the current controller is the most influential one. The seen SCR is reduced by increasing the power level, and the stability margin increases. Under a strong grid, HPF-VFF and delay are the most influential ones.

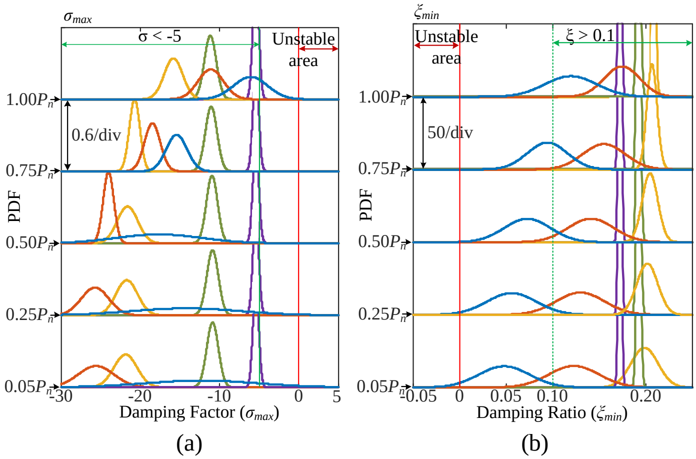

Fig. 3.7: Probability density functions (PDFs) of (a) maximum damping factor and (b) minimum damping ratio. The colors match the distribution in Fig. 3.4. Source: **[J1]**

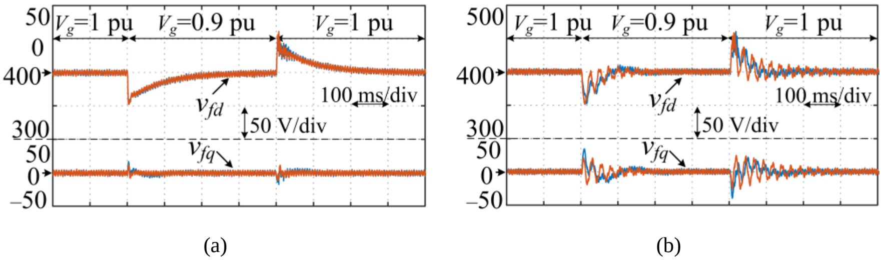

Fig. 3.8: Simulated system output when grid voltage amplitude changes by 10% under two different VSC power levels (p_{vsc}=0.25P_n (orange) and p_{vsc}=0.75P_n, (blue)), (a) SCR=5, (b) SCR=1.67. Source: **[J1]**

c) Time-domain simulations

Simulations in Fig. 3.8 have been prepared to validate the previous analytical results. They show system responses under different grid SCRs and inverter power levels when a 10% voltage sag happens. As shown under the strong grid condition, the system response is not influenced by inverter power levels. Conversely, different responses under different power levels can be observed under weak grid conditions in response to the grid voltage sag.

3.5.3. Impact of Different PLL Bandwidths

This subsection explores the impact of PLL bandwidth on the stability metrics. Unlike the grid SCR and power level, the PLL bandwidth is usually a fixed control parameter. However, nowadays, the control system may be equipped with adaptive or gain-scheduling PLL to support power grids under faulty conditions and enhance the transient response. In addition, it can disclose the importance of the optimal and robust control system design to ensure stability and performance specifications over power system uncertainties variations.

In this regard, five values for PLL bandwidths are supposed, and then the proposed probabilistic assessment method is conducted for each value to investigate system robustness under changeable grid conditions. The results are summarized in Fig. 3.9 and Table 3.3, and they are explained in the following:

a) Damping factor analysis

As shown in Fig. 3.9, the PDFs are very narrow under very low PLL bandwidth, indicating lower sensitivity to grid inductance variations. Yet, the stability margin is also small and not acceptable. In this situation, as the participation factor is shown in Table 3.3, the PLL bandwidth mainly contributes to the critical mode. Consequently, it can be expected that the stability margin will improve by increasing the PLL bandwidth. The stability margin increases by increasing the PLL bandwidth to 8 Hz. However, if the PLL bandwidth rises further, it may lead to poorer stability due to higher power grid coupling and control loops interaction.

b) Damping ratio analysis

As demonstrated in Fig. 3.9, the damping ratio is not affected by the PLL bandwidth under strong grid conditions. On the other hand, increasing the PLL bandwidth worsens the stability margin under weak grid conditions. For instance, in the case of a grid with an SCR of 2.5, faster dynamics (such as HPF and delay) and slower dynamics (like CC and PLL) play a significant role in determining the minimum damping ratio for both lower and higher PLL bandwidths.

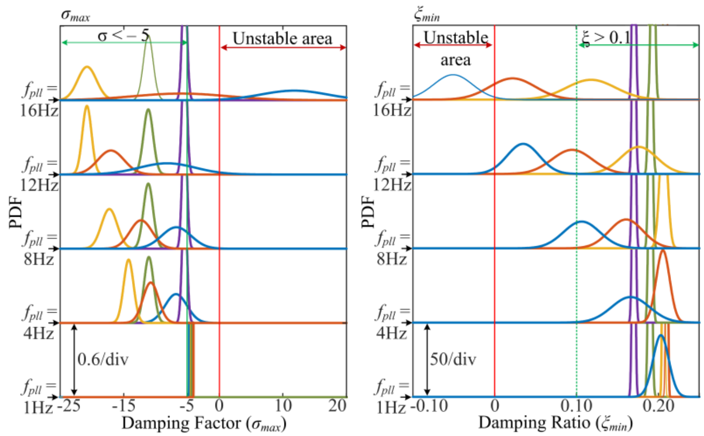

(a) (b)

Fig. 3.9: Probability density functions (PDFs) of (a) maximum damping factor and (b) minimum damping ratio for different grid SCRs and PLL bandwidths. The colors match the distribution in Fig. 3.4. Source: **[J1]**

Table 3.3: Participation factor analysis of critical modes for different grid SCR and PLL bandwidths (P=P_n). Source: **[J1]**

SCR	10	5	2.5	2	1.67
			f_{PLL} = 1 Hz		
Damping Factor	PLL(.99)	PLL(.99)	PLL(.97)	PLL(.94)	PLL(.92)
Damping Ratio	HPF(.31), Delay(.27), i_{fdq}(.16), v_{fdq}(.14)	HPF(.33), Delay(.22), i_{fdq}(.22), v_{fdq}(.14)	HPF(.34), Delay(.21), i_{fdq}(.24), v_{fdq}(.14)	HPF(.34), Delay(.2), i_{fdq}(.25), v_{fdq}(.13)	CC(.52), i_{gdq}(.23), PLL(.02), AVC(.06), APB(.09)
			f_{PLL} = 4 Hz		
Damping Factor	AVC(.99)	AVC(.96)	PLL(.5), DVC(.16), AVC(.14), ABP(.14)	PLL(.42), DVC(.16), AVC(.18), ABP(.16)	PLL(.38), DVC(.14), AVC(.21), ABP(.17)
Damping Ratio	HPF(.3), Delay(.27), i_{fdq}(.16), v_{fdq}(.14)	HPF(.33), Delay(.23), i_{fdq}(.21), v_{fdq}(.14)	HPF(34), Delay(.2), i_{fdq}(.24), v_{fdq}(.14)	HPF(.34), Delay(.2), i_{fdq}(.25), v_{fdq}(.14)	CC(.48), i_{gdq}(.22), PLL(.05), AVC(.06), APB(.09)
			f_{PLL} = 8 Hz		
Damping Factor	AVC(.99)	AVC(.96)	PLL(.34), DVC(.2), AVC(.11), APB(.26)	PLL(.33), AVC(.19), DVC(.17), APB(.24)	PLL(.31), DVC(.14), AVC(.19), APB(.23)
Damping Ratio	HPF(.31), Delay(.27), i_{fdq}(.17), v_{fdq}(.14)	HPF(.34), Delay(.23), i_{fdq}(.2), v_{fdq}(.14)	HPF(.34), Delay(.2), i_{fdq}(.25), v_{fdq}(.14)	CC(.45), i_{gdq}(.24), PLL(.1), AVC(.05), APB(.07)	CC(.43), i_{gdq}(.23), PLL(.1), AVC(.06), APB(.08)
			f_{PLL} = 12 Hz		
Damping Factor	AVC(.99)	AVC(.96)	PLL(.01), DVC(.25), AVC(.71), APB(.01),	PLL(.19), DVC(.22), AVC(.15), APB(.32),	CC(.38), i_{gdq}(.2), PLL(.16), AVC(.06), APB(.07),
Damping Ratio	HPF(.31), Delay(.27), i_{fdq}(.17), v_{fdq}(.14)	HPF(.33), Delay(.22), i_{fdq}(.21), v_{fdq}(.14)	CC(.42), i_{gdq}(.26), PLL(.12), AVC(.05), APB(.07)	CC(.4), i_{gdq}(.25), PLL(.14), AVC(.05), APB(.07)	CC(.38), i_{gdq}(.24), PLL(.15), AVC(.06), APB(.08)
			f_{PLL} = 16 Hz		
Damping Factor	AVC(.99)	AVC(.97)	PLL(.37), APB(.23), DVC(.18), AVC(.13)	PLL(.35), APB(.22), DVC(.16), AVC(.16)	PLL(.33), APB(.21), AVC(.2), DVC(.14)
Damping Ratio	HPF(.31), Delay(.26), i_{fdq}(.16), v_{fdq}(.14)	HPF(.33), Delay(.22), i_{fdq}(.22), v_{fdq}(.14)	CC(.38), i_{gdq}(.26), PLL(.19), AVC(.03), APB(.05)	CC(.35), i_{gdq}(.26), PLL(.21), AVC(.05), APB(.06)	CC(.32), i_{gdq}(.25), PLL(.24), AVC(.06), APB(.07)

Interpretation example: for the case of SCR = 10 and f_{PLL}=16 Hz (red box), the participation factor (PF) of AVC state on the critical mode damping factor is 99%. Moreover, HPF and Delay have a higher contribution to the minimum damping ratio, their PF are 31% and 26% respectively.

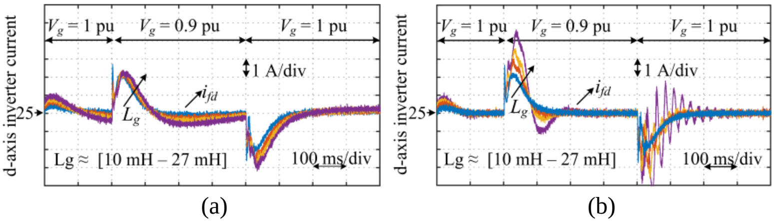

Fig. 3.10: Simulated d-axis current waveforms of VSC under grid inductance variations when 10% grid voltage sag is applied (p_{vsc} = 10 kW), (a) f_{PLL}=1 Hz, (b) f_{PLL} =12 Hz. Colors show the system response under different grid inductances [10 mH – 27 mH]. Source: **[J1]**

c) Time-domain simulations

The previous analytical discussion has been evaluated through several simulation runs. Fig. 3.10 shows the system response for a low and high PLL bandwidth (f_{PLL} = 1 and 12 Hz) over grid inductance uncertainties and 10% voltage sag. As shown, under lower PLL bandwidth, the system response is not affected by different grid inductance values.

However, the transient response takes longer to reach the steady-state operational point. On the contrary, as expected, the transient response is faster for a higher PLL bandwidth. However, it is considerably affected by the grid inductance values. Under higher PLL bandwidths and grid inductances, the coupling between VSC and the power grid significantly increases, and it may cause higher oscillations and eventually give system instability.

3.6. Experimental Verification

The experimental tests are shown in Fig. 3.11 and Fig. 3.12, which consider all discussed situations and different operational conditions such as strong and weak grids (SCR= 5.3 and 1.6), nominal and lower power levels (p_{vsc}= 5 kW and 2.5 kW), and fast and slow PLL bandwidths (f_{PLL}= 8 and 24 Hz). As depicted, the stability is not influenced by the inverter power level and PLL bandwidth in a strong grid. In contrast, the inverter power level affects the system response under weak grid conditions which is especially seen by Fig. 3.11.

Moreover, lower grid SCR restricts the possibility of employing a fast PLL. Therefore, experimental results based on a down-scaled power system have verified the time-domain simulations and analytical discussion in the previous sections.

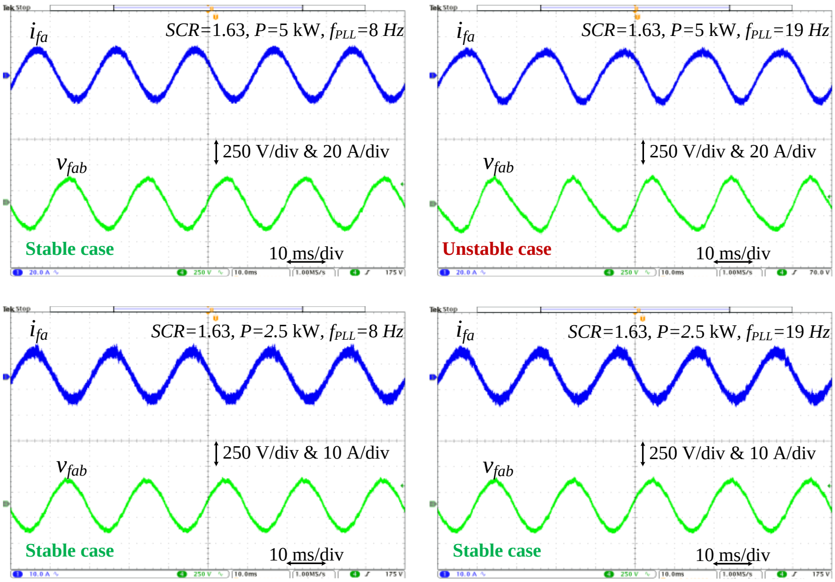

Fig. 3.11: Experimental time-domain results of the system output under different power levels (p_{vsc}=5 kW, 2.5 kW) and PLL bandwidths (f_{PLL}=8 Hz, 19 Hz) when a weak grid (SCR=1.63) is considered. Source: **[J1]**

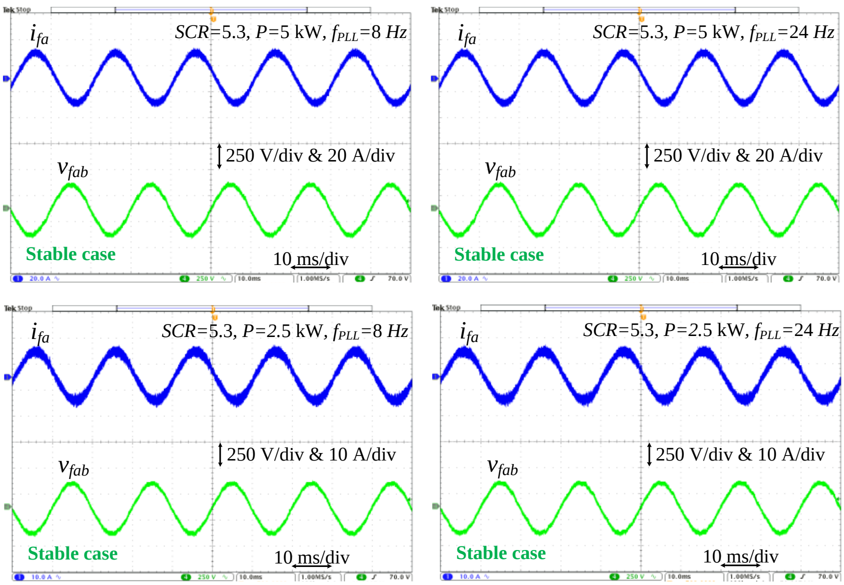

Fig. 3.12: Experimental time-domain results of the system output under different power levels (p_{vsc} =5 kW, 2.5 kW) and PLL bandwidths (f_{PLL}=8 Hz, 24 Hz) when a strong grid (SCR=5.3) is considered. Source: **[J1]**

3.7. Summary

So far, other research work works have been reported on a stability analysis of grid-connected VSCs, as referenced in the introduction. However, this research tries to widen the existing knowledge on the robustness analysis of power electronics-based power systems (PEPS) and provide a new probabilistic perspective. In this regard, it is first shown how a proposed robustness framework can be applied and how to interpret the findings on an example system. It can give the likelihood of the desired condition and relate the system stability studies to a risk and reliability evaluation.

Related Publications:

[J1] **H. Gholami-Khesht**, P. Davari, M. Novak, and F. Blaabjerg, "A probabilistic framework for the robust stability and performance analysis of grid-tied voltage source converters," *Appl. Sci.*, vol. 12, no. 15, p. 7375, 2022, doi: 10.3390/app12157375.

Main Contributions in the paper are:

This work involves proposing a general probabilistic framework for robustness analysis and presenting implementation guidelines. It also delves into the interpretation of obtained results, clarifying various aspects of probabilistic robustness assessment. Additionally, it identifies robustness issues and crucial parameters contributing significantly to system robustness.

Chapter 4. Robust Control Methods for Inner Control Loop Design of PEPS

4.1. Background

The previous two chapters have done modeling of power converters as well as robust stability and performance assessment of a single grid-connected voltage source converter (VSC). The procedure is helpful when evaluating the small-signal stability and doing a performance analysis of a given system. Nevertheless, as revealed in the robustness analysis, the system response may not be satisfying due to modern power system characteristics and unavoidable uncertainties. Hence a control system that fulfills the necessary stability and performance requirements under any conditions is needed (e.g., unknown or variable filter and grid impedances). Consequently, this chapter aims to present more advanced control techniques that are applicable to power converters and discuss their advantages and disadvantages. These control strategies are model reference adaptive and robust H_∞ control methods as they in other cases have proven strong characteristics.

First, a direct adaptive current control for grid-connected VSCs is proposed based on the Lyapunov stability theorem. An adoption law continuously updates the control gains in such a way that the desired stability margin and response will be obtained under all conditions. In the second method, the H_∞ theorem with linear matrix inequalities (LMIs) calculates the constant current control gains, ensuring system stability under the worst-case scenario. These control strategies give advanced solutions for a fast inner control part, which is essential and also responsible for providing sufficient damping for resonances introduced by converter output filter or power grid impedance, rejecting grid voltage disturbances, reducing the adverse effect of control delay, but is also being able to produce sinusoidal current according to international power quality standards.

4.2. Direct Adaptive Current Control Method

The variability of power system conditions can affect the response of grid-connected VSCs and may lead to performance degradation or instability as elaborated in the previous chapters. Adaptive control methods try to handle this issue by continuously updating the control gains during the system operation.

4.2.1. Proposed Direct Adaptive Current Control Method

Fig. 4.1 depicts block diagram of the understudy system and the proposed control structure. The power system includes a single grid-connected VSC with an inductor lowpass filter at the output. The main goal of the control system is to produce the VSC output current with a desired and predefined closed-loop response, where variations in the filter are considered. The proposed control structure includes three main parts to meet this goal, (1) a reference model to generate the desired closed-loop response (i_m), (2) an adaption law to update the control gains to compensate for parameter variations, and (3) state-feedback controller to calculate the VSC reference voltage based on the updated control gains. Based on this figure, the system dynamics can be written as follows:

$$\begin{cases} v_{inv}(t) = r_f i_f(t) + L_f \dfrac{di_f(t)}{dt} + v_{pcc}(t) \\ v_{inv}(t) \approx v_{inv,ref}(t) \end{cases} \tag{4.1}$$

The reference model should have the same structure as the closed-loop system with poles and zeros at the proper places. Hence, the following can represent the reference model:

$$\frac{di_m(t)}{dt} = -a_m i_m(t) + b_m i_{f,ref}(t) \tag{4.2}$$

where, a_m introduces the required closed-loop pole, and b_m provides unity gain at the reference input frequency for the closed-loop system. i_m and $i_{f,ref}$, are desired closed-loop output current (output of the reference model, reference output) and the converter reference current (reference input).

Suppose the system parameters at (4.1) are available and known. The following feedback controller can provide the desired output as the reference model:

$$v_{inv,ref}(t) = -k_1 i_f(t) + k_2 i_{f,ref}(t) + v_{pcc}(t) \tag{4.3}$$

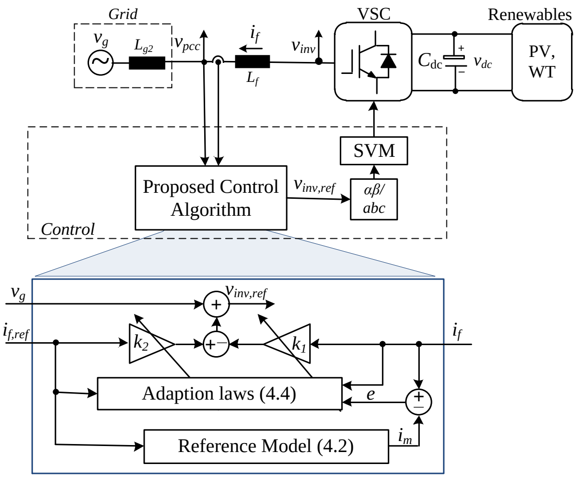

Fig. 4.1: Structure of the proposed direct adaptive current control of a grid-connected VSC. Source: **[C1].**

The pole-placement technique can calculate the nominal control gains (k_1 and k_2) based on the (4.1)-(4.3). Although the above feedback control law can provide an efficient response under the known conditions, the power system changes may deteriorate system response when using constant control gains. To overcome this challenge, adaption mechanisms are proposed as follows:

$$\begin{cases} v_{inv,ref}(t) = -k_1 i_f(t) + k_2 i_{f,ref}(t) + v_{pcc}(t) \\ \dot{k}_1 = \gamma_{ad} \cdot i_f \cdot e_{if} \\ \dot{k}_2 = -\gamma_{ad} \cdot i_{f,ref} \cdot e_{if} \end{cases} \tag{4.4}$$

Here γ_{ad} is a positive adaption gain.

The proposed control law guarantees:

1. zero tracking error and stability of the closed-loop system, even in the presence of variations in the filter inductor. (The influence of grid impedance will also be addressed.)
2. the convergence of the control gains to the desired and bounded (limited) values.

Lyapunov stability function alongside Barbalat’s lemma are applied to prove the above conclusions mathematically. Someone can refer to the paper [66] for more information.

4.2.2. Simulation and Experimental Verifications

For evaluating the performance of the proposed adaptive current control method, simulations and experiments were conducted under a variety of operational conditions. Moreover, it have been compared with the well-known proportional-resonant (PR) current control technique to further investigate the proposed control method’s effectiveness (system parameters are listed in Table 2.1). The PR current control parameters are computed using the design algorithm of [73] and [87] to have a desired closed-loop bandwidth and phase margin at 4000 rad/s and 41°, respectively. This design algorithm can guarantee acceptable performance under the nominal condition, where the exact value of the filter inductance is available.

Hence, the system’s performance can be compromised by variations in the filter. To investigate this matter, an uncertainty of +60% (mismatch) in the inductance value during the design of the PR controller is taken into account. The transient performance is then analyzed under various step changes in the reference current and compared with the proposed approach in Fig. 4.2.

This figure shows that the converter current encounters a higher overshoot (OV=11.2%), where the PR control method is employed. On the contrary, the proposed control method keeps the desired dynamic response dictated by the reference model under unknown inductances. Besides, when the reference current backs to zero, the tracking errors last longer using the PR control method compared to the proposed control method.

Fig. 4.3 presents the start-up response when the reference current changes from zero to the nominal one. There is intentionally also a 50% estimation error in the initial values of the control gains. Following the startup command, the output currents demonstrate a fast and smooth transient response, and control gains converge to bounded and desired values. There is a slight difference in the estimated values of the control gains since the correct values of filter parameters are not accurately known in practice.

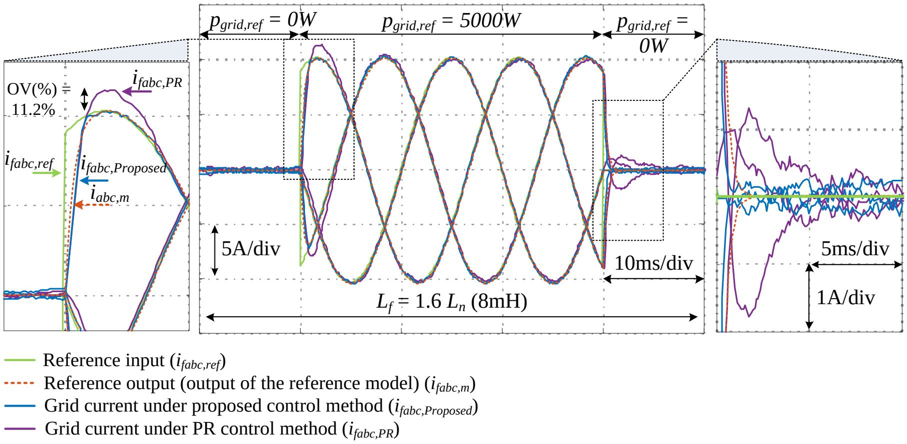

Fig. 4.2: Simulated transient performance of the proposed adaptive and PR controllers when the inductance value differs in the initial design. ($q_{grid,ref}$ = 0 Var, L_f = 1.6 L_n (8 mH)). Source: **[C1].**

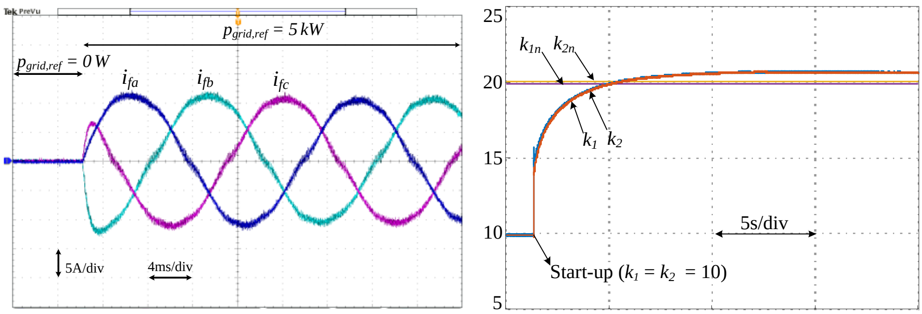

(a) (b)

Fig. 4.3: Experimental startup response of the proposed adaptive method ($q_{grid,ref}$ = 0 Var). (a): three-phase grid currents. (b): control gains convergence. Source: **[C1].**

4.2.3. Remarks to the obtained results with an adaptive method

Remark 1:

In this work, the impact of the control delay in the design process is neglected to simplify the control system design and modeling. There is usually a delay of one and a half sampling period in VSC-based power applications. One sample can be entirely compensated by employing an observer, and the remaining half sample delay can be safely ignored due to its negligible impact on the control system (where it is less than 10 percent of the control time scale or ten times faster than the inner control loop bandwidth) [73], [88]. However, it should be noted that this solution adds additional observer gains in the design process and complicates the implementation.

Remark 2:

The control system can also be used for a high-order and more complex LCL filter with a few changes for the converter- and grid-side current controllers. The voltage drop on the filter's capacitance can be treated as the grid background voltage (v_g) for the converter side controller [18], [56]. If the grid side current is controlled, some research works have proposed to neglect the filter capacitance and consider the sum of the converter- and grid-side filter inductances as well as the grid inductance as a single inductor filter with a series resistor [89], [90]. It is worth noting that this model is only a valid approximation of the filter's dynamic behavior, which is much lower than the resonance frequency in the LCL filter.

Remark 3:

It would be worth mentioning that the convergence of control gains to the desired values depends on the persistent excitation (PE) of the measured signals and the references. If the required level of PE is not fulfilled, the control gains only converge to the bounded and not the desired values. Moreover, the adaption gain should be selected carefully; they significantly impact the convergence rate of the control gains and even system response and stability. They are usually selected based on trials and errors; hence, the design procedure and implementation become more laborious when multiple uncertain parameters exist. Therefore a fixed control structure with good robustness against uncertainties is preferred, as discussed in the following section.

4.3. Robust H_∞ Current Control Method

The second control approach is a robust H_∞ current control method of a three-phase LCL-filtered grid-connected VSC to help with the mentioned shortcomings discussed in the previous subsection. A robust H_∞ technique based on delay-dependent LMIs calculates the constant current control gains under uncertain filter and grid impedances. Moreover, as a noteworthy feature, the possibility of considering the control delay in the design procedure is possible, unlike the previous method, which have such simplifying assumptions.

4.3.1. System Description and Modeling

Fig. 4.4 shows a block and circuit diagram of the three-phase LCL-filtered grid-connected VSC and the proposed robust current control method. Considering the control input delay and Kirchhoff's Laws, the system state-space equations can be written as follows:

$$\begin{cases} \dot{x}(t) = A_c x(t) + B_c v_{inv}(t) + D_c v_g(t) \\ v_{inv}(t) = v_{inv,ref}(t - \tau(t)) \end{cases} \tag{4.5}$$

where, $x = [x_1\ x_2\ x_3] = [i_f\ v_f\ i_g]$, v_{inv} and v_g, are the state vector, control input (inverter output voltage) and disturbance input (grid voltage). $\tau(t)$ is the time-varying control input delay $\tau(t) \in [0, t_d]$. Also, A_c, B_c, and D_c are state and input matrixes given as follows:

$$A_c = \begin{bmatrix} 0 & \frac{-1}{L_f} & 0 \\ \frac{1}{C_f} & 0 & \frac{-1}{C_f} \\ 0 & \frac{1}{L_g} & 0 \end{bmatrix}, B_c = \begin{bmatrix} \frac{1}{L_f} \\ 0 \\ 0 \end{bmatrix}, D_c = \begin{bmatrix} 0 \\ 0 \\ \frac{-1}{L_g} \end{bmatrix}, L_g = L_{g1} + L_{g2} \tag{4.6}$$

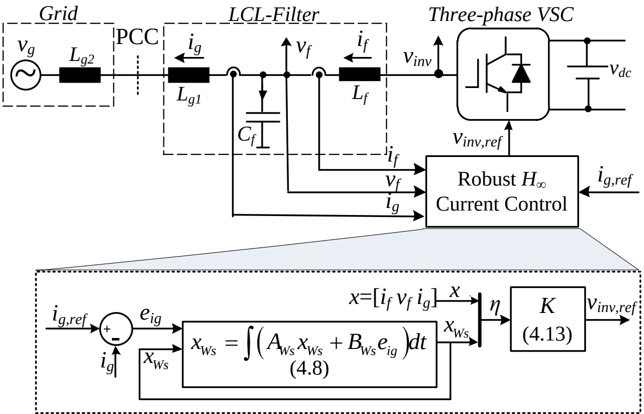

Fig. 4.4: Structure of the proposed H_∞ current control of an LCL-filtered grid-connected VSC. Source: **[C2].**

4.3.2. Proposed Robust H_∞ Current Controller

The proposed H_∞ design procedure defines the stability and performance requirements, such as control bandwidth, phase margin, noise attenuation, disturbance rejection, and tracking errors, using the performance weighting function (W_S) on the loop sensitivity function. Moreover, a constant control input weighting factor (W_{KS}) is also used to avoid difficulties regarding to high control gains. It limits the control gains' norm while not changing the overall system order. The following show the considered weighting functions:

$$W_S = \frac{y}{e_{ig}} = \sum_{n=1,5,7} \frac{k_{sn}\left(s+\xi_S\omega_n\right)}{s^2+\omega_n{}^2},\ W_{KS} = k_u \tag{4.7}$$

here, $e_{ig} = i_g - i_{g,ref}$ is the grid current tracking error, ω_n and ξ_S are a resonant frequency and a damping factor, and k_{sn} and k_u are controller gains. As it can be seen from the performance weighting function, infinite gains at the resonant frequencies (here at fundamental, fifth, and seventh components) are provided, ensuring excellent disturbance rejection capabilities and zero tracking error, when the references and disturbances are sinusoidal signals.

The performance weighting function can be rewritten in the state-space form as follows:

$$\dot{x}_{Ws}(t) = A_{Ws}x_{Ws}(t) + B_{Ws}e_{ig}(t) \tag{4.8}$$

The generalized state-space equation by including dynamics of weighting functions (4.9) in the plant state-space model (4.5) can be obtained as:

$$\begin{cases} \dot{\eta} = A\eta + Bv_{inv,ref}(t-\tau(t)) + Dw \\ z = C_1\eta + D_{12}v_{inv,ref}(t-\tau(t)) + D_{11}w \end{cases} \tag{4.9}$$

where, $\eta = \begin{bmatrix} x & x_{Ws} \end{bmatrix}$ is the state vector of the generalized model containing the plant and weighting function states in (4.5) and (4.8). $z = \begin{bmatrix} y & W_{KS}v_{inv,ref}(t-\tau(t)) \end{bmatrix}$ and $w = \begin{bmatrix} v_g & i_{g,ref} \end{bmatrix}$ represent the regulated outputs and external inputs (including references and disturbances). Matrixes *A, B, D, C_1, D, D_{11},* and D_{11} are calculated using (4.5), (4.7), and (4.8) by doing some manipulations.

a) Calculations of H_∞ Control Gain using Delay Dependent LMIs

The primary goal of the robust H_∞ technique is to find a feedback control input $\left(v_{inv,ref}(t) = K\eta(t)\right)$ that stabilizes the closed-loop system and minimizes the impact of the external inputs (w) on the regulated outputs (z) under variable uncertain grid impedances and time-varying control input delays $\left(\tau(t) \in [0, t_d], \dot{\tau}(t) \le d < 1\right)$. Here, d is the maximum variable rate of control delay.

These requirements are mathematically met by keeping the system L_2-gain norm $\left(\frac{\|z\|_{\ell 2}}{\|w\|_{\ell 2}}\right)$ less than γ_∞ for all system uncertainties as follows [38]:

$$\min_{K \ \ stabilizing} \|T_{zw}\|_\infty = \frac{\|z\|_{\ell 2}}{\|w\|_{\ell 2}} < \gamma_\infty \tag{4.10}$$

In summary, the optimization goal outlined in equation (4.10) is to determine the stabilizing control gain matrix K in a manner that reduces the influence of external disturbance inputs (w) on the regulated outputs (z). Mathematically, this entails minimizing the L_2-gain norm from z to w $\left(\frac{\|z\|_{\ell 2}}{\|w\|_{\ell 2}}\right)$. However, due to the complexity of finding the exact K that achieves this mathematical minimization, an alternate approach is taken. In such a way, a predefined lower value (γ_∞) is adopted, and the objective shifts to identifying a suitable K that ensures the L_2-gain norm of z to w remains below γ_∞ .

The subsequent proposition offers design guidelines for resolving the aforementioned optimization issue. For a comprehensive understanding of how the optimization problem is transformed into the subsequent equations and LMIs, interested readers can find detailed information in [38]. It's worth noting that, this procedure relies on the utilization of the Lyapunov-Krasovskii function (4.11) to ensure the stability of the closed-loop system.

$$\begin{cases} V\left(t,\eta,\dot{\eta}\right) = \eta^T P\eta + \int\limits_{t-t_d}^{t} \eta^T(s)S\eta(s)ds + \int\limits_{t-\tau(t)}^{t} \eta^T(s)Q\eta(s)ds + t_d \int\limits_{-t_d}^{0}\int\limits_{t+\theta}^{t} \dot{\eta}^T(s)R\dot{\eta}(s)dsd\theta > 0 \\ \dot{V} + z^T z - \gamma^2 w^T w < 0 \\ P > 0, S > 0, Q > 0, R > 0 \end{cases} \tag{4.11}$$

Equation (4.11), which is a key component, plays a significant role in this procedure. While the process involves intricate mathematical maneuvers and manipulations, the extensive proof is omitted here, and only the final outcomes are summarized and presented as the following proposition.

Proposition: Given $\gamma_\infty > 0; t_d > 0; 0 \le d < 1$ and a tuning parameter $\varepsilon > 0$, if there exist matrixes $\bar{P} > 0, \bar{P}_2 > 0, \bar{Q} > 0, \bar{R} > 0, \bar{S} > 0$ such that:

$$\begin{bmatrix} & | & D & \bar{P}_2^T C_1 \\ \bar{\varphi} & | & \varepsilon D & 0 \\ & | & 0 & 0 \\ & | & 0 & Y^T D_{12}^T \\ - & - & - & - \\ * & | & -\gamma_\infty^2 I_{2\times 2} & D_{11}^T \\ * & | & D_{11} & -I \end{bmatrix} < 0, \quad \begin{bmatrix} \bar{R} & \bar{S}_{12} \\ * & \bar{R} \end{bmatrix} > 0 \tag{4.12}$$

Here

$$\bar{\varphi} = \begin{bmatrix} \bar{\varphi}_{11} & \bar{P} - \bar{P}_2 + \varepsilon \bar{P}_2^T A^T & \bar{S}_{12} & BY + \bar{R} - \bar{S}_{12} \\ * & -\varepsilon \bar{P}_2 - \varepsilon \bar{P}_2^T + t_d^2 \bar{R} & 0 & \varepsilon BY \\ * & * & -\left(\bar{S} + \bar{R}\right) & \bar{R} - \bar{S}_{12}^T \\ * & * & * & -(1-d)\bar{Q} - 2\bar{R} + \bar{S}_{12} + \bar{S}_{12}^T \end{bmatrix} \tag{4.13}$$

$$\bar{\varphi}_{11} = A\bar{P}_2 + \bar{P}_2^T A^T + \bar{S} + \bar{Q} - \bar{R}$$

Where, this connection between matrixes in (4.11), (4.12), and (4.13) exists:

$$\begin{bmatrix} \bar{P} & \bar{R} & \bar{S} & \bar{Q} & \bar{S}_{12} \end{bmatrix} = \bar{P}_2^T \begin{bmatrix} P & R & S & Q & \bar{S}_{12} \end{bmatrix} \bar{P}_2 \tag{4.14}$$

Then the following calculates the robust static feedback control gain (K), ensuring $\dfrac{\|z\|_{\ell 2}}{\|w\|_{\ell 2}} < \gamma_\infty$:

$$\begin{cases} K = Y\bar{P}_2^{-1} \\ v_{inv,ref}(t) = K\eta(t) \end{cases} \tag{4.15}$$

Notice that (4.12) and (4.13) represent delay-dependent LMIs due to the required time delay information. It needs information on the expected maximum time delay (t_d) and its variation rate (d). Indeed, (4.12) and (4.13) ensure system stability and performance requirements for any time delay in an interval $\left(0 \le \tau(t) < t_d\right)$ with a limited variation rate to d $\left(\dot{\tau}(t) \le d < 1\right)$. Moreover, when d is selected close to zero or one, one accepts slow or fast variations in the time delay.

4.3.3. System Modeling with Polytopic Type Uncertainties

The LMIs of the proposition are affine in the system matrixes. Therefore, the obtained control gains can guarantee system stability and performance in the presence of parametric uncertainties using polytopic modeling and simultaneously solving the LMIs for all vertices.

The following equation can represent the system with polytopic-type uncertainties:

$$\Omega = \sum_{j=1}^{n} f_j \Omega_j , 0 \leq f_j(t) \leq 1, \sum_{j=1}^{n} f_j = 1, \Omega_j = \left[A^{(j)}, B^{(j)}, D^{(j)}, D_{11}{}^{(j)}, D_{12}{}^{(j)} \right] \qquad (4.16)$$

where f represents the parametric uncertainty, and the matrixes in (4.16) are represented as a convex combination of known matrixes ($A^{(j)}$, $B^{(j)}$, …,), called vertices. n is the number of vertices.

The studied system includes three parameters (L_f, C_f, L_g) which may vary. They can be initially (previously) unknown but have some intervals with known upper and lower bounds. The polytopic modeling has eight vertices corresponding to their minimum and maximum values.

$$\left\{ L_f \in \left[L_{f\min}, L_{f\max} \right], C_f \in \left[C_{f\min}, C_{f\max} \right], L_g \in \left[L_{g\min}, L_{g\max} \right] \right\} \qquad (4.17)$$

The H_∞ control gain matrix in (4.15) ensures system stability and performance, even when parametric uncertainty exists if LMIs are jointly satisfied at all vertices.

4.3.4. Remarks on the obtained results with a robust H_∞ control method

Remark 1: Design Procedure

The robust H_∞ control gain calculations can be summarized in the followings steps:

1. Represent the plant in the proper state-space form (4.5) and define control delay, uncertain parameters, and their potential intervals.
2. Choose the appropriate performance and control weighting functions based on the required bandwidth, disturbance rejection capability, steady-state error, and upper bound on the control input (4.7). In this case, selecting the number of resonators (n), desired resonant frequencies (ω_n), resonators damping factor (ξ_S), dc gain (k_{sn}), and constant weighting gain (k_u).
3. Represent the performance weighting function (4.7) in the state-space form (4.8).
4. Calculate the augmented state-space model (4.9) to include the desired stability and performance requirements in the design procedure.
5. Construct LMI in (4.12).

6. Implement LMI in (4.12) in a proper computational package. To fulfill LMI, the computational algorithm should find positive definite matrixes ($\bar{P} > 0, \bar{P}_2 > 0, \bar{Q} > 0, \bar{R} > 0, \bar{S} > 0$) using the given data by the user for $\gamma_\infty, t_d, d, \varepsilon$ and the calculated matrixes for the augmented state-space model in step 4.

   Note: If polytopic-type uncertainties are present, the LMIs need to be solved simultaneously for all vertices. This includes both the minimum and maximum values of the uncertain parameters. Here there is one uncertain parameter $\left\{L_g \in \left[L_{g\min}, L_{g\max}\right]\right\}$, therefore the LMIs in (4.12) and (4.13) should be solved simultaneously for both the minimum and maximum value of L_g.

7. Calculate the robust static feedback control gain (K) and control input $\left(v_{inv,ref}\right)$ given in (4.15).
8. Implement the proposed robust H_∞ current controller as shown in Fig. 4.4 by using (4.8) and (4.15).

Remark 2: Implementation

The LMIs can be easily solved based on user-friendly and powerful MATLAB toolboxes such as YALMIP or other standard computational packages.

Remark 3: Stability

The Lyapunov stability analysis guarantees that the H_∞ controller provides robustness for any value of an uncertain parameter belonging to the specified interval, regardless of the parameter variation rate. Therefore, the closed-loop system remains stable for any random variation rate of an uncertain parameter from the minimum to its maximum value and vice-versa. In contrast, the classical eigenvalue analysis does not guarantee stability for all parameter rate variations.

Remark 4: Generality

Eq. (4.9) shows a general state-space representation of a dynamic system; therefore, the obtained LMIs (4.12) based on that can be used to calculate robust control gain (4.15) for any other VSC-based power applications, where they are appropriately represented in this general form (4.9).

Remark 5: Examplabilty

The proposed robust H_∞ technique can systematically calculate control gains, as shown and discussed in previous sections. This provides a great opportunity to design the control system with a higher number of control gains, such as active power filters and uninterruptable power supplies, where additional resonators are needed to reduce power quality issues of nonlinear loads and distorted grids. It is worth remarking that additional resonators at the fifth and seventh harmonics in the performance weighting function (4.7) are considered to examine and validate this idea.

Remark 6: Limitation

Although the provided method and polytopic representation can consider any number of uncertain parameters from a theoretical point of view, there are some difficulties in solving the optimization problem in practice. These LMIs are usually solved based on numerical methods; therefore, they may not converge to a proper solution when the number of vertices increases. To be able to achieve a solution when the number of vertices increases, the expected system performance should be reduced (higher conservatism).

Therefore, to reduce conservatism and avoid divergence, only the most critical parameters should be considered, which have a higher impact on the system's stability and performance. In this regard, this thesis only considers grid impedance uncertainties, which may vary widely and significantly impact the system's stability. In this situation, one uncertain parameter (L_g) leads to two vertices related to its minimum and maximum values.

4.3.5. Simulation and Experimental Results

To assess the efficacy of the proposed robust H_∞ control method under various grid conditions, a MATLAB Simulink model and a laboratory setup are established using the parameters provided in Table 2.2.

Fig. 4.5 examines the steady-state performance of VSC under a severe condition, i.e., a distorted grid voltage with a high grid impedance. Even though the SCR is low (SCR=1.27, weak grid condition) and grid voltage is distorted (total harmonic distortion (THDv) equals 7.1% with 5% of the fifth and seventh components), the proposed control method effectively produces high quality and sinusoidal output currents with a low THD (THDi=1.1%).

Fig. 4.6 studies and demonstrates the system robustness under variable control delays. As it can be seen, the stability of the proposed control method is not affected when the control delay is changed from $0.75T_S$ to $1.5T_S$ and then back to $0.75T_S$, confirming the analytical results based on the Lyapunov-Krasovskii stability function as it should be stable.

Finally, Fig. 4.7 shows the (transient and) start-up response of the VSC using the proposed control method for practical implementation, where both strong and weak grid conditions are considered. The results show a fast and smooth dynamic response of the VSC current where the reference current changes from zero to nominal (step change). Even though it presents a fast dynamic response, no overshoot is observed. Moreover, the transient response takes a little longer under a lower SCR, which is rational due to the larger grid inductor. It is worth mentioning that the active power references are almost the same for both cases; however, to keep the capacitor voltage at safe limits, the reactive power references are different (-3 kVar and 1 kVar).

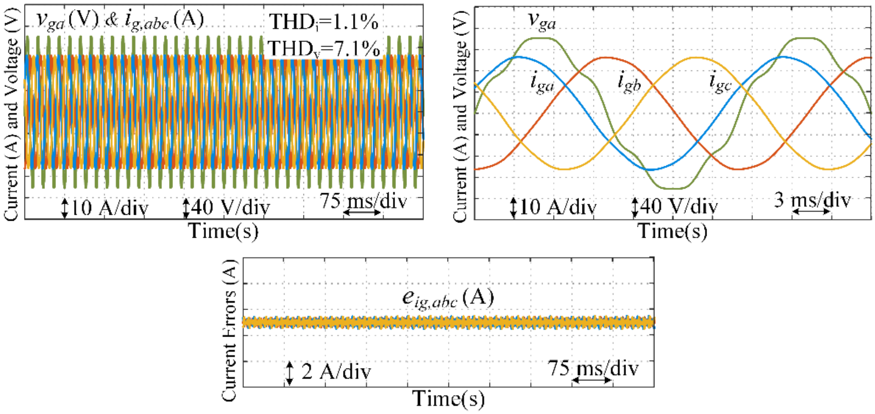

Fig. 4.5: Simulation results of the steady-state performance of the grid currents under distorted grid voltage using the proposed robust H_∞ control method, (SCR=1.26, L_g=15 mH, p_{grid} =5 kW, and q_{grid} = -2.5 kVar). Source: **[C2].**

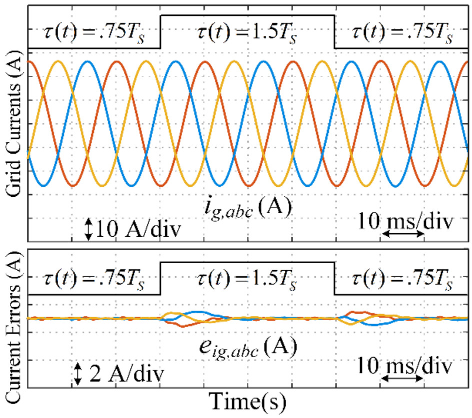

Fig. 4.6: Simulation results of the three-phase grid currents when control delay changes using the proposed robust H_∞ control method, SCR=1.26, L_g=15 mH, p_{grid} =5 kW, and p_{grid} = -2.5 kVar). Source: **[C2].**

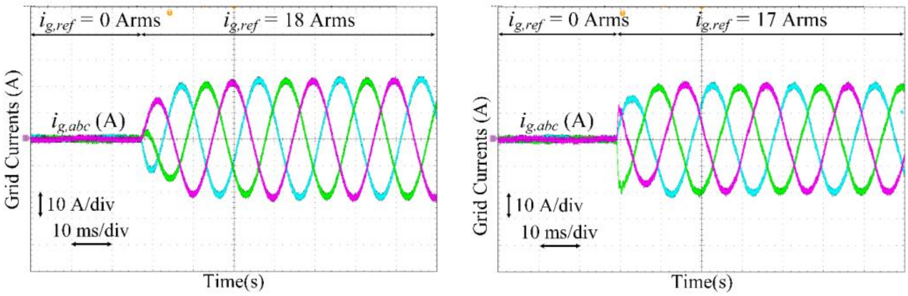

(a) (b)

Fig. 4.7: Mesured start-up of the three-phase grid currents under both weak and strong grids using the proposed robust H_∞ control method, (a) SCR=1.26 and L_g=15 mH (p_{grid} =4.5 kW, q_{grid} =-3 kVar), and (b) SCR=7 and L_g=2.7mH (p_{grid} =5 kW, q_{grid} =1 kVar). Source: **[C2].**

4.4. Summary

This chapter has studied the inner control loop design of PEPS. At first, a simple and powerful adaptive current control method was presented. The idea is to continuously update the controller gain to keep the system performance at the desired ones during different parameter variations. The control method was investigated, implemented experimentally, and compared with the conventional PR control method. In addition to its advantages, applying this method to a more complex system with more uncertain parameters is difficult. Moreover, considering the impact of control delay is not straightforward, as it may considerably impact the system stability due to the high bandwidths of the VSC's inner control loop. In this regard, a second robust current control method with fixed control gains was proposed when considering variable parameters (e.g., grid inductance) during the design procedure by modeling it as polytopic-type uncertainties. Furthermore, the system modeling takes into account a complete expression of time delay, avoiding any approximations. The design approach introduced employs the H_∞ technique and Linear Matrix Inequalities (LMIs) based on the Lyapunov-Krasovskii function. These novel LMI formulations enable computer-aided implementation and control system design, even in scenarios involving numerous control gains that need tuning and the presence of uncertain parameters.

Related Publications:

[C1] **H. Gholami-Khesht**, M. Monfared, M. Graungaard Taul, P. Davari, and F. Blaabjerg, "Direct adaptive current control of grid-connected voltage source converters based on the Lyapunov theorem," *2020 IEEE 9th Int. Power Electron. Motion Control Conf. IPEMC 2020 ECCE Asia*, pp. 858–863, 2020, doi: 10.1109/IPEMC-ECCEAsia48364.2020.9368224.

Main contributions in the paper:

As the performance of the VSC current controller may be affected by power system uncertainties, this work proposes a direct adaptive current controller to cope with power system parameter changes. In such a way, it continuously updates the control gains based on proper adaption laws, providing the desired closed-loop response under all variable conditions.

[C2] **H. Gholami-Khesht**, P. Davari, M. Novak, and F. Blaabjerg, "Robust H_∞ current control of three-phase grid-connected voltage source converters using linear matrix inequalities," in *2021 IEEE 22nd Workshop on Control and Modelling of Power Electronics (COMPEL)*, Nov. 2021, pp. 1–6. doi: 10.1109/COMPEL52922.2021.9646071.

Main contributions in the paper:

This paper proposes a robust H_∞ current controller based on the LMI formulation and a polytopic representation of uncertainties. In the proposed model, a full expression of the control delay is considered and not just an approximation. Moreover, the grid impedance is considered uncertain. The proposed design strategy calculates a constant control gain that provides the desired requirement under the worst-case scenario. Therefore, a better response can be expected for the other conditions. Moreover, since the proposed control method uses a fixed structure with constant control gains, it does not have implementation difficulties like the adaptive control methods. Finally, this research work examined the response of the H_∞ techniques under very low SCRs, which have not been studied so far.

Chapter 5. A Systematic and Optimal Control Design Method for Inner and Outer Control Loops in PEPS

5.1. Background

The previous chapter proposed adaptive and robust tuning of the inner current control loop of grid-connected VSCs and neglected the design and study the impact of outer voltage control loops. The main reason is that when considering all control loops simultaneously, multiplications of different control gains appear, leading to a nonlinear optimization problem. Therefore the overall control system design can become a recursive and laborious task. Moreover, neglecting the interaction between control loops may lead to a conservative design approach.

This problem can become more severe under weak grid conditions where the coupling between VSC and the power grid increases due to the synchronization mechanism and it may lead to a smaller stability margin as investigated in Chapter 3. Reducing the PLL bandwidth is a typical solution to maintain the required stability margin; however, it is not recommendable from transient response perspective.

Therefore this chapter aims to respond to these challenges in such a way that a conventional cascaded control loop is considered and augmented by including additional state-feedback-based active damping for inner and outer control loops (to damp high- and low-frequency oscillations). Then a new formulation is proposed that can lump all control gains into one control gain matrix. It leads to a linear optimization problem, simplifying the control system design and optimal control gains calculation. The new formulation allows using well-known control system design methods already developed for linear systems. Among them, the linear-quadratic regulator (LQR) design framework is attractive due to its effectiveness and practicality. As a result of the suggested control structure and optimal control gains computation, the control method shows good robustness against the system uncertainties and employs, at the same time, a high-performance PLL under weak grid conditions.

5.2. Derivation of Proposed Control Method

The conventional control system of a grid-connected VSC is shown in Fig. 5.1 (for access simplicity). The control system employs different controllers with at least eleven control parameters. These control gains (significantly) impact the system's performance and stability and should be carefully designed. Moreover, there are many system states available that can be appropriately employed. It can be expected that by properly utilizing them it can improve the system response, as shown in Fig. 5.2. However, it increases the number of tuning parameters leading to a higher design complexity.

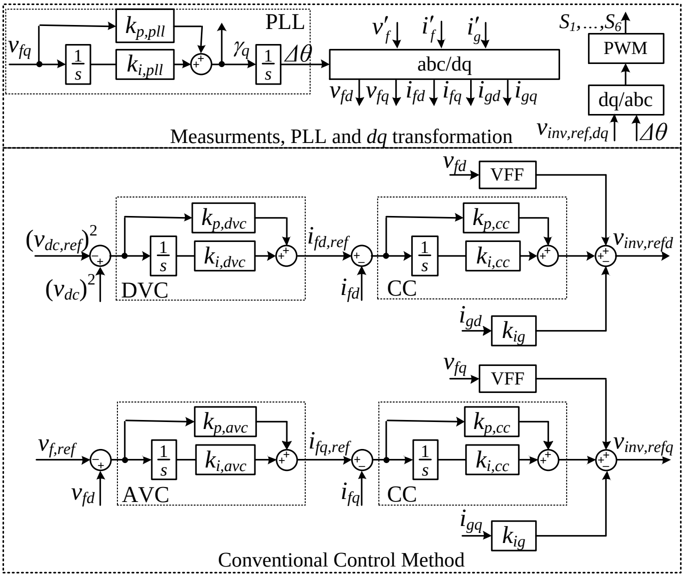

Fig. 5.1: Block diagram of the conventional control method of VSC using PI-controllers. CC: current controller, VFF: voltage feedforward controller, AVC: AC voltage magnitude controller, DVC: dc-link voltage controller, PLL: phase-locked loop. Source: **[J2].**

The control system in Fig. 5.2 can be further simplified as follows. As it can be seen, some control gains are multiplied at the same states, entered at the same point in the control structure, and provide the exact damping; therefore, the repeated control gains can be omitted to reduce the number of tuning parameters.

For example, one of the $k_{p,dvc}$ and K_{f1} (1,15) (the element at the first row and the fifteenth column of the matrix) can be eliminated since they are multiplied by Δv_{dc} at the same place in the control system. The same conclusion can be drawn for other control gains. Therefore Fig. 5.2 can be simplified as Fig. 5.3. As shown in Fig. 5.3, control gains that produce the exact damping are eliminated (e.g., $k_{p,dvc,}$ etc.). All control gains regarding the internal current control, external voltage control, and active damping control are lumped into one control gain matrix, providing a linear optimization problem and simplifying the control system design. In addition, utilizing all system states is provided, which may lead to a higher stability margin and better system response by a proper tuning.

There is still the question of how to calculate the control gain matrix and based on which design technique and criteria. To answer this question, the following subsections will present a system state-space model representation and then an optimal design process to calculate the control gain matrix.

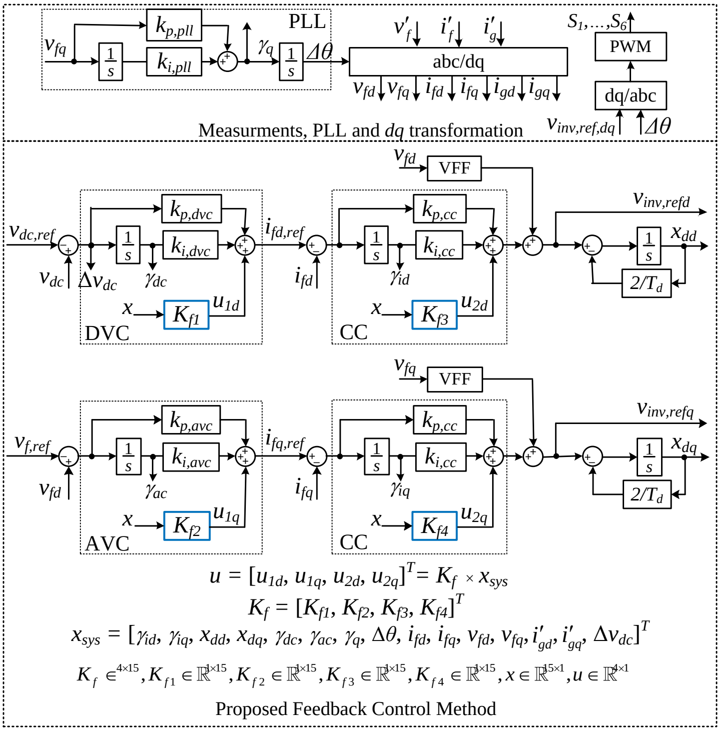

Fig. 5.2: The proposed control solution including state-feedback-based active damping in all control loops. Source: **[J2].**

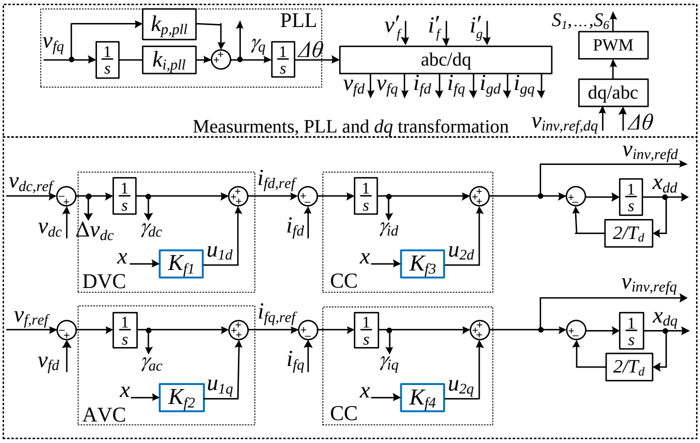

Fig. 5.3: Structure of the proposed robust and optimal control method of a grid-connected VSC. Source: **[J2].**

5.3. Modeling of a Grid-Connected VSC for Optimal Control System Design

The nonlinear state-space model of the overall system can be written as follows, considering the power and control system dynamics in Chapter 2, in Fig. 5.1 and Fig. 5.3 [J3]:

$$
\begin{array}{ll}
 & v_{invd} = \left(4/T_d\right)x_{dd} - v_{inv,refd} \\
\dot{\gamma}_q = v_{fq} & v_{invq} = \left(4/T_d\right)x_{dq} - v_{inv,refq} \\
\Delta\dot{\theta} = k_{pp}v_{fq} + k_{ip}\gamma_q & \dot{i}_{fd} = L_f^{-1}\left(L_f\omega_1 i_{fq} + v_{invd} - v_{fd}\right) \\
\dot{\gamma}_{dc} = v_{dc,ref} - v_{dc} & \dot{i}_{fq} = L_f^{-1}\left(-L_f\omega_1 i_{fd} + v_{invq} - v_{fq}\right) \\
\dot{\gamma}_{ac} = v_{f,ref} - v_{fd} & \dot{v}_{fd} = C_f^{-1}\left(C_f\omega_1 v_{fq} + i_{fd} - \cos\left(\delta\right)i'_{gd} - \sin\left(\delta\right)i'_{gq}\right) \\
\dot{\gamma}_{id} = -\gamma_{dc} - i_{fd} + u_{1d} & \dot{v}_{fq} = C_f^{-1}\left(-C_f\omega_1 v_{fd} + i_{fq} + \sin\left(\delta\right)i'_{gd} - \cos\left(\delta\right)i'_{gq}\right) \\
\dot{\gamma}_{iq} = -\gamma_g - i_{fq} + u_{1q} & \dot{i}'_{gd} = L_g^{-1}\left(L_g\omega_1 i'_g + \cos\left(\delta\right)v_{fd} - \sin\left(\delta\right)v_{fq} - v'_{gd}\right) \\
v_{inv,refd} = \gamma_{id} + u_{2d} & \dot{i}'_{gq} = L_g^{-1}\left(-L_g\omega_1 i'_g + \sin\left(\delta\right)v_{fd} + \cos\left(\delta\right)v_{fq} - v'_{gq}\right) \\
v_{inv,refq} = \gamma_{iq} + u_{2q} & \dot{v}_{dc} = \dfrac{-1}{C_{dc}}\dfrac{v_{fd}.i_{fd} + v_{fq}.i_{fq}}{v_{dc}} + \dfrac{1}{C_{dc}}i_{dc} \\
\dot{x}_{dd} = \left(-2/T_d\right)x_{dd} + v_{inv,refd} & \\
\dot{x}_{dq} = \left(-2/T_d\right)x_{dq} + v_{inv,refq} &
\end{array}
\tag{5.1}
$$

here γ_{id}, γ_{iq}, γ_q, γ_{ac}, and γ_{dc} are integral states for the CC, PLL, AVC, and DVC. Note that the Pade approximation represents the digital implementation delay. Also, the system equations are represented in two synchronous *dq*-frames, i.e., global and local *dq*-frames, in oder to include the PLL impact. The global *dq*-frame follows the infinite bus voltage, and the local and converter *dq*-frame follows the PoC bus voltage. The global and local frame variables are represented with and without the superscript “ ′ ”, respectively.

The above nonlinear model can be compactly expressed as follows:

$$
\begin{aligned}
x_{sys} &= \left[\gamma_{id}\ \ \gamma_{iq}\ \ x_{dd}\ \ x_{dq}\ \ \gamma_{dc}\ \ \gamma_{ac}\ \ \gamma_q\ \ \Delta\theta\ \ i_{fd}\ \ i_{fq}\ \ v_{fd}\ \ v_{fq}\ \ i'_{gd}\ \ i'_{gq}\ \ \Delta v_{dc}\right]^T \\
u &= \left[u_{1d}\ \ u_{1q}\ \ u_{2d}\ \ u_{2q}\right]^T,\ d = \left[v_{dc,ref}\ \ v_{f,ref}\ \ v'_g\ \ i_{dc}\right]^T
\end{aligned}
\tag{5.2}
$$

Where x_{sys} is the system state vector, and u and d are control and disturbance inputs.

A linearized state-space model around equilibrium and in steady-state point (x_e, u_e, d_e) facilitates calculating the control gain matrix based on well-known design strategies developed for linear time-invariant systems. The following can calculate the linearized model:

$$\begin{aligned}
\dot{x}_{sys} &= Ax_{sys} + Bu + Dd \\
A &= \frac{\partial f}{\partial x} \mid x_{sys} = x_e, u = u_e, d = d_e \\
B &= \frac{\partial f}{\partial u} \mid x_{sys} = x_e, u = u_e, d = d_e \\
D &= \frac{\partial f}{\partial d} \mid x_{sys} = x_e, u = u_e, d = d_e
\end{aligned} \tag{5.3}$$

here, A, B, and D are the state matrix, control input matrix, and disturbance input matrix, respectively.

5.4. Calculating the Control Gain Matrix

The previous discussions have provided a new formulation that lumped all control gains into a single matrix and led to a linear optimization problem. Therefore different design techniques can be employed. This research selects a linear-quadratic regulator (LQR) to achieve a systematic approach using multivariable control of grid-connected VSCs, which is then optimized.

The static full-state-feedback control law for a given dynamic in (5.3) is [70], [91]:

$$u = -K_f x_{sys} \tag{5.4}$$

The main aim is to find the optimal gain matrix K_f that minimizes the following quadratic performance cost function:

$$J(u) = \int_0^\infty \left(x_{sys}{}^T Q x_{sys} + u^T R u \right) dt, \quad Q = Q^T \geq 0, R = R^T \geq 0 \tag{5.5}$$

where Q and R are constant matrixes that represent performance and control input weighting matrixes.

The optimal gain matrix to minimize the above cost function is given by:

$$K_f = R^{-1} B^T P \tag{5.6}$$

here the positive definite matrix P is a solution using the following algebraic Riccati equation:

$$A^T P + PA - PBR^{-1} B^T P + Q = 0 \tag{5.7}$$

This solution guarantees a stable closed-loop system $\left(A_{cl} = A - BK_f \right)$ and keeps the infinite-horizon quadratic cost function (J) to a minimum value. The optimal solution is available if and only if the sets of (A, B) and $\left(\sqrt{Q}, A \right)$ are stabilizable and detectable, respectively. It is worth mentioning that there are many powerful tools to quickly solve the above problem, even for a MIMO and high-dimensional system [70], [91].

5.4.1. Weighting matrixes selection

As deduced in the previous subsection, the control gains calculation depends on the selection of weighting matrixes (Q and R). Proper selection of matrixes highly impacts the system response and stability. On the other hand, these two matrixes for the system under study include 130 elements to design, which is considerably high. Therefore, the following questions arise: (1) How can the number of tuning parameters be reduced? (2) How can they be associated with the typical stability and performance indices such as maximum damping factor (σ_{max}) and minimum damping ratio (ξ_{min})?

The standard solution to reduce the number of weighting factors is to select diagonal matrixes. The inverse of diagonal elements (q_i^{-1} or r_i^{-1}) is associated with the maximum allowable system states or inputs ($x_i^{\wedge 2}$ or $u_i^{\wedge 2}$) values. The higher Q elements cause smaller steady-state errors and better disturbance rejection at the cost of a higher norm of the control gain matrix. Higher control gains increase the sensitivity to unmodeled dynamic and control system delay. Therefore, their selection compromises desired performance requirements and control matrix norms.

Yet, by diagonal matrix selection, nineteen weighting factors should be chosen. A computer-aided program can select the tuning factors based on an optimization approach to meet the desired stability requirements and control efforts. This design method takes a long time and does not give a clear insight into the relationships between the tuning factors and desired stability indices. Therefore, further reduction of the tuning factors and finding more explicit connections between them and system response is highly required.

There are four control inputs (u_{1d}, u_{1q}, u_{2d}, and u_{2q}); therefore, three or four individual tuning factors may be enough to fulfill the desired stability and performance metrics in terms of maximum damping factor, minimum damping ratio, and magnitude of control gain matrix.

Therefore following recommendations are made to divide the control inputs and system states into four groups:

1. The input cost matrix is chosen as $R = rI_{4\times4}$; so only one tuning factor (r) is required to be selected. This parameter limits the control gains' norm and reduces the sensitivity to noise and delay in practical implementation.
2. Integrals of tracking errors $\left(\gamma_{id}, \gamma_{iq}, \gamma_{dc}, \gamma_{ac}, \gamma_q\right)$ can be considered in one group, and thus one tuning factor is selected for them (q_1). This tuning factor affects steady-state errors.

3. Another tuning factor can be associated with dc-link voltage tracking error (Δv_{dc}), significantly affecting dc-link voltage dynamic response and, consequently, inverter current variations.

4. For the remaining states, $(x_{dd}, x_{dq}, \Delta\theta, i_{fd}, i_{fq}, v_{fd}, v_{fq}, i'_{gd}, i'_{gq})$ one tuning factor is selected. There are intermediate states, which can improve the system damping for different oscillations.

Finally, based on the above categorization, the following cost matrixes are chosen:

$$\begin{aligned} &R = diag(r,r,r,r) \\ &Q = diag(q_1,q_1,q_2,q_2,q_1,q_1,q_1,q_2,q_2,q_2,q_2,q_2,q_2,q_3) \end{aligned} \tag{5.8}$$

In (5.8), the weighting matrixes include four tuning factors to be selected (q_1, q_2, q_3, and r). Table 5.1 summarizes their impact on the system stability and performance, as explained in the following.

Table 5.1: Impacts of tuning parameters (q_1, q_2, q_3, and r) on the system's stability and performance in terms of the control gain matrix, maximum damping factor, and minimum damping ratio. norm(K_f) returns the 2-norm or maximum singular value of the control gain matrix, Source: **[J2]**

q_1	norm(K_f)	σ_{max}	ξ_{min}
1e^1	9.7e^3	-1.5	0.28
1e^2	9.8e^3	-4.5	0.28
1e^3	9.8e^3	-14.1	0.28
1e^4	9.9e^3	-41.6	0.28
2e^4	9.9e^3	-41.2	0.28
1e^5	10.2e^3	-41	0.28
1e^6	11.3e^3	-41	0.28

q_2	norm(K_f)	σ_{max}	ξ_{min}
1e^{-2}	1.6e^3	-42	0.03
1e^{-1}	3.5e^3	-41.9	0.1
5e^{-1}	7.1e^3	-41.8	0.21
1	9.8e^3	-41.6	0.28
2	13.8e^3	-41.1	0.36
5	21.5e^3	-34	0.39
10	29.8e^3	-26	0.42

q_3	norm(K_f)	σ_{max}	ξ_{min}
1e^{-2}	9.7e^3	-40	0.26
1e^{-1}	9.7e^3	-40	0.27
1	9.7e^3	-40	0.28
2	9.8e^3	-40	0.28
5	9.9e^3	-42	0.28
10	10e^3	-31	0.28
100	10.7e^3	-10	0.28

r	norm(K_f)	σ_{max}	ξ_{min}
1e^{-2}	99.3e^3	-42	0.48
1e^{-1}	36.5e^3	-42	0.47
1	12.1e^3	-42	0.32
2	8.5e^3	-41	0.25
5	5.3e^3	-31	0.17
10	3.8e^3	-23	0.12
100	1.3e^3	-7	0.03

Selection of q_1

As Table 5.1 shows, q_1 considerably affects the maximum damping factor (σ_{max}). For a higher value of q_1, the system stability margin is superior at the higher control gain norm price. This parameter does not have a considerable impact on the minimum damping ratio (ξ_{min}).

Selection of q_2

Unlike the previous tuning factor, q_2 substantially impacts the minimum damping ratio (ξ_{min}) and not the damping factor (σ_{max}). Again, a compromise between better system transient response and overshoot (in terms of damping ratio) and the norm of the control gain matrix exist.

Selection of q_3

This parameter significantly impacts the dynamic response of dc-link voltage and, as a consequence, the inverter current response. The inverter *d*-axis current can be considered as a control input for dc-link voltage; thus, higher variations in the inverter currents are expected where a faster response in the dc-link voltage is required. Fig. 5.4 demonstrates the impact of different q_3 values on the dc-link voltage and inverter current responses. The dc-link voltage shows a faster response with a smaller overshoot for a higher value of q_3 at the cost of higher inverter current variations and vice versa.

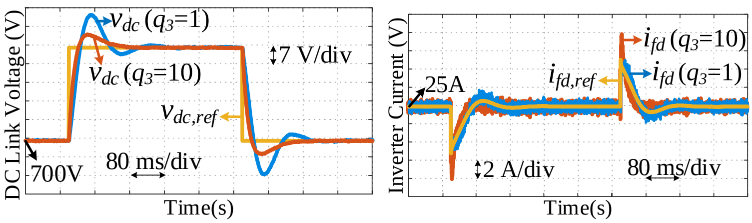

Fig. 5.4: Simulation results showing the impact of tuning parameter q_3 on the d-axis inverter current and dc-link voltage responses (q_1=1e^4, q_2=1, r=1.5), (q_3=1, norm(K)=9.7e3, σ_{max}=-39, and ξ_{min}=0.28) in blue, and (q_3=10, norm(K)=9.9e3, σ_{max}=-31, and ξ_{min}=0.28) in orange. Source: **[J2].**

Selection of r

The norm of the control gain matrix is affected by this parameter, and lower values of *r* mean higher control gains are permitted. Even though the stability margin is superior in this situation, high control gain leads to difficulties in practical implementation. Therefore there is a compromise between the system response and the norm of the control gain matrix.

5.4.2. An overview of the weighting factors design process

As studied so far, almost a direct relationship between tuning parameters (r, q_1, q_2, q_3) and stability and performance requirements (σ_{max}, ξ_{min}, norm(K_f)) are identified, simplifying the control system design and providing a clearer picture of the designed system.

Hence, the following steps summarize the design procedure:

Step 1: Small values for q_1, q_2, q_3, and r are chosen.

Step 2: By increasing q_1, the maximum damping factor (σ_{max}) is improved.

Step 3: By increasing q_2, the minimum damping ratio (ξ_{min}) is adjusted.

Step 4: By increasing r, the control gain matrix norm (norm(K_f)) is limited.

Step 5: By tuning q_3, a compromise between dc-link voltage and inverter current transient response and overshoot is obtained.

5.5. Robustness Analysis

Unlike the H_∞ techniques, the previous design procedure in section 5.4 does not consider uncertainties in the design step. Therefore, it is necessary to consider the impact of different uncertainties on the control system's robustness. In this respect, this subsection investigates the effect of operating point changes, grid SCR variations, and PLL bandwidths using eigenvalue analysis. Moreover, a comparison with the conventional control method is also given as shown in Fig. 5.1. The closed-loop eigenvalues of the proposed control method are computed using the system state-space model in (5.3) and the given control gain matrix in (5.6) $\left(A_{cl} = A - BK_f\right)$. The control gain matrix (K_f) is calculated for the P= P_n, SCR=5.5, and f_{PLL}=10 Hz once, and it is kept fixed during the robustness analysis. The eigenvalues and critical mode of the conventional control method are also calculated using the presented linearized model in Chapter 2.

5.5.1. Impact of grid SCR variations

Fig. 5.5 plots the critical mode locations where the SCR varies from 10 (strong grid) to 1 (ultra-weak grid) conditions for both conventional and proposed control methods. It covers a larger area in a complex plane under the conventional one, meaning higher sensitivities to variations in the grid SCR. Moreover, the system becomes unstable under a weaker grid condition, SCR=1.37, even though a low PLL bandwidth is used (f_{PLL}=10 Hz). On the contrary, the proposed control method shows a lower sensitivity to grid SCR variations. The critical mode is less than -30 1/sec under all grid conditions, guaranteeing a good stability margin. Additionally, the possibility of employing a PLL with higher bandwidth is also provided (f_{PLL}=50 Hz), facilitating a fast transient response and better disturbance rejection.

5.5.2. Impact of operating point changes

Fig. 5.6 demonstrates the critical mode locations under both control methods when the inverter power level changes from 0.01P_n to the P_n under a weak grid condition (SCR=1.5). As it can be seen, both control methods stay in the stable area under operational point changes. The stability margin is reduced under the conventional control method when the inverter power level increases due to higher interaction with the power grid. An opposite behavior is observed for the proposed control method, and the stability margin improves when the power level rises to the nominal one. This is due to the fact that the control gain matrix that guarantees optimal performance is determined for the nominal power. Therefore it is rational to suppose that moving away from the full power capacity leads to slight performance deterioration.

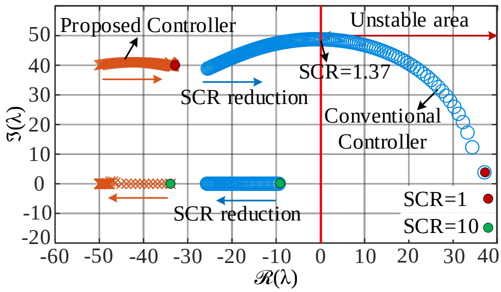

Fig. 5.5: System critical mode location in the complex plane under different grid SCRs, p_{vsc} = 10 kW, f_{PLL}=10 Hz (conventional controller), and 50 Hz (proposed controller). Source: **[J2].**

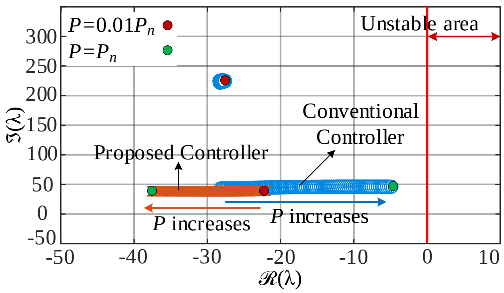

Fig. 5.6: System critical mode location in the complex plane for different inverter operating power levels, SCR=1.5, f_{PLL}=10 Hz (conventional controller), and 50 Hz (proposed controller). Source: **[J2].**

5.5.3. Impact of different PLL bandwidths

Fig. 5.7 investigates the possibility of employing a PLL with higher bandwidths on the control system and under weak grid conditions. In this regard, it shows the critical mode locations under different PLL bandwidths where the grid SCR is 1.5. When using the conventional control method, the modes cover a larger area, which means the control system is more sensitive to the synchronizing blocks and having serious control loop interactions. Moreover, the closed-loop system becomes unstable for a PLL bandwidth greater than 17 Hz. On the other hand, the proposed control method reduces the impact of the synchronization mechanism on the system's stability and performance. Thereby, the opportunity of implementing a high-performance PLL, here at 80 Hz, under a weak grid condition (SCR=1.5) is obtained.

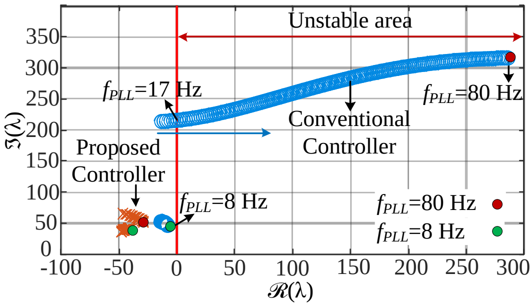

Fig. 5.7: System critical mode location in the complex plane for different PLL bandwidths (p_{vsc} = 10 kW, SCR=1.5). Source: **[J2].**

5.6. Control Gain Matrix Simplification

The proposed control structure and gain calculation can provide satisfactory robustness features. However, it needs all system states, such as grid-side current, leading to higher computations and increasing the number of sensors. Therefore finding a solution to reduce the number of sensors and calculations is highly beneficial. As presented in Chapter 4, an initial answer to reduce the number of sensors is to employ state-space model-based observers like the Kalman filter or Luenberger observer. However, additional tuning gains should be selected carefully, leading to more complexity and computations in the total system control. In this section, a more straightforward solution is proposed and tested. It reduces the number of employed system states and calculations, which is an advantage.

It is evident that properly employing all system states improves the system's stability and performance, but all states do not have the same impact on the system's overall stability. Thus it would be beneficial to find the states with significant impact and keep them in the control system; on the other hand, to remove the less influential ones in order to reduce computations. Fig. 5.8 shows the impact of eliminating different states on the system's critical mode. The number beside each mode shows the eliminated state.

For instance, the system maintains stability when excluding states 3, 4, 7, 11, 12, 13, or 14, as shown. Conversely, omitting states 1, 2, 5, 6, 8, 9, 10, or 15 repositions the critical mode to an undesirable region, resulting in system instability. The configuration marked as 00 represents the critical mode location when all states are utilized. Additionally, it's noteworthy that deactivating a single state results in the corresponding elements in the control gain matrix being set to zero. Simulations in Fig. 5.9 are prepared to verify the previous analyzes. As shown, eliminating the thirteen state (the grid side current $\left(x_{sys,13}:\text{off}\rightarrow K_f\left(:,13\right)=0\right)$) does not lead to system instability, while eliminating the ninth one $\left(x_{sys,9}:\text{off}\rightarrow K_f\left(:,9\right)=0\right)$ does.

Another interesting study is to eliminate all states that do not lead to system instability. As a result of this action, there are 8 employed states instead of 15, and 46% of all control gain matrix arrays turn into zeros.

$$x_{sys,3}, x_{sys,4}, x_{sys,7}, x_{sys,11}, x_{sys,12}, x_{sys,13} \,\&\, x_{sys,14}:\text{off}\rightarrow K_f\left(:,3:4\right)=K_f\left(:,7\right)=K_f\left(:,11:14\right)=0$$

The critical mode location under grid SCR variations for the proposed full and reduced state feedback control and the conventional one are plotted in Fig. 5.10.

As shown, reducing the number of the system's states causes a little stability degradation; however, it still indicates remarkably better robustness over the conventional one.

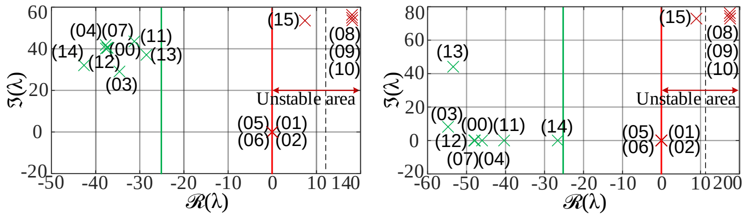

Fig. 5.8: System critical mode locations in the complex plane when one of the states is removed, and a reduced state feedback is employed. The number beside a critical mode shows the omitted state. (a) SCR=1.5 and (b) SCR=5. Source: **[J2].**

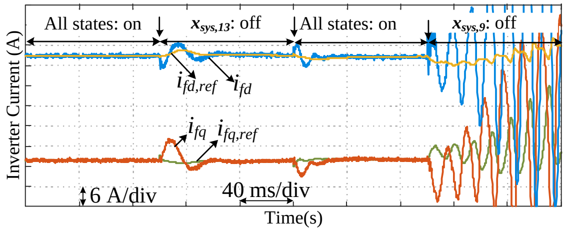

Fig. 5.9: Simulated inverter current waveforms under different control gain matrixes (full control matrix is considered (K_f), its thirteen column is set equal to zero. $\left(x_{sys,13}:\text{off}\rightarrow K_f\left(:,13\right)=0\right)$ and its ninth column is set equal to zero $\left(x_{sys,9}:\text{off}\rightarrow K_f\left(:,9\right)=0\right)$), (p_{vsc} =10 kW, f_{PLL}=50 Hz, SCR =1.5). Source: **[J2].**

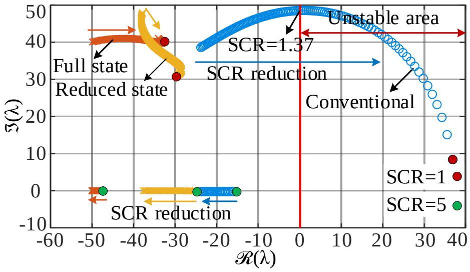

Fig. 5.10: System critical mode locations in the complex plane under different grid SCRs (p_{vsc} =10 kW and f_{PLL}=10 Hz (Conventional controller) and f_{PLL}=50 Hz (proposed controllers)). Source: **[J2].**

5.1. Simulation and Experimental Demonstration

This section presents simulation and experimental tests to study the analytical results and effectiveness of the proposed control method in practice.

In Fig. 5.11, the grid SCR changes from 1.5 to 1.37 and then reduces to 1.25. The proposed control method is not affected by these variations, while the conventional one becomes unstable under the weakest condition.

Fig. 5.12 investigates the power converter performance under different PLL bandwidths and a grid SCR equal to 1.5. The conventional one becomes unusable by increasing the PLL bandwidth from 10 to 18 Hz. In contrast, the proposed method can employ a PLL bandwidth of 50 Hz, providing better transient response and disturbance rejection.

In Fig. 5.13, 20% voltage sag happens under a low grid SCR (SCR = 2). The proposed control method shows a fast and smooth response without oscillations, thanks to the higher PLL bandwidth and the optimal gain calculations. In contrast, the conventional one shows a slower response and a larger rise time. It is worth mentioning that the conventional one still fulfills the standards' guidelines, which recommend a rise time equal to or less than 100 ms [62], [79]. However, the proposed control method represents a response much better than the required levels.

Finally, the steady-state and transient performance of both control methods under weak grid conditions (SCR=1.21) and different PLL bandwidths are examined in practice and the results are shown in Fig. 5.14 and Fig. 5.15. The conventional one is unstable under a relatively low PLL bandwidth (14 Hz), whereas the proposed control method shows higher robustness and stable operation where a fast PLL is employed (50 Hz). Moreover, the proposed control method is robust against 20% grid voltage sag, while the conventional one eventually will be unstable.

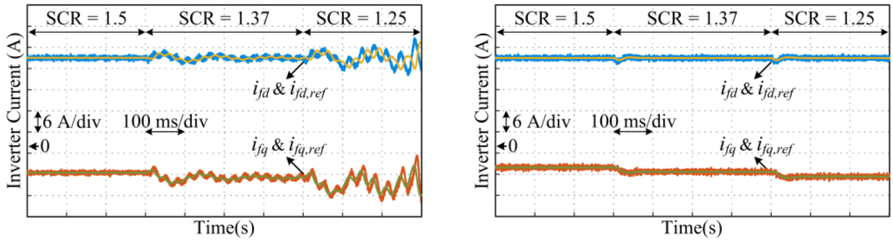

(a) (b)

Fig. 5.11: Simulated d-axis and q-axis current waveforms of VSC under different grid SCRs (SCR=1.5, 1.35 and 1.25, p_{vsc} =10 kW), (a) the conventional control method, and (b) the proposed control method. Source: **[J2].**

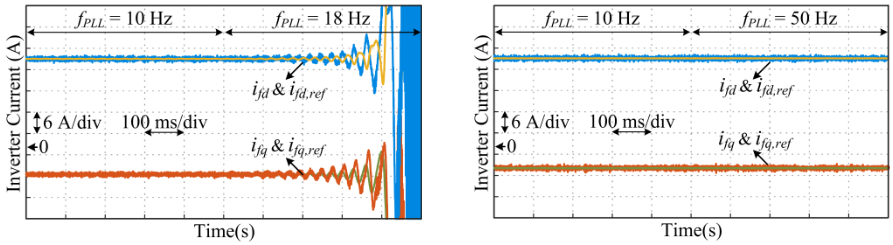

(a) (b)

Fig. 5.12: Simulated d-axis and q-axis current waveforms of VSC under different PLL bandwidths (p_{vsc} =10 kW, SCR=1.5), (a) the conventional control method, and (b) the proposed control method. Source: **[J2].**

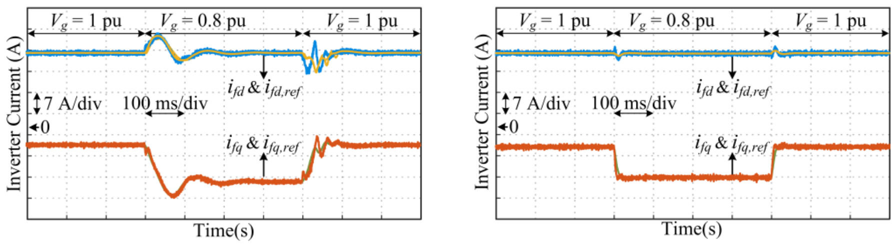

(a) (b)

Fig. 5.13: Simulated d-axis and q-axis current waveforms of VSC when 20% grid voltage sag is applied (p_{vsc} =10 kW, SCR=2), (a) the conventional control method, and (b) the proposed control method. Source: **[J2].**

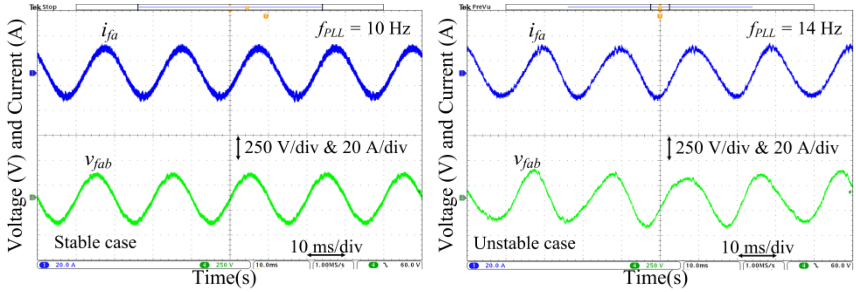

(a)

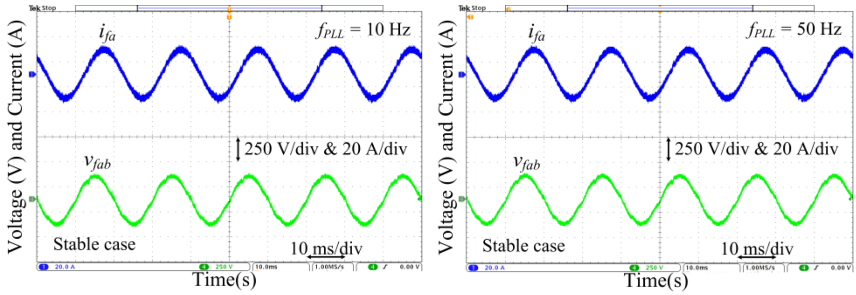

(b)

Fig. 5.14: Experimental waveforms under different PLL bandwidths (SCR=1.21, L_g =15.5 mH, and p_{vsc} =5 kW), (a) the conventional control method, and (b) the proposed control method. Source: **[J2].**

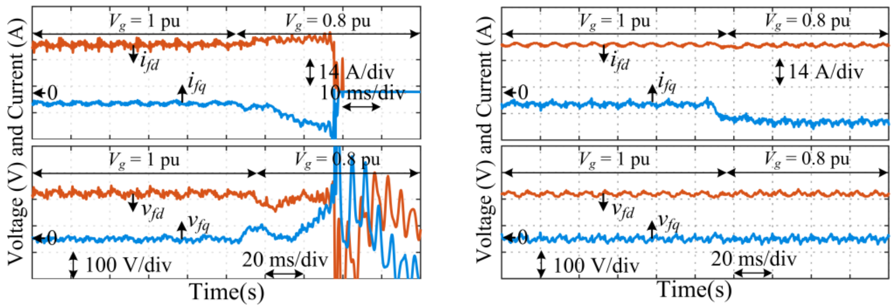

(a) (b)

Fig. 5.15: Experimental waveforms when 20% grid voltage sag is applied (SCR=1.21, L_g=15.5 mH and p_{vsc} =5 kW), (a) the conventional control method (f_{PLL}=10 Hz), and (b) the proposed control method (f_{PLL}=50 Hz). Source: **[J2].**

5.1. Summary

This Chapter proposes a new grid-connected VSC formulation, where all inner and outer control loops are considered simultaneously. It consolidates all control gains into a single matrix, resulting in a linear optimization problem and an optimal control system design. Unlike the conventional design strategies, the proposed one is less time-consuming and more straightforward. With the proposed control structure and optimal gain calculation, the control system demonstrates a strong stability margin and performance under different power system conditions. Moreover, the feasibility of employing a fast PLL is obtained, providing better fault ride-through and transient responses.

Related Publications:

[J2] **H. Gholami-Khesht**, P. Davari, C. Wu, and F. Blaabjerg, "A systematic control design method with active damping control in voltage source converters," *Appl. Sci.*, vol. 12, no. 17, p. 8893, Sep. 2022, doi: 10.3390/app12178893.

Main contributions in the paper:

This paper makes several significant contributions, including a direct and systematic design approach for the simultaneous calculation of all control gains with minimal repetition. It establishes transparent relationships between tuning parameters, system stability, and performance indices. Additionally, the proposed approach enhances the system's resilience to variations in grid impedance and operating points. It further improves the fault ride-through response and disturbance rejection capability by implementing a fast PLL.

Chapter 6. Conclusions

This chapter summarizes the main findings and research outcomes from this Ph.D. project and highlights the main contributions. In the end, the chapter concludes with some future research perspectives.

6.1. Summary

This Ph.D. project aims to stability robustness analysis and robust control system design of modern power systems with power converters integration, which is also called power electronics-based power systems (PEPS). In spite of the flexibility and controllability offered by PEPS, their lower inertia and broad dynamics make them more susceptible to parameter variations. In this regard, it is important to study stability robustness analysis and robust control system design of PEPS in order to understand their dynamic behavior and improve it, which is the main purpose of this Ph.D. thesis. The following is a summary of each chapter in the thesis:

Chapter 1 identified several research gaps concerning the robustness stability analysis and robust control system design of PEPS. These gaps were substantiated by the state-of-the-art review and served as motivation for this Ph.D. project. They also led to the formulation of research questions that the subsequent chapters aim to tackle.

Chapter 2 focused on the power electronics-based power systems description and modeling. It tried to present an overview of how the linearized state space model can be obtained and how different control loops are conventionally designed. The outcomes provided a base for future studies. In addition, it allowed comparing the proposed solutions to the most commonly used approaches.

Chapter 3 proposed a new framework for (stability) robustness analysis of a single grid-connected VSC. The aim was to contribute to the expansion of PEPS stability analysis and provide a more probabilistic perspective on the problem. This chapter discussed different aspects of probabilistic stability analysis and suggested some implementation guidelines. According to the proposed framework, operating point variations, grid impedance uncertainties, and control loop interactions are all analyzed in depth, and the main reasons for each instability phenomenon are discussed. For instance, the analysis showed how weak grid conditions (lower SCRs) reduce the fast disturbance rejection capability of high-performance PLL, limit small-signal stability margin, and widen PDF and CDF of stability and performance measures (which means higher sensitivities to uncertainties).

The remedial actions to address the identified potential stability issues are proposed in the next chapters.

Chapter 4 proposed solutions for adaptive and robust design strategies for the inner control loop of PEPS to reduce the impact of grid and filter impedances on the system stability and closed-loop responses. At first, a new adaptive current control method was presented. The main aim was to keep the system's closed-loop performance at the desired level by continuously updating the control gains when the output filter parameters are changed. In contrast to this method, a robust H_∞ control method with fixed control gains was also discussed, and it keeps the implementation simplicity as conventional control methods. The design strategy employs advanced mathematics like LMIs and Lyapunov-Krasovskii function to ensure stability and good performance over system uncertainties and disturbances. The proposed robust H_∞ control method was successfully applied under weak grid conditions that haven't been studied until now.

Despite these advantages, the proposed adaptive and robust current control methods overlook the tuning and their interaction with outer voltage control loops. This issue will be addressed and resolved in the upcoming chapter.

Chapter 5 proposed an optimal design strategy to design inner and outer control loops and active damping control gains simultaneously. Moreover, it presented clear relationships between tuning parameters, stability and performance indicators. Simulation and experimental tests demonstrate the effectiveness of the proposed method under different grid conditions. As a noteworthy advantage of this method, it will be able to provide fast PLL even when the grid conditions are weak, which is not possible with conventional control methods and design strategies (as identified and discussed in Chapter 3).

6.2. Main Contributions

The following summarizes the main research contributions of this Ph.D. project.

Power electronics-based power systems description and modeling

Polytopic-type uncertainties and a general state-space model of PEPS have been introduced (in Chapter 4). With the proposed method, incorporating uncertain parameters into the model becomes mathematically feasible when their intervals are defined. This approach also enables the inclusion of the complete expression of control system delay in state-space modeling, rather than relying on the Padé approximation. Additionally, a probabilistic representation of uncertain parameters has been discussed in Chapter 3.

A probabilistic framework for robust stability and performance analysis of a single-converter system

A new probabilistic robustness analysis framework has been introduced (Chapter 3). It was shown how uncertainties could be represented based on this method and how the results can be interpreted. It gives a probabilistic standpoint and it can reduce conservatism in the design by accounting for the probability of different operating conditions. In addition to this new framework and perspective, the proposed robustness analysis also presents some new findings on the robustness analysis of PEPS. It identifies the potential robustness issues that may come from the inverter power level changes, power grid impedance variations, and coupling between different control loops. Lastly, the proposed approach facilitates how probabilistic and robust stability analysis can be coupled doing risk and reliability assessment, one of the most important aspects of planning and designing power systems.

Adaptive and robust control methods for inner loop design of PEPS

An adaptive mechanism has been introduced to update current control gains concerning the filter impedance variations (Chapter 4). The experiments showed how the proposed adaptive control method would be helpful in a system with unknown or high variability in the filter impedances, where finding the correct value of control gains that provide the desired closed-loop performance is difficult or maybe impossible. Secondly, a robust H_∞ design technique has been proposed, where polytopic type uncertainties representing filter and grid impedance variations. This method converts all system performance and stability requirements to LMIs using the Lyapunov-Krasovskii function. It is worth noting that LMIs were calculated in a general state-space form; therefore, they can be directly used for any system represented in this form. Also, they have facilitated using a systematic robust control gains calculation based on a computer-aided program. The effectiveness of the proposed method was studied experimentally under both strong and weak grid conditions. It is worth remarking that analyzing the performance of the robust H_∞ technique under weak grid conditions had not been previously studied.

A systematic control design method with active damping control in voltage source converters

A systematic and optimal solution has been proposed to deal with broad frequency dynamics, MIMO, and cascaded control loops structure of grid-connected VSC. Based on the proposed solution, a linear optimization problem is created by lumping all control gains into one matrix, which facilitates employing powerful design techniques that have already been developed. In this thesis, an optimal control theorem has been employed to calculate the control gain matrix optimally and systematically. Moreover, clear and transparent connections between tuning parameters, stability, and performance indicators like maximum damping factor, minimum damping ratio, and the control gain matrix norm are identified, which provides good physical insight. As a noteworthy feature, the linear formulations and direct connection between tuning parameters and stability metrics significantly reduce the recursive process and make the design process far more straightforward and efficient. Finally, as a result of the proposed control structure and optimal control gain calculations, it is also possible to use a high-bandwidth PLL under weak grid conditions.

6.2.1. Findings on the research questions

The followings shortly describe how the contribution and results of this Ph.D. thesis help to address the initial research questions represented in Chapter 1.

- Can PEPS be modeled in adequate small-signal modeling of power converters to include different aspects and system conditions?

Chapter 3 proposed a new probabilistic approach to include uncertain parameters and operating point variations in the small-signal stability model and assessment.

Chapter 4 proposed a polytopic-type representation of uncertainties and a general state-space model of PEPS using LMIs.

- Which part of the system (or control parameter) exerts the most critical impact on the robustness of PEPS?

This question is discussed in detail in Chapter 3. The impact of grid SCR, operating point conditions, and interactions among different control loops are investigated on the critical mode, maximum damping factor, and minimum damping ratio based on the proposed probabilistic robustness analysis.

- How will a stability robustness analysis of PEPS be connected to the reliability metrics of such systems?

Chapter 3 showed that based on the provided PDFs and CDFs of the critical mode, it is possible to bridge small-signal stability analysis to the static risk/reliability assessments. This idea was represented and emphasized in this chapter, and some insights were discussed, however, much effort is still required to mature and develop this interesting topic, which is very beneficial for power system planners and operators.

- Is it possible to benefit from the advantages of the probabilistic stability analysis for PEPS?

Chapter 3 discussed how the probabilistic robustness analysis can be implemented and how the results can be interpreted.

- What objectives should the control system be able to handle based on the robustness analysis results?

As identified in Chapter 3 having a fast PLL under lower grid SCR is a big challenge and can not be achieved based on the conventional cascaded control system and design strategies. Therefore, a new approach in Chapter 5 was proposed to guarantee a fast PLL response and good disturbance rejection even under weak grid conditions.

- Is it possible to propose a systematic-design procedure with a minimum recursive process?

As discussed in Chapter 2 and Chapter 5, considering all inner and outer control loops leads to a nonlinear optimization problem. Solving this nonlinear optimization problem to calculate the control gains is not straightforward and leads to a time-consuming recursive process. Chapter 5 proposed a new model and linear formulation that still takes into account all inner and outer control loops and active damping gains. Consequently, well-known linear control techniques can be used to reduce recursive processes and facilitate control gains calculation.

- Does a robust and optimal control system tackle the system's uncertainties and disturbances?

The proposed adaptive and robust H_∞ control methods in Chapter 4 can tackle uncertainties regarding the inner fast control loops, such as filter parameters, grid inductance, and control delay.

The proposed robust and optimal control method in Chapter 5 can guarantee good stability margins and disturbance rejection under different operating conditions and grid SCR variations, while a fast PLL is also employed.

- Can a clear intuition be found between control tuning and relevant stability and performance indicators?

Chapter 5 proposed a new strategy to calculate all inner and outer control gains based on the new formulation and optimal control theorem. In that way, a direct and one-to-one relationship between tuning parameters (q_1, q_2, q_3, and r) and the system's stability and performance indicators (the control gain matrix, maximum damping factor, minimum damping ratio, and dc-link voltage and inverter current overshoot) have been identified (Section 5.4.2).

6.3. Research Perspectives and Future Work

Investigation of other types of PEPS stability form a probabilistic perspective

This thesis tried to present a new probabilistic perspective of small-signal stability analysis of PEPS. The same idea can be applied to other types of PEPS stability, such as synchronization stability, frequency stability, and voltage stability, to benefit from the advantages of the suggested probabilistic approaches.

Enhancing stability robustness analysis through the integration of additional indicators

To gain a more comprehensive insight into system behavior, it's advisable to incorporate supplementary stability indicators. These could include parameters like oscillation frequency, phase and gain margins, singular values, tracking errors, and disturbance rejection capabilities, among others. The development and utilization of such indicators can contribute to a more thorough assessment of the system's robustness.

Mission profile-based stability assessment

Stability analysis and control system design depend on the operating point of VSCs, which e.g., are related to wind speed and solar irradiance in the case of renewables. Therefore, historical data on wind speed and solar irradiance can generate static and dynamic load profiles to assess probabilistic stability and reliability proposed in this thesis.

Probabilistic control system design

The probabilistic robustness analysis revealed the importance of a probabilistic control system design. It can guarantee stable operation over a wide range of grid variations and maximize the probability of critical mode identification within the desired region in the complex plane.

Large-scale PEPS robustness analysis

When the penetration levels of power converters are increasing, it is required to expand the robustness framework for system-level analysis, where multiple power converters and their control systems may interact with each other and lead to an unreliable power system. This method should be able to provide solutions and guidelines that facilitate the finding of the root cause of performance degradation or instability issues for a large-scale power system. Moreover, a higher-order system with numerous uncertain parameters may lead to large computations for the analysis. Therefore, an improved stability robustness analysis method should be able to reduce the computational burden while keeping accuracy around the needed implementation.

Extending the application of the proposed robust H_∞ technique to other VSC-based power application

The proposed robust H_∞ design strategy introduces a general state-space representation and a set of LMIs to calculate the robust control gains systematically. Therefore, these LMIs can be directly used for other applications of VSCs, such as grid-forming VSCs and active power filters, where they are appropriately represented in the suggested general form.

Extending the application of the proposed systematic and optimal control design method for inner and outer control loops in PEPS

The idea can be used in other applications in which cascaded control loops exist, making the design of control systems easier and simpler. This is achieved by establishing a direct connection between tuning parameters (q_1, q_2, q_3, and r) and the system’s stability and performance in terms of the control gain matrix, maximum damping factor, and minimum damping ratio

Examining the control system without PLL for PEPS

As discussed earlier, a key cause for reduced stability margins is the need for a phase-locked loop (PLL) in current control-based methods. An alternative is direct power control (DPC), which has an inherent synchronization mechanism, eliminating the need for a PLL. DPC methods can be categorized differently, but a comprehensive study comparing their effectiveness and robustness against current control-based methods is still lacking. Additionally, the concept of grid-forming control holds relevance in this context. It’s gained attention for its natural synchronization capabilities and impressive performance, especially in weak grid scenarios.

LITERATURE LIST

[1] International renewable energy agency (IRENA), “Renewables 2022,” 2022. [Online]. Available: https://www.iea.org/reports/renewables-2022/renewable-electricity.

[2] X. Wang and F. Blaabjerg, “Harmonic stability in power electronic-based power systems: concept, modeling, and analysis,” *IEEE Trans. Smart Grid*, vol. 10, no. 3, pp. 2858–2870, 2019, doi: 10.1109/TSG.2018.2812712.

[3] M. Farrokhabadi *et al.*, “Microgrid stability definitions, analysis, and examples,” *IEEE Trans. Power Syst.*, vol. 35, no. 1, pp. 13–29, Jan. 2020, doi: 10.1109/TPWRS.2019.2925703.

[4] S. Jiang, Y. Zhu, and G. Konstantinou, “Settling angle-based stability criterion for power-electronics-dominated power systems,” *IEEE Trans. Power Electron.*, vol. 38, no. 3, pp. 2972–2984, 2023, doi: 10.1109/TPEL.2022.3218580.

[5] M. Graungaard Taul, “Synchronization stability of grid-connected converters under grid faults,” Aalborg University, 2020. Ph.D thesis.

[6] G. Wang, L. Fu, Q. Hu, C. Liu, and Y. Ma, “Transient synchronization stability of grid-forming converter during grid fault considering transient switched operation mode,” *IEEE Trans. Sustain. Energy*, vol. 14, no. 3, pp. 1504–1515, 2023, doi: 10.1109/tste.2023.3236950.

[7] B. Wen, D. Boroyevich, R. Burgos, P. Mattavelli, and Z. Shen, “Small-signal stability analysis of three-phase AC systems in the presence of constant power loads based on measured d-q frame impedances,” *IEEE Trans. Power Electron.*, vol. 30, no. 10, pp. 5952–5963, 2015, doi: 10.1109/TPEL.2014.2378731.

[8] Y. Liao and X. Wang, “Stationary-frame complex-valued frequency-domain modeling of three-phase power converters,” *IEEE J. Emerg. Sel. Top. Power Electron.*, vol. 8, no. 2, pp. 1922–1933, Dec. 2020, doi: 10.1109/JESTPE.2019.2958938.

[9] B. He, W. Chen, X. Li, L. Shu, Z. Zou, and F. Liu, “Unified frequency-domain small-signal stability analysis for interconnected converter systems,” *IEEE J. Emerg. Sel. Top. Power Electron.*, vol. 11, no. 1, pp. 532–544, 2023, doi: 10.1109/JESTPE.2022.3201570.

[10] S. Jiang, Y. Zhu, and G. Konstantinou, “Settling-angle-based stability analysis for multiple current-controlled converters,” *IEEE Trans. Power Electron.*, vol. 37, no. 11, pp. 12992–12997, 2022, doi: 10.1109/TPEL.2022.3185141.

[11] X. Wang, L. Harnefors, and F. Blaabjerg, “Unified impedance model of grid-connected voltage-source converters,” *IEEE Trans. Power Electron.*, vol. 33, no. 2, pp. 1775–1787, Feb. 2018, doi: 10.1109/TPEL.2017.2684906.

[12] H. Zhang, L. Harnefors, X. Wang, H. Gong, and J.-P. P. Hasler, “Stability analysis of grid-connected voltage-source converters using SISO modeling,” *IEEE Trans. Power Electron.*, vol. 34, no. 8, pp. 8104–8117, Aug. 2019,

doi: 10.1109/TPEL.2018.2878930.

[13] D. Lu, X. Wang, and F. Blaabjerg, "Impedance-based analysis of DC-link voltage dynamics in voltage-source converters," *IEEE Trans. Power Electron.*, vol. 34, no. 4, pp. 3973–3985, Apr. 2019, doi: 10.1109/TPEL.2018.2856745.

[14] A. Rygg, M. Molinas, C. Zhang, and X. Cai, "A modified sequence-domain impedance definition and its equivalence to the dq-domain impedance definition for the stability analysis of AC power electronic systems," *IEEE J. Emerg. Sel. Top. Power Electron.*, vol. 4, no. 4, pp. 1383–1396, 2016, doi: 10.1109/JESTPE.2016.2588733.

[15] S. F. Chou, X. Wang, and F. Blaabjerg, "Two-port network modeling and stability analysis of grid-connected current-controlled VSCs," *IEEE Trans. Power Electron.*, vol. 35, no. 4, pp. 3519–3529, Apr. 2020, doi: 10.1109/TPEL.2019.2934513.

[16] Z. Xie *et al.*, "Modeling and control parameters design for grid-connected inverter system considering the effect of PLL and grid impedance," *IEEE Access*, vol. 8, pp. 40474–40484, 2020, doi: 10.1109/ACCESS.2019.2950933.

[17] C. Zhang, X. Cai, A. Rygg, and M. Molinas, "Sequence domain SISO equivalent models of a grid-tied voltage source converter system for small-signal stability analysis," *IEEE Trans. Energy Convers.*, vol. 33, no. 2, pp. 741–749, 2018, doi: 10.1109/TEC.2017.2766217.

[18] L. Harnefors, A. G. Yepes, A. Vidal, and J. Doval-Gandoy, "Passivity-based controller design of grid-connected VSCs for prevention of electrical resonance instability," *IEEE Trans. Ind. Electron.*, vol. 62, no. 2, pp. 702–710, Feb. 2015, doi: 10.1109/TIE.2014.2336632.

[19] A. A. A. Radwan and Y. A. R. I. Mohamed, "Assessment and mitigation of interaction dynamics in hybrid AC/DC distribution generation systems," *IEEE Trans. Smart Grid*, vol. 3, no. 3, pp. 1382–1393, 2012, doi: 10.1109/TSG.2012.2201965.

[20] Y. Liao and X. Wang, "Impedance-based stability analysis for interconnected converter systems with open-loop RHP poles," *IEEE Trans. Power Electron.*, vol. 35, no. 4, pp. 4388–4397, Apr. 2020, doi: 10.1109/TPEL.2019.2939636.

[21] G. F. Gontijo, M. K. Bakhshizadeh, L. H. Kocewiak, and R. Teodorescu, "State space modeling of an Offshore wind power plant with an MMC-HVDC connection for an eigenvalue-based stability analysis," *IEEE Access*, vol. 10, no. July, pp. 82844–82869, 2022, doi: 10.1109/ACCESS.2022.3196368.

[22] Y. Wang, X. Wang, Z. Chen, and F. Blaabjerg, "Small-signal stability analysis of inverter-fed power systems using component connection method," *IEEE Trans. Smart Grid*, vol. 9, no. 5, pp. 5301–5310, 2018, doi: 10.1109/TSG.2017.2686841.

[23] D. Yang and X. Wang, "Unified modular state-space modeling of grid-

connected voltage-source converters," *IEEE Trans. Power Electron.*, vol. 35, no. 9, pp. 9700–9715, Sep. 2020, doi: 10.1109/TPEL.2020.2965941.

[24] H. Gholami-Khesht, P. Davari, and F. Blaabjerg, "An adaptive model predictive voltage control for LC-filtered voltage source inverters," *Appl. Sci.*, vol. 11, no. 2, p. 704, Jan. 2021, doi: 10.3390/app11020704.

[25] H. Yuan, X. Yuan, and J. Hu, "Modeling of grid-connected VSCs for power system small-signal stability analysis in DC-link voltage control timescale," *IEEE Trans. Power Syst.*, vol. 32, no. 5, pp. 3981–3991, Sep. 2017, doi: 10.1109/TPWRS.2017.2653939.

[26] A. Egea-Alvarez, S. Fekriasl, F. Hassan, and O. Gomis-Bellmunt, "Advanced vector control for voltage source converters connected to weak grids," *IEEE Trans. Power Syst.*, vol. 30, no. 6, pp. 3072–3081, 2015, doi: 10.1109/TPWRS.2014.2384596.

[27] R. Rosso, J. Cassoli, G. Buticchi, S. Engelken, and M. Liserre, "Robust stability analysis of LCL filter based synchronverter under different grid conditions," *IEEE Trans. Power Electron.*, vol. 34, no. 6, pp. 5842–5853, Jun. 2019, doi: 10.1109/TPEL.2018.2867040.

[28] S. Sumsurooah, M. Odavic, and S. Bozhko, "µ Approach to robust stability domains in the space of parametric uncertainties for a power System with ideal CPL," *IEEE Trans. Power Electron.*, vol. 33, no. 1, pp. 833–844, 2018, doi: 10.1109/TPEL.2017.2668900.

[29] S. Sumsurooah, M. Odavic, and S. Bozhko, "A modeling methodology for robust stability analysis of nonlinear electrical power systems," *IEEE Trans. Ind. Appl.*, vol. 52, no. 5, pp. 4416–4425, 2016, doi: 10.1109/TIA.2016.2581151.

[30] S. Sumsurooah, M. Odavic, S. Bozhko, and D. Boroyevich, "Robust stability analysis of a DC/DC buck converter under multiple parametric uncertainties," *IEEE Trans. Power Electron.*, vol. 33, no. 6, pp. 5426–5441, Jun. 2018, doi: 10.1109/TPEL.2017.2736023.

[31] R. Rosso, S. Engelken, and M. Liserre, "Robust stability investigation of the interactions among grid-forming and grid-following converters," *IEEE J. Emerg. Sel. Top. Power Electron.*, vol. 8, no. 2, pp. 991–1003, 2020, doi: 10.1109/JESTPE.2019.2951091.

[32] M. Toulabi, S. Bahrami, and A. M. Ranjbar, "Application of Edge theorem for robust stability analysis of a power system with participating wind power plants in automatic generation control task," *IET Renew. Power Gener.*, vol. 11, no. 7, pp. 1049–1057, 2017, doi: 10.1049/iet-rpg.2016.0931.

[33] Z. Liu, M. Su, Y. Sun, W. Yuan, H. Han, and J. Feng, "Existence and stability of equilibrium of DC microgrid with constant power loads," *IEEE Trans. Power Syst.*, vol. 33, no. 6, pp. 6999–7010, 2018, doi: 10.1109/TPWRS.2018.2849974.

[34] J. Liu, W. Zhang, and G. Rizzoni, "Robust stability analysis of DC microgrids with constant power loads," *IEEE Trans. Power Syst.*, vol. 33, no. 1, pp. 851–860, 2018, doi: 10.1109/TPWRS.2017.2697765.

[35] L. A. Maccari *et al.*, "LMI-based control for grid-connected converters with LCL filters under uncertain parameters," *IEEE Trans. Power Electron.*, vol. 29, no. 7, pp. 3776–3785, Jul. 2014, doi: 10.1109/TPEL.2013.2279015.

[36] G. G. Koch, C. R. D. Osorio, H. Pinheiro, R. C. L. F. Oliveira, and V. F. Montagner, "Design procedure combining linear matrix inequalities and genetic algorithm for robust control of grid-connected converters," *IEEE Trans. Ind. Appl.*, vol. 56, no. 2, pp. 1896–1906, 2020, doi: 10.1109/TIA.2019.2959604.

[37] G. G. Koch, L. A. Maccari, R. C. L. F. Oliveira, and V. F. Montagner, "Robust H∞ state feedback controllers based on linear matrix inequalities applied to grid-connected converters," *IEEE Trans. Ind. Electron.*, vol. 66, no. 8, pp. 6021–6031, 2019, doi: 10.1109/TIE.2018.2870406.

[38] H. Gholami-Khesht, P. Davari, M. Novak, and F. Blaabjerg, "Robust H∞ current control of three-phase grid-connected voltage source converters using linear matrix inequalities," in *2021 IEEE 22nd Workshop on Control and Modelling of Power Electronics (COMPEL)*, Nov. 2021, pp. 1–6. doi: 10.1109/COMPEL52922.2021.9646071.

[39] R. Bimarta and K.-H. Kim, "A robust frequency-adaptive current control of a grid-connected inverter based on LMI-LQR under polytopic uncertainties," *IEEE Access*, vol. 8, pp. 28756–28773, 2020, doi: 10.1109/ACCESS.2020.2972028.

[40] E. Mattos, L. C. Borin, C. R. D. Osorio, G. G. Koch, R. C. L. F. Oliveira, and V. F. Montagner, "Robust optimized current controller based on a two-step procedure for grid-connected converters," *IEEE Trans. Ind. Appl.*, vol. 59, no. 1, pp. 1024–1034, 2023, doi: 10.1109/TIA.2022.3211251.

[41] R. Preece, K. Huang, and J. V. Milanović, "Probabilistic small-disturbance stability assessment of uncertain power systems using efficient estimation methods," *IEEE Trans. Power Syst.*, vol. 29, no. 5, pp. 2509–2517, 2014, doi: 10.1109/TPWRS.2014.2308577.

[42] S. Munikoti, B. Natarajan, K. Jhala, and K. Lai, "Probabilistic voltage sensitivity analysis to quantify impact of high PV penetration on unbalanced distribution system," *IEEE Trans. Power Syst.*, vol. 36, no. 4, pp. 3080–3092, Jul. 2021, doi: 10.1109/TPWRS.2021.3053461.

[43] D. De Souza De Oliveira, M. Jorge Araujo De Souza, G. C. Borges Leal, F. Andrade Leite Alves, and M. Aredes, "Probabilistic assessment of the VSC-HVDC contribution in voltage stability applied to a hybrid DC-multi-infeed scenario," *IECON Proc. (Industrial Electron. Conf.*, vol. 2020-Octob, pp. 1684–1691, 2020, doi: 10.1109/IECON43393.2020.9254694.

[44] P. Wang, Z. Zhang, Q. Huang, and W. J. Lee, "Wind farm dynamic equivalent modeling method for power system probabilistic stability assessment," *IEEE Trans. Ind. Appl.*, vol. 56, no. 3, pp. 2273–2280, 2020, doi: 10.1109/TIA.2020.2970377.

[45] P. N. Papadopoulos and J. V. Milanović, "Probabilistic framework for transient stability assessment of power systems with high penetration of

renewable generation," *IEEE Trans. Power Syst.*, vol. 32, no. 4, pp. 3078–3088, 2017, doi: 10.1109/TPWRS.2016.2630799.

[46] P. He, J. Chen, X. Wu, P. Qi, R. Shen, and W. Yin, "Probabilistic small signal stability assessment of large-scale wind power integration," *2019 IEEE PES Innov. Smart Grid Technol. Asia, ISGT 2019*, pp. 1248–1253, 2019, doi: 10.1109/ISGT-Asia.2019.8881264.

[47] R. F. Mochamad, A. Ehsan, and R. Preece, "Probabilistic multi-stability assessment in power systems with uncertain wind generation," *2020 Int. Conf. Probabilistic Methods Appl. to Power Syst. PMAPS 2020 - Proc.*, pp. 18–23, 2020, doi: 10.1109/PMAPS47429.2020.9183660.

[48] A. Khodabakhshian and R. Hemmati, "Multi-machine power system stabilizer design by using cultural algorithms," *Int. J. Electr. Power Energy Syst.*, vol. 44, no. 1, pp. 571–580, 2013, doi: 10.1016/j.ijepes.2012.07.049.

[49] R. Rosso, G. Buticchi, M. Liserre, Z. Zou, and S. Engelken, "Stability analysis of synchronization of parallel power converters," in *IECON 2017 - 43rd Annual Conference of the IEEE Industrial Electronics Society*, Oct. 2017, pp. 440–445. doi: 10.1109/IECON.2017.8216078.

[50] S. Peyghami, P. Palensky, and F. Blaabjerg, "An overview on the reliability of modern power electronic based power systems," *IEEE Open J. Power Electron.*, vol. 1, no. December 2019, pp. 34–50, 2020, doi: 10.1109/OJPEL.2020.2973926.

[51] S. Peyghami, F. Blaabjerg, and P. Palensky, "Incorporating power electronic converters reliability into modern power system reliability analysis," *IEEE J. Emerg. Sel. Top. Power Electron.*, vol. 9, no. 2, pp. 1668–1681, Apr. 2021, doi: 10.1109/JESTPE.2020.2967216.

[52] A. Sangwongwanich, Y. Yang, D. Sera, and F. Blaabjerg, "Lifetime evaluation of grid-connected PV inverters considering panel degradation rates and installation sites," *IEEE Trans. Power Electron.*, vol. 33, no. 2, pp. 1225–1236, 2018, doi: 10.1109/TPEL.2017.2678169.

[53] A. Sangwongwanich, Y. Yang, D. Sera, F. Blaabjerg, and D. Zhou, "On the impacts of PV array sizing on the inverter reliability and lifetime," *IEEE Trans. Ind. Appl.*, vol. 54, no. 4, pp. 3656–3667, Jul. 2018, doi: 10.1109/TIA.2018.2825955.

[54] H. Jedtberg, A. Pigazo, M. Liserre, and G. Buticchi, "Analysis of the robustness of transformerless PV inverter topologies to the choice of power devices," *IEEE Trans. Power Electron.*, vol. 32, no. 7, pp. 5248–5257, Jul. 2017, doi: 10.1109/TPEL.2016.2612888.

[55] H. Gong, X. Wang, and D. Yang, "DQ-frame impedance measurement of three-phase converters using time-domain MIMO parametric identification," *IEEE Trans. Power Electron.*, vol. 36, no. 2, pp. 2131–2142, 2021, doi: 10.1109/TPEL.2020.3007852.

[56] F. Hans, W. Schumacher, S.-F. Chou, and X. Wang, "Design of multifrequency proportional–resonant current controllers for voltage-source converters," *IEEE Trans. Power Electron.*, vol. 35, no. 12, pp. 13573–

13589, Dec. 2020, doi: 10.1109/TPEL.2020.2993163.

[57] M. Lu, A. Al-Durra, S. M. Muyeen, S. Leng, P. C. Loh, and F. Blaabjerg, "Benchmarking of stability and robustness against grid impedance variation for LCL-filtered grid-interfacing inverters," *IEEE Trans. Power Electron.*, vol. 33, no. 10, pp. 9033–9046, Oct. 2018, doi: 10.1109/TPEL.2017.2784685.

[58] X. Wang, F. Blaabjerg, and P. C. Loh, "Grid-current-feedback active damping for LCL resonance in grid-connected voltage-source converters," *IEEE Trans. Power Electron.*, vol. 31, no. 1, pp. 213–223, 2016, doi: 10.1109/TPEL.2015.2411851.

[59] H. Wu and X. Wang, "Virtual-flux-based passivation of current control for grid-connected VSCs," *IEEE Trans. Power Electron.*, vol. 35, no. 12, pp. 12673–12677, May 2020, doi: 10.1109/TPEL.2020.2997876.

[60] H. Gong, X. Wang, L. Harnefors, J.-P. Hasler, and C. Danielsson, "Admittance-dissipativity analysis and shaping of dual-sequence current control for VSCs," *IEEE J. Emerg. Sel. Top. Power Electron.*, vol. 10, no. 1, pp. 324–335, Feb. 2022, doi: 10.1109/JESTPE.2021.3067553.

[61] S. Zhou *et al.*, "An improved design of current controller for LCL-type grid-connected converter to reduce negative effect of PLL in weak grid," *IEEE J. Emerg. Sel. Top. Power Electron.*, vol. 6, no. 2, pp. 648–663, Jun. 2018, doi: 10.1109/JESTPE.2017.2780918.

[62] H. Zhang *et al.*, "Loop-at-a-time stability analysis for grid-connected voltage-source converters," *IEEE J. Emerg. Sel. Top. Power Electron.*, vol. 9, no. 5, pp. 5807–5821, Oct. 2021, doi: 10.1109/JESTPE.2020.3024103.

[63] X. Zhang, L. Tan, J. Xian, H. Zhang, Z. Ma, and J. Kang, "Direct grid-side current model predictive control for grid-connected inverter with LCL filter," *IET Power Electron.*, vol. 11, no. 15, pp. 2450–2460, Dec. 2018, doi: 10.1049/iet-pel.2018.5338.

[64] P. Falkowski and A. Sikorski, "Finite control set model predictive control for grid-connected AC-DC converters with LCL filter," *IEEE Trans. Ind. Electron.*, vol. 65, no. 4, pp. 2844–2852, Apr. 2018, doi: 10.1109/TIE.2017.2750627.

[65] C. S. Lim, S. S. Lee, Y. C. Cassandra Wong, I. U. Nutkani, and H. H. Goh, "Comparison of current control strategies based on FCS-MPC and D-PI-PWM control for actively damped VSCs with LCL-filters," *IEEE Access*, vol. 7, pp. 112410–112423, Aug. 2019, doi: 10.1109/access.2019.2934185.

[66] R. Guzman, L. G. De Vicuna, A. Camacho, J. Miret, and J. M. Rey, "Receding-horizon model-predictive control for a three-phase VSI with an LCL filter," *IEEE Trans. Ind. Electron.*, vol. 66, no. 9, pp. 6671–6680, Sep. 2019, doi: 10.1109/TIE.2018.2877094.

[67] O. Babayomi, Z. Zhang, Z. Li, M. L. Heldwein, and J. Rodriguez, "Robust predictive control of grid-connected converters: sensor noise suppression with parallel-cascade extended state observer," *IEEE Trans. Ind. Electron.*, vol. PP, pp. 1–13, 2023, doi: 10.1109/TIE.2023.3279565.

[68] F. M. Mahafugur Rahman, V. Pirsto, J. Kukkola, M. Routimo, and M. Hinkkanen, "State-space control for LCL filters: converter versus grid current measurement," *IEEE Trans. Ind. Appl.*, vol. 56, no. 6, pp. 6608–6618, 2020, doi: 10.1109/TIA.2020.3016915.

[69] S. A. Khajehoddin, M. Karimi-Ghartemani, and M. Ebrahimi, "Optimal and systematic design of current controller for grid-connected inverters," *IEEE J. Emerg. Sel. Top. Power Electron.*, vol. 6, no. 2, pp. 812–824, 2018, doi: 10.1109/JESTPE.2017.2737987.

[70] S. Silwal, S. Taghizadeh, M. Karimi-Ghartemani, M. J. Hossain, and M. Davari, "An enhanced control system for single-phase inverters interfaced with weak and distorted grids," *IEEE Trans. Power Electron.*, vol. 34, no. 12, pp. 12538–12551, 2019, doi: 10.1109/TPEL.2019.2909532.

[71] S. P. Ribas, L. A. Maccari, H. Pinheiro, R. C. de L. F. Oliveira, and V. F. Montagner, "Design and implementation of a discrete-time H-infinity controller for uninterruptible power supply systems," *IET Power Electron.*, vol. 7, no. 9, pp. 2233–2241, Sep. 2014, doi: 10.1049/iet-pel.2013.0794.

[72] L. Huang, H. Xin, and F. Dorfler, "H∞-control of grid-connected converters: design, objectives and decentralized stability certificates," *IEEE Trans. Smart Grid*, vol. 11, no. 5, pp. 3805–3816, Sep. 2020, doi: 10.1109/TSG.2020.2984946.

[73] H. Gholami-Khesht, M. Monfared, and S. Golestan, "Low computational burden grid voltage estimation for grid connected voltage source converter-based power applications," *IET Power Electron.*, vol. 8, no. 5, pp. 656–664, May 2015, doi: 10.1049/iet-pel.2014.0466.

[74] L. Harnefors, L. Zhang, and M. Bongiorno, "Frequency-domain passivity-based current controller design," *IET Power Electron.*, vol. 1, no. 4, pp. 455–465, 2008, doi: 10.1049/iet-pel:20070286.

[75] L. Harnefors, A. G. Yepes, A. Vidal, and J. Doval-Gandoy, "Passivity-based controller design of grid-connected VSCs for prevention of electrical resonance instability," *IEEE Trans. Ind. Electron.*, vol. 62, no. 2, pp. 702–710, Feb. 2015, doi: 10.1109/TIE.2014.2336632.

[76] A. Reznik *et al.*, "LCL filter design and performance analysis for grid-interconnected systems," vol. 50, no. 2, pp. 1225–1232, 2014.

[77] L. Harnefors, M. Bongiorno, and S. Lundberg, "Input-admittance calculation and shaping for controlled voltage-source converters," *IEEE Trans. Ind. Electron.*, vol. 54, no. 6, pp. 3323–3334, 2007, doi: 10.1109/TIE.2007.904022.

[78] A. Chaoui, F. Krim, J. P. Gaubert, and L. Rambault, "DPC controlled three-phase active filter for power quality improvement," *Int. J. Electr. Power Energy Syst.*, vol. 30, no. 8, pp. 476–485, 2008, doi: 10.1016/j.ijepes.2008.04.009.

[79] "IEEE guide for specification of transmission static synchronous compensator (STATCOM) systems," 2019.

[80] F. Hans, W. Schumacher, and L. Harnefors, "Small-signal modeling of

three-phase synchronous reference frame Phase-locked loops," *IEEE Trans. Power Electron.*, vol. 33, no. 7, pp. 5556–5560, 2018, doi: 10.1109/TPEL.2017.2783189.

[81] S. Golestan, J. M. Guerrero, and J. C. Vasquez, "Three-phase PLLs: a review of recent advances," *IEEE Trans. Power Electron.*, vol. 32, no. 3, pp. 1894–1907, Mar. 2017, doi: 10.1109/TPEL.2016.2565642.

[82] F. De Bosio, L. A. De Souza Ribeiro, F. D. Freijedo, M. Pastorelli, and J. M. Guerrero, "Effect of state feedback coupling and system delays on the transient performance of stand-alone VSI with LC output filter," *IEEE Trans. Ind. Electron.*, vol. 63, no. 8, pp. 4909–4918, 2016, doi: 10.1109/TIE.2016.2549990.

[83] Z. Xin, X. Wang, P. C. Loh, and F. Blaabjerg, "Grid-current-feedback control for LCL-filtered grid converters with enhanced stability," *IEEE Trans. Power Electron.*, vol. 32, no. 4, pp. 3216–3228, Apr. 2017, doi: 10.1109/TPEL.2016.2580543.

[84] R. E. Moore and F. Bloom, *Linear matrix inequalities in system and control theory SIAM studies in applied mathematics*. [Online]. Available: https://web.stanford.edu/~boyd/lmibook/lmibook.pdf.

[85] Y. Huang, X. Yuan, J. Hu, and P. Zhou, "Modeling of VSC connected to weak grid for stability analysis of DC-link voltage control," *IEEE J. Emerg. Sel. Top. Power Electron.*, vol. 3, no. 4, pp. 1193–1204, 2015, doi: 10.1109/JESTPE.2015.2423494.

[86] J. Wang, J. D. Yan, L. Jiang, and J. Zou, "Delay-dependent stability of single-loop controlled grid-connected inverters with LCL filters," *IEEE Trans. Power Electron.*, vol. 31, no. 1, pp. 743–757, Jan. 2016, doi: 10.1109/TPEL.2015.2401612.

[87] M. Lu, Y. Yang, B. Johnson, and F. Blaabjerg, "An interaction-admittance model for multi-inverter grid-connected systems," *IEEE Trans. Power Electron.*, vol. 34, no. 8, pp. 7542–7557, Aug. 2019, doi: 10.1109/TPEL.2018.2881139.

[88] H. Gholami-Khesht, M. Monfared, M. Graungaard Taul, P. Davari, and F. Blaabjerg, "Direct adaptive current control of grid-connected voltage source converters based on the Lyapunov theorem," *2020 IEEE 9th Int. Power Electron. Motion Control Conf. IPEMC 2020 ECCE Asia*, pp. 858–863, 2020, doi: 10.1109/IPEMC-ECCEAsia48364.2020.9368224.

[89] A. Vidal *et al.*, "Assessment and optimization of the transient response of proportional-resonant current controllers for distributed power generation systems," *IEEE Trans. Ind. Electron.*, vol. 60, no. 4, pp. 1367–1383, Apr. 2013, doi: 10.1109/TIE.2012.2188257.

[90] M. Liserre, F. Blaabjerg, and S. Hansen, "Design and control of an LCL-filter-based three-phase active rectifier," *IEEE Trans. Ind. Appl.*, vol. 41, no. 5, pp. 1281–1291, 2005, doi: 10.1109/TIA.2005.853373.

[91] P. M. de Almeida *et al.*, "Systematic design of a DLQR applied to grid-forming converters," *IEEE J. Emerg. Sel. Top. Ind. Electron.*, vol. 1, no. 2,

pp. 200–210, Oct. 2020, doi: 10.1109/JESTIE.2020.3017124.

ISSN (online): 2446-1636
ISBN (online): 978-87-7573-797-0

AALBORG UNIVERSITY PRESS